

Spring 2015

A novel in vivo tumor oxygen profiling assay: Combining functional and molecular imaging with multivariate mathematical modeling

Chung-Wein Lee
Purdue University

Follow this and additional works at: https://docs.lib.purdue.edu/open_access_dissertations



Part of the [Biomedical Engineering and Bioengineering Commons](#), [Biophysics Commons](#), and the [Medicine and Health Sciences Commons](#)

Recommended Citation

Lee, Chung-Wein, "A novel in vivo tumor oxygen profiling assay: Combining functional and molecular imaging with multivariate mathematical modeling" (2015). *Open Access Dissertations*. 499.
https://docs.lib.purdue.edu/open_access_dissertations/499

This document has been made available through Purdue e-Pubs, a service of the Purdue University Libraries. Please contact epubs@purdue.edu for additional information.

PURDUE UNIVERSITY
GRADUATE SCHOOL
Thesis/Dissertation Acceptance

This is to certify that the thesis/dissertation prepared

By Chung-Wein Lee

Entitled

A NOVEL IN VIVO TUMOR OXYGEN PROFILING ASSAY: COMBINING FUNCTIONAL AND MOLECULAR
IMAGING WITH MULTIVARIATE MATHEMATICAL MODELING

For the degree of Doctor of Philosophy

Is approved by the final examining committee:

Dr. Keith M. Stantz

Chair

Dr. Yun Liang

Dr. Ulrike Dydak

Dr. Shuang Liu

To the best of my knowledge and as understood by the student in the Thesis/Dissertation Agreement, Publication Delay, and Certification Disclaimer (Graduate School Form 32), this thesis/dissertation adheres to the provisions of Purdue University's "Policy of Integrity in Research" and the use of copyright material.

Approved by Major Professor(s): Dr. Keith M. Stantz

Approved by: Dr. Keith M. Stantz

Head of the Departmental Graduate Program

4/28/2015

Date

A NOVEL *IN VIVO* TUMOR OXYGEN PROFILING ASSAY: COMBINING FUNCTIONAL AND
MOLECULAR IMAGING WITH MULTIVARIATE MATHEMATICAL MODELING

A Dissertation

Submitted to the Faculty

of

Purdue University

by

Chung-Wein Lee

In Partial Fulfillment of the

Requirements for the Degree

of

Doctor of Philosophy

May 2015

Purdue University

West Lafayette, Indiana

For my sister, three daughters and wife.

ACKNOWLEDGEMENTS

I still clearly remembered a story I read as a teenager about an old farmer who wants to give thanks to whom supplies water for his crops, stocks, and family. He started his journey by walking upstream the river, which has supplied all his water need in his whole life. He did not find the owner or any individual claiming the river; instead the river led him to the mountain. He told himself: “the one who gives water generously to everyone living by the river must stay somewhere in the mountain and I am determined to thank him in person.” He spent next several years to search the entire mountain but found no one. He was frustrated. A severe thunderstorm unexpectedly came to the mountains and the heavy rain was mercilessly pounding his body. He suddenly realized all his blessing is from heaven, and it is not far away. The farmer and I have many in common. As I am approaching the completion of my Ph.D. study, I began to look back and ask myself whom I should thank for. Any branch of sciences has progressed so far, so quick from the last century that it is impossible to do research without standing on the shoulders of giants or pioneers to look further. I want to take this opportunity to first thank the people who came before me to tunnel the very bedrock of oxygen transport modeling.

I am eager to avow my debt to Dr. Keith Stantz, whose perfectionism, patience and kindness are a model of scientific humanistic responsiveness; and to my committee members (Dr. Shuang Liu, Dr. Ulrike Dydak, and Dr. Yun Liang) for their guidance in my PhD. pursuit as a part-time student. Their scientific insights have given me the direction to the solution of the problems.

My odyssey in USA to pursue a higher degree has been long, winding, and blessed. Many days and nights when I was in solitude I often tried to remember all the events in my Ph.D. journey and figure out the meaning. I still have not found the meaning, but I found a family who will accompany with me for my whole life. That meaning is not important to me anymore. And I am forever grateful to God's grace, the support of my wife (Seokchun), and company of my three kids (Gina, Yeahna, and Sophia).

TABLE OF CONTENTS

	Page
LIST OF TABLES.....	ix
LIST OF FIGURES.....	x
LIST OF ABBREVIATIONS	xx
ABSTRACT.....	xxi
CHAPTER 1. INTRODUCTION	1
1.1 Relevance of Tumor Hypoxia.....	2
1.1.1 Hypoxia and its Clinical Significance	2
1.1.2 Hypoxia and Angiogenesis in Cancer	3
1.1.3 Angiogenic Biomarkers	4
1.2 Therapeutic Approaches Targeting Hypoxia	5
1.2.1 Hyperbaric, ARCON and EPO Therapies.....	6
1.2.2 Drugs Toxic to Hypoxic Cells	7
1.2.3 Anti-angiogenic Therapy and Vascular Normalization	7
1.3 Diagnostic Methods Used to Assess Hypoxia.....	14
1.3.1 Invasive Methods.....	15
1.3.2 Histology	16
1.3.3 Microscopy.....	19
1.3.4 PET and SPECT.....	19
1.3.5 MRI.....	20
1.3.6 Optical Imaging and Spectroscopy.....	21
1.3.7 Photoacoustic Tomography and Spectroscopy	21
1.3.8 Dynamic Contrast Enhanced (DCE) Imaging.....	24

1.4	Oxygen Transport Models	28
1.5	A 3-D <i>in vivo</i> Assay of Hypoxia.....	35
CHAPTER 2.	SPECIFIC AIMS	37
CHAPTER 3.	TUMOR MICROVESSEL STRUCTURE AND FUNCTION AND ASSOCIATED MATHEMATICAL MODELS OF OXYGEN TRANSPORT	41
3.1	Vascular Structure of the Reference Tissues and its Function.....	42
3.1.1	Window Chamber Animal Model for 3D Optical Tumor Vessel Imaging ...	42
3.1.2	Methods Used to Quantify Microvascular Structure and Function	43
3.1.3	Intravascular pO_2 Determination (PQM and Microelectrode Method)	45
3.1.4	Interstitial Tissue pO_2 Determination (PQM and Microelectrode Method) 48	
3.1.5	Intravascular $ SaO_2$ and Hemoglobin Concentration	49
3.2	Mathematical Models of Oxygen Transport	50
3.2.1	Green's Function Method to Calculate Tissue pO_2 by 3D Vasculature	51
3.2.2	MPO2 Method to Calculate Tissue pO_2	58
CHAPTER 4.	MPO2 PERFORMANCE AT VARIOUS VOXEL SIZES.....	62
4.1	MPO2 Validation Method Using Green's Function as Standard	62
4.1.1	Implementation of a Virtual Voxel Grid.....	62
4.1.2	The Average pO_2 of a Voxel Using GPO2 Model.....	64
4.1.3	The Fractional Vessel Volume in a Voxel	65
4.1.4	The Blood Perfusion in a Voxel	66
4.1.5	The $ SaO_2$ and Initial pO_2 in a Voxel.....	67
4.1.6	Linear Regression to Evaluate the Correlation Between the GPO2 and MPO2 Models of pO_2	69
4.1.7	Sensitivity of MPO2 to Changes in the Vascular Inputs.....	69
4.1.8	MPO2 Uncertainty Analysis	70
4.2	Results of Vasculature Characterization.....	70
4.2.1	Brain and Tumor Microvasculature Characterization	70
4.2.2	The 3-D pO_2 Map as Determined by Green's Function Algorithm.....	73

4.3	Comparing the Results of MPO2 Model to GPO2 Standard.....	74
4.3.1	Characterization of MPO2 Distribution in a Single Voxel	77
4.3.2	MPO2 Sensitivity to Vascular Inputs.....	78
4.3.3	Linear Regression Results of MPO2 versus GPO2.....	80
4.3.4	The Nearest Neighbor Algorithm to Correct for 50- μ m Voxel Outliers	83
4.3.5	MPO2 Uncertainty Analysis	85
CHAPTER 5. COMPARING IN VIVO PO2 MEASUREMENTS BASED ON THE MPO2		
	MODEL AND OXYLITE OXYGEN SENSOR	86
5.1	Introduction	87
5.2	Material and Method	88
5.2.1	Calibration Phantom	88
5.2.2	Animal Models	89
5.2.3	Imaging Protocols	90
5.2.4	Oxylite Probe Measurements	92
5.3	Results.....	94
5.3.1	Comparing the Dissociation Curves for Blood in a Calibration Phantom and Breast Tumors.....	94
5.3.2	Comparing pO2 Measurements Using MPO2 Model and Oxylite Probe in MCF7 Breast Tumors	95
5.3.3	Comparing pO2 Measurements Using MPO2 Model and Oxylite Probe in MCF7 Tumors Receiving AAT	97
CHAPTER 6. MOUSE PANCREATIC TUMOR HYPOXIA QUANTIFICATION		
6.1	MPO2 as a Means to Monitor the Efficacy of AAT	99
6.2	Material and Method	100
6.2.1	Experiment Design	100
6.2.2	Impact of Perfusion on Pancreatic Tumor Hypoxia	102
6.2.3	Impact of the Fractional Plasma Volume on Pancreatic Tumor Hypoxia .	103
6.2.4	Impact of Vessel Tortuosity on Pancreatic Tumor Hypoxia.....	103

6.2.5	Simulation of DCE-CT and PCT-S Uncertainty	104
6.2.6	Mapping Pancreatic Tumor Hypoxia Heterogeneity	105
6.3	Results.....	106
6.3.1	Experimental Observations of Pancreatic Tumor with DC101	106
6.3.2	Simulation Results of Blood Perfusion to Hypoxia	109
6.3.3	Simulation Results of Fraction of Plasma to Hypoxia	111
6.3.4	Simulation Results of Vessel Tortuosity to Hypoxia	112
6.3.5	Simulation Results of Synergistic Normalization to Hypoxia.....	112
6.3.6	Simulation Results of DCE-CT and PCT-S Uncertainty	113
6.3.7	Tortuosity Normalization vs. Dilation Normalization	115
6.3.8	Oxygen Concentration Maps of the Pancreatic Xenograft Tumors.....	116
CHAPTER 7.	DISCUSSION	123
7.1	Mathematics in Biology and Medicine	123
7.1.1	Using GPO ₂ as a Standard to Validate MPO ₂	124
7.1.2	Discrepancy Between the PO ₂ Calculated from MPO ₂ and GPO ₂ Models 125	
7.2	<i>In vivo</i> Validation of MPO ₂ Using the OxyLite Oxygen Sensor.....	128
7.3	MPO ₂ Analysis on PRT and NRT Tumors Post DC101 Administration	129
7.4	Perspectives in Vessel Normalization	131
7.5	Future Perspectives	133
	LIST OF REFERENCES	136
	VITA	151

LIST OF TABLES

Table	Page
Table 1.1.3.1 Genes regulated by HIF-1.....	5
Table 1.2.3.1 Preclinical AAT induced tumor vessel normalization.....	13
Table 1.2.3.2 Clinical AAT evidence demonstrating tumor vessel normalization	13
Table 3.1.2.1: Methods to study detailed microcirculation structure and hemodynamics[95].	45
Table 3.2.2.1 Simulation parameters used in MPO2	61
Table 6.2.2.1: Average DCE-CT structural and functional measurements of the control (baseline), the positive responding tumor (PRT), and the negative responding tumor (NRT).	103
Table 6.2.4.1: Four scenarios to compare hypoxia improvement by geometrical normalization against topological normalization.	104
Table 6.3.7.1: Oxygen response of various normalization mechanisms	116

LIST OF FIGURES

Figure	Page
Figure 1.2.3.1 Vessel normalization hypothesis and observation in response to AAT. (A) Schematic illustration of abnormal vessel structure and normalized vessel structure after AAT. Overdose or prolonged AAT causes inadequate vasculature which hinders oxygen delivery. (B) On the left is a two-photons image showing normal skeletal muscle blood vessels; subsequent images show colon carcinoma vasculature transplanted in window chamber model at day 0, 3, and 5 after DC101 injection[66]. (C) Diagram showing the concomitant changes in pericyte (red) and basement membrane (blue) coverage during normalization. (D) Connection between molecular mechanism (pro and antiangiogenic factor change) and vessel phenotypic/functional response [71]. (Reprinted permitted.)	12
Figure 1.3.7.1 Three steps of photoacoustic signal generation.	24
Figure 1.3.7.2 Absorption spectrum of oxygenated (red line) and deoxygenated hemoglobin (blue dash line). Isosbetic point occurs when molar extinction coefficient of oxy- and deoxy-hemoglobin is identical.	24
Figure 1.3.8.1 Basic Components and Work Flow of DCE-CT Imaging[126]. (Reprint permitted)	26

Figure 1.3.8.2 Schematic diagram of a two compartmental model to estimate tumor vascular physiology[126]. (Reprint permitted).....	27
Figure 1.3.8.1 Schematic diagram of oxygen transport via diffusion/convection in terminal microvasculature(arterioles, capillaries, and venules)[139]. (Reprint permitted)	33
Figure 3.1.1.1: The window-chamber model consists of a titanium metal frame, which holds the dorsal skin fold in place. The front skin flap is excised, and tumor cells are injected into the back plane of the opposing side skin and covered by a round coverglass. The inset shows the mouse with window implanted, with a larger view of the window itself[150]. (Reprint permitted)	43
Figure 3.1.3.1.A-B: (A) Schematic illustration of Phosphorescence Quenching Microscopy[167]. (B) A typical example of a digitized phosphorescence decay curve measured in the interstitial space of rat cremaster muscle, the decay constant is extrapolated from the decay curve[167]. (Reprint permitted).....	47
Figure 3.1.4.1.A-B: (A) Schematic representation of the pO ₂ measurement in tumor-bearing rat <i>in vivo</i> using near-infrared light[172]. (B) Oxygen measurements in anesthetized Fisher rat with a subcutaneous 9L glioma tumor. A 6x5 grid is marked on the tumor skin to locate the excitation and emission light guides. (Reprint permitted for both figures).....	49
Figure 3.1.5.1: Schematic illustration of vessel complexity to voxel size. Tumor microvasculature is overall structurally tortuous and chaotic. To represent both structural and functional aspects of a vessel network inside a large voxel by an effective	

microvessel is problematic as shown on top-left corner. The complication of vessel tree confined in a volume is reduced as voxel size is decreased(the top-middle cartoon). As the volume of voxel becomes appropriate, the vessel configuration inside the voxel is comparable to an off-center single vessel configuration illustrated on top-right cartoon. Hence adapting a Krogh-based oxygenation model to estimate average pO ₂ in a voxel is obtainable. MPO ₂ places the effective single vessel at the center of voxel and considers oxygen source(blood flow, SaO ₂ , C _{tHb} , vessel diameter) as well as consumption (cell oxygen consumption rate, fraction of cell volume)attributes to determine the tissue oxygen level.	51
Figure 3.2.1.1: Coordinate systems: Cartesian system (x ₁ , x ₂ , x ₃) for tissue space: local cylindrical polar system (r,theta,z) for one vessel segment).....	54
Figure 4.1.1.1: Schematic illustration of tumor microvasculature and lattice and voxel grid layout. Blue diamond represented the lattice points used to calculate . Red grid represented the voxel grid with voxel size (200 and 100 μm). Entire vessel segments outside of the voxel grid were colored in blue; entire vessel segments dwelling in a voxel in green; the partial vessel segments which crossed at least two neighboring voxels in yellow. Since 200 μm voxel covered entire vasculature, no blue vessel should exist under layout.	64
Figure 4.1.2.1.A-B: Demonstration of standard voxel GPO ₂ calculation. Figure B showed the tissue pO ₂ profile resulting from the tumor vasculature. The GPO ₂ of each voxel was the average of pO ₂ within the voxel.	65

- Figure 4.1.3.1: A Schematic illustration of stereology concept. An artificial regular grid (Cavalieri estimator) is superimposed onto a tissue section to estimate the area of interest (dark ring structure). A physical equivalent area representing a cross point is equal to the total area divided by the total number of crosses. Count the number of cross points hit the area of interest, marked by red circles in the figure. The area of interest is equal to the number of hits multiplying the physical unit area. This concept is also valid to estimate the volume of an irregular object..... 66
- Figure 4.2.1.1.(A/B): Reconstructed microvessel network of tumor and brain by confocal scanning microscope at sub- μm resolution. The unit is μm in both microvasculatures. 72
- Figure 4.2.1.2: Tumor and brain microvasculature diameter and flow histogram. Tumor histograms are colored in blue; brain histograms in red. For tumor blood flow, the number of vessel segments with flow rate $< 5 \text{ nL/min}$ is close to 400; the inset displays the detail distribution of blood flow from 1 to 10 nL/min 72
- Figure 4.2.1.3: Blood flow correlation of tumor microvasculature on left and of brain vasculature on right. 73
- Figure 4.2.2.1: (A) Partial oxygen pressure distribution (pO_2) in tumor. The entire tumor region is $990 \mu\text{m} \times 810 \mu\text{m} \times 150 \mu\text{m}$ in 2D view. (B) pO_2 in brain. The brain region is $150 \mu\text{m} \times 160 \mu\text{m} \times 140 \mu\text{m}$. The colorbars on the right indicate the pO_2 value. The scale bar in tumor represents 0.2mm; the scale bar in brain represents 0.1mm. 73
- Figure 4.2.2.1: Heat map of SaO_2 , blood flow, fraction of vessel volume, GPO_2 , and MPO_2 under voxel grid = 200 and 100 μm . Blue diamonds represent the location of

lattice points in ROI. Red grid represents the voxel grid with voxel size (200 and 100 μm). Entire vessel segments outside of the voxel grid are colored in blue; entire vessel segments dwelling in a voxel in green; the partial vessel segments which cross at least two neighboring voxels in yellow. The heat map colorbar indicates the value of three key inputs. The unit of fraction of vessel volume is in percentage; the value of SaO₂ goes from 0 (no oxygen binding) to 1 (saturated oxygen binding); the unit of blood flow is in nL/min. 76

Figure 4.3.1.1: Two-dimensional pO₂ profile demonstration by single vessel MPO₂ model in a 200 μm voxel. A single 20- μm diameter vessel is placed at the center of a (200 μm)³ voxel. The origin of a cylindrical coordinate is located at the entrance of blood vessel with z-axis oriented toward to blood flow direction. The cylindrical vessel configuration leads to pO₂ distribution symmetry in radial and azimuthal direction. Anoxic region, pO₂ = 0 mmHg, could occur at the remote corners in MPO₂ modeling. Any negative pO₂ from MPO₂ calculation is replaced by zero mmHg. Average tissue pO₂ by MPO₂ algorithm excludes the pO₂ contribution from the vessel lumen. The unit of gray color bar is mmHg. 78

Figure 4.3.2.1: Partial oxygen pressure sensitivity of five MPO₂ input parameters. The pO₂ response are organized into five groups (-20%, -10%, reference, 10%, and 20%). All responses are in percentage and normalized with respect to the referenced determinant; accordingly the response of the reference group is zero. 80

Figure 4.3.3.1: Brain pO₂ scattering plot of MPO₂ and GPO₂. Brain pO₂ correlation plots at voxel sizes 50 and 100 μm are shown in the panel A and B. The abscissa consists of the average Green's function pO₂ of the voxels; the ordinate consists of the MPO₂ from the same voxels. Red lines are the linear regression fitting; the result of linear regression fitting and Rsq are displayed on top-left corner..... 81

Figure 4.3.3.2(A/F): Tumor pO₂ correlation of MPO₂ and GPO₂ as function of the voxel size. Six pO₂ scattering plots of pO₂ (mmHg) at voxel sizes (50, 100, 150, 200, 250, and 300 μm) are displayed in the panel (A-F). At 50 μm voxel size (panel A), the underestimated MPO₂ outliers are enclosed in a long dash oval; the overestimated MPO₂ grouped in short dash oval. 82

Figure 4.3.4.1.A-B: Outlier voxel location in tumor microvasculature. The overestimated outliers, of which MPO₂ is exceedingly greater than Green's function pO₂, are marked with yellow solid circles in panel A; the underestimated outliers, of which MPO₂ is exceedingly lower than Green's function pO₂, are labeled with blue solid circles in panel B. 84

Figure 4.3.4.2.A-B: The correlation scattering plot after nearest neighbor correction on 50- μm grid on tumor vasculature was shown in figure (A); two outlier population in figure 5.4.3.2-A was disappeared. The goodness of fit (r-square) as function of voxel size is demonstrated in figure (B). The blue stars represented the rsq values from figure .4.3.3.2; the red star highlighted the rsq improvement by nearest neighbor algorithm..... 84

Figure 4.3.5.1: Response of MPO ₂ to the perfusion measurement uncertainty (on left) and the f-plasma measurement uncertainty (on right). Horizontal axis represents the Green's function pO ₂ of the voxel and vertical axis the average pO ₂ from 10 simulated MPO ₂ with blood perfusion and fraction of vessel volume uncertainty following Gaussian error function. The blue dot-dash line is the pO ₂ regression line of 150 μ m voxel (see figure 4.3.3.2-C).	85
Figure 5.2.1.1: Experimental setup for blood phantom SaO ₂ and pO ₂ quantification with various mixtures of air and Nitrogen.	89
Figure 5.2.3.1: An example of CtHb and SaO ₂ parametric map using photoacoustic spectroscopy (PCT-S). Figure A showed the intensity of PCT-S, three locations (A, B,C) were marked on the tumor; figure B showed the CtHb concentration in tumor; figure C showed the corresponding SaO ₂ distribution in tumor. The CtHb and SaO ₂ at location A, B, C are (41.1 μ M, 0.913), (11.6 μ M, 0.412), (31.9 μ M, 0.78).	91
Figure 5.2.3.2: 3D in vivo parametric tumor perfusion map using DCE-CT	92
Figure 5.2.4.1: A 1.0 mm ³ yellow cubic ROI was placed at position along a straight line through the center of the tumor, which approximates the actual position of the OxyLite probe (red).	93
Figure 5.3.1.1.A-C: The oxygen saturation (SaO ₂) and oxygen partial pressure (pO ₂) plot of blood phantom (A), of MDA-231 tumor (B), and of MCF-7 tumor (C).	94
Figure 5.3.2.1.A-C: Co-localized vascular physiology (perfusion, F-plasma, and F-intracellular) quantification along the axial of track in MCF tumor. Red arrow in	

perfusion indicated the voxel with significant trend deviation of perfusion and pO ₂ by OxyLite probe. The distance on horizontal axis represented the voxel position along the track.	96
Figure 5.3.2.2.A-B: Co-localized hemoglobin and Oxygen saturation quantification. The voxel were coregistered with those in figure 5.3.2.1. The red dash box indicated two voxels with significant trend deviation of the hemoglobin concentration and OxyLite probe pO ₂	96
Figure 5.3.2.3.A-C: Correlation and regression of MPO ₂ and OxyLite pO ₂ of MCF tumor.	97
Figure 5.3.3.1.A-C: Co-localized vascular physiology (perfusion, F-plasma, F-intracellular) measurements of MCF/VEGF tumor.	98
Figure 5.3.3.2.A-B: Co-localized hemoglobin and oxygen saturation of MCF/VEGF tumor.	98
Figure 5.3.3.3.A-B: Correlation and regression of MPO ₂ and OxyLite pO ₂ of MCF/VEGF tumor. The regression analysis contained both MCF and MCF/VEGF data.	98
Figure 6.3.1.1: Relative tumor growth comparison of control, mono low-dose DC101, mono high-dose DC101, mono radiation therapy, DC101-plus-RT (HD and LD). (*P < 0.05, **P < 0.01 control group to mono RT or DC101; # P < 0.05, ## P < 0.01 DC101 to DC101-plus-RT groups; error bar: standard deviation). Reprinted with permission from N. Cao[74].	107
Figure 6.3.1.2: Key physiology adjustment in positive and negative responding group. (A) Average percentage change with respect to baseline in perfusion and fraction of plasma	

of the positive (n=4) and negative (n=5) responding tumors one week post DC101 treatment. Error bars represent the standard deviation (B-C) Relative tumor growth chart of the positive, the negative, mono-RT at 5Gy/7Gy over time. The valleys in PRT and 7-Gy RT indicated the onset of vessel normalization. Error bar indicates the standard deviation. (*P<0.05; **P<0.01). Reprint permission by Cao et. al.[74].	108
Figure 6.3.1.3: Blood perfusion(F) and fraction of plasma(Fp) histogram of PRT and NRT. Reprint permission by Cao et. al.	108
Figure 6.3.2.1: Average pO ₂ and HF5 of the positive and the negative responding group at hemoglobin concentration 1.0 g/dL. Two plots on the top illustrate the HF5 and the average pO ₂ of three groups at MPO ₂ tortuosity from 1 to 1.2. Blue diamonds connected with dash lines highlight the baseline reference in HF5 and the average pO ₂ plot. Table on the bottom lists the MPO ₂ determinants to compute the pO ₂ distribution in a voxel size = 300 μm and the corresponding numerical pO ₂ result in median pO ₂ , average pO ₂ , and HF5 at various tortuosity.	110
Figure 6.3.2.2: Average pO ₂ and HF5 of the positive and the negative responding group at hemoglobin concentration 3.0 g/dL. Please read the caption in Figure 5.6.2.2 for description.	111
Figure 6.3.6.1: Sensitivity test of fraction of plasma in MPO ₂ . The upper and lower value of an error bar is determined by MPO ₂ with upper and lower f-plasma (1.1 and 0.9 times of the average f-plasma).	113

Figure 6.3.6.2: Sensitivity test of SaO₂ in MPO₂. The upper and lower value of an error bar is determined by MPO₂ with upper and lower SaO₂ (1.1 and 0.9 times of SaO₂ = 0.5).

..... 114

Figure 6.3.6.3: Uncertainty test of Hct in MPO₂. The upper and lower value of an error bar is determined by MPO₂ with upper and lower Hct(0.225 and 0.275). 115

Figure 6.3.8.1.A-D: Histogram and distribution of key MPO₂ inputs and outputs. Each figure displays a single mouse DCE-CT functional quantification and the corresponding simulated tumor pO₂ status at baseline(pre-DC101) and one week post DC101 treatment. Each figure is composed of three sections: perfusion/fraction of plasma volume(f-plasma) histogram on the top; perfusion(F)/f-plasma montage at the middle; simulated pO₂/HF5 montage on the bottom. The middle montage demonstrates the perfusion and f-plasma map of two tumors in a mouse determined by DCE-CT in single voxel resolution; the top histogram displays the perfusion and f-plasma value distribution from all voxels in the tumor shown in the middle montage. Two histograms on the left of histogram panel represent the blood perfusion in voxel at baseline and week one; two histograms on the right show the distribution of the fraction of plasma in voxel. The red arrow in the histogram indicates the location of the average value from all voxels. The bottom montage displays the simulated pO₂ and HF5 in each voxel by MPO₂ adapting the corresponding voxel perfusion and f-plasma inputs. In the title of each figure, LT represents left tumor; RT: right tumor; WK1: week one. 121

LIST OF ABBREVIATIONS

CT	Computed Tomography
DCE-CT	Dynamic Contrast-Enhanced CT
PCT-S	Photoacoustic Computed Tomography Spectroscopy
MRI	Magnetic Resonance Imaging
BOLD MRI	Blood Oxygen Level Dependent MRI
pO ₂	Oxygen Partial Pressure
VEGF	Vascular Endothelial Growth Factor
VEGF-R	VEGF Receptor
CtHb	Hemoglobin Concentration
SaO ₂	Oxygen Saturation
VOXEL(voxel)	Volume Element(a 3D extension of pixel)
RBC	Red Blood Cell
PRT	Positive responding tumor to DC101 treatment
NRT	Negative responding tumor to DC101 treatment
AAT	Anti-angiogenic treatment
Hct(hct)	Hematocrit
MPO ₂	pO ₂ calculated by Multivariate <i>in vivo</i> Hemodynamic
Model Of Tumor Oxygen Concentration model	
GPO ₂	pO ₂ calculated by Green's function method

ABSTRACT

Lee, Chung-Wein. Ph.D., Purdue University, May 2015. A Novel *In vivo* Tumor Oxygen Profiling Assay: Combining Functional and Molecular Imaging with Multivariate Mathematical Modeling. Major Professor: Keith M. Stantz.

Purpose: The objective of this study is to develop and test a novel high spatio-temporal *in vivo* assay to quantify tumor oxygenation and hypoxia. The assay implements a biophysical model of oxygen transport to fuse parameters acquired from *in vivo* functional and molecular imaging modalities.

Introduction: Tumor hypoxia plays an important role in carcinogenesis. It triggers pathological angiogenesis to supply more oxygen to the tumor cells and promotes cancer cell metastasis. Preclinical and clinical evidence show that anti-angiogenic treatment is capable of normalizing the tumor vasculature both structurally and functionally. The resulting normalized vasculature provides a more efficient and uniform microcirculation that enhances oxygen and drug delivery to the tumor cells and improves second-line treatments such as traditional radiation or chemotherapy. Early studies using the overall or average tumor hypoxia as a prognostic biomarker of anti-angiogenic therapy efficacy was ambivalent; however, recent studies have discovered that the etiology of hypoxia and its heterogeneity could be used as reliable prognostic biomarkers. The capability to longitudinally map tumor hypoxia with high spatial and temporal resolution has the potential to enhance fundamental cancer research and ultimately cancer patient care.

Method: A novel methodology to identify and characterize tumor hypoxia by fusing the physiological hemodynamic parametric maps obtained from functional and molecular imaging modalities and technique using a modified Krogh model of oxygen transport (MPO2) was developed. First, simulations studies were performed to validate this technique. Microscopy data of tumor and brain tissue (control) provided both the vasculature and rheology data. A Green's function algorithm was used to solve the ordinary differential equation and calculate the oxygen profile at a microscopic scale (15 μm) (GPO2), which was used as a reference. From this data, simulated physiological maps (perfusion, fractional plasma volume, fractional interstitial volume) and hemoglobin status (oxygen saturation, hemoglobin concentration) was used as input to MPO2 and used to calculate pO2 levels as a function of scanner spatial resolution and noise. Second, MPO2 was compared to pO2 measurements in xenograft breast tumors using OxyLite oxygen sensor as a Gold Standard, where DCE-CT and PCT-S images were acquired to obtain hemodynamic images. Finally, the vascular physiology measurements obtained from an anti-angiogenic therapeutic study in pancreatic tumors was applied to MPO2 and compared to therapeutic response.

Results: The simulation results using Green's function pO2 as standard showed that the MPO2 model performance was dependent on the spatial resolution (voxel size) of the images. Sensitivity and error analysis of this model were also investigated in this study. These oxygen transport simulations results suggest the oxygen saturation and hemoglobin concentration were two key factors in tissue oxygenation, and concomitant

with blood perfusion and tumor metabolic rate. Comparisons of the pO₂ profile obtained from MPO₂ and OxyLite probe in MCF7 tumor model demonstrated a significant correlation and approached a slope of one (after accounting for a few outliers). Simulation studies implementing the physiological data obtained from the anti-angiogenic therapeutic study in pancreatic tumors using the MPO₂ model agreed with the experimental findings that blood perfusion is a valuable prognostic biomarker in therapeutic efficacy. This model also predicted the oxygenation improvement difference from two vascular renormalization modes (topological normalization and geometrical normalization).

Conclusion: The results from the simulation and in vivo studies demonstrated the feasibility of this novel hypoxia assay. Simulation results of the pancreatic tumors provide an example of the impact the MPO₂ model in conjunction with imaging can provide when evaluating the therapeutic significance of various normalization modes in anti-angiogenic therapy, and suggests potential approaches to further improve anti-angiogenic therapy efficacy.

CHAPTER 1. INTRODUCTION

In 2014, over 1.5 million (1,665,540) Americans are expected to be diagnosed with cancer, 585,720 of which are anticipated to die from cancer. This is 1 out of every 4 deaths. Even though an overall increase in the combined 5-year cancer survival rate from 49% to 68% has occurred over the past 30 years due to early diagnosis and improved treatment, cancer rates remain very high, such as for breast and prostate cancer, or continue to increase, such as pancreatic cancer where prevalence (1.3% per year) and death rates (0.4%) continue to increase. A critical factor associated with poor treatment response and contributing to reduced patient outcome is tumor hypoxia. As demonstrated by the overall increase in cancer 5-year survival rates, the development of new imaging technologies and methods have shown to significantly impact early detection and treatment. The objective of this thesis is to advance *in vivo* imaging and our understanding of intra-tumor hypoxia and its role in cancer therapy, in particular its role in anti-angiogenic therapy. In this chapter, hypoxia, its association with angiogenesis, and its clinical relevance in patient treatment and outcome are discussed. Existing mathematical models of oxygen transport and diagnostic methods to measure intra-tumor hypoxia are discussed.

Finally, ***a novel 3-D in vivo assay to measure intra-tumor oxygen concentrations, hypoxia, and forms are hypoxia is proposed by combining imaging and oxygen transport models.***

1.1 Relevance of Tumor Hypoxia

1.1.1 Hypoxia and its Clinical Significance

The definition of hypoxia can vary depending on the biological system under investigation. For example, a biochemist may define hypoxia as the level of dissolved oxygen necessary to sustain life on microbial fauna, a physiologist as the level of oxygen which influences organ function, a radiobiologist on cell survival curves, and oncologists on clinical outcomes, such as the hypoxic fraction or median partial pressure of oxygen (pO₂). In many cancers, the oxygen or hypoxic microenvironment within a tumor plays a critical role in a patient's response and resistance to therapy. Studies have shown that low levels of oxygen, or hypoxia, deprives cancer cells of hypoxia and confers resistance to chemotherapeutic drugs and ionizing radiation, leading to treatment failure and poor disease-free/overall survival rates [1-3][25-28]. This has been observed in patients with breast, head-and-neck, and cervical cancers, and are more likely to suffer metastasis and local recurrence if their tumors are determined to be hypoxic [4, 5][29-30]. An *in vivo* assay of tumor oxygenation that bridges the gap between the pathologist, the physiologist and the oncologist would greatly enhance the translational capacity of this research these disciplines within the clinic.

1.1.2 Hypoxia and Angiogenesis in Cancer

Tumors growing beyond 1 mm in diameter exceed the maximum oxygen diffusion length and forms hypoxia [6]. While normal cells typically die under severe oxygen stress or hypoxia (< 10 mmHg) (e.g., apoptotic pathways) [7], cancer cells have been shown to survive and transform into a more aggressive phenotype, metastasizing to other parts of body [8-10]. One critical factor contributing to this phenotype is the cancer cell's ability to initiate the formation of new blood vessels or angiogenesis. Unlike normal angiogenesis observed in wound healing or ovulation, tumor-induced angiogenesis forms a structurally and functionally abnormal vasculature that fluctuates spatially and temporally throughout the tumor volume [11, 12]. This resulting vasculature network in turn contributes to or detracts from the supply (or delivery) of oxygen to the tumor cells, and when combined with their high consumption and proliferation rates, results in a local imbalance between the supply and demand of oxygen. Several factors contributing to this imbalance include: (1) low oxygen partial pressure in arterial blood (hypoxemic hypoxia); (2) reduced capacity of the blood to carry oxygen (anemia or carbon monoxide poisoning, e.g., anemic hypoxia); (3) reduced blood perfusion (ischemia) or periodical fluctuations in blood perfusion (cycling or acute hypoxia); (4) increased oxygen diffusion distance due to deterioration of local vasculature or elevated levels of interstitial fluid pressure (diffusion or chronic hypoxia); and (5) inability of cells to utilize oxygen due to cellular toxicity (cyanide poisoning) (histotoxic or cytotoxic hypoxia). Despite the advances over the past four decades in our understanding of angiogenesis, the detailed interactions between angiogenesis, vascular physiology and hemodynamics, and

hypoxia remain unknown and an active area of research [13, 14]. This is not a surprise since the simultaneous quantification of oxygen levels and other corresponding physiological parameter measurements are difficult and in many cases impossible to obtain.

1.1.3 Angiogenic Biomarkers

As discussed in the previously, tumors are marked by uncontrolled cellular proliferation; and, as the tumor volume increases, so does the demand for oxygen and nutrients. Once hypoxia forms, a complex network of biomolecular pathways are initiated, where various transcriptional factors, genes, and growth factors are up-regulated, in particular vascular endothelial growth factors (VEGF) and their receptors (VEGFR). Angiogenesis initiates endothelial cells (ECs) within existing microvasculature to respond by randomly sprouting neovessels and pruning of existing vasculature (vascular remodeling) [15, 16]. This resulting tumor-induced vasculature appears structurally chaotic and highly dysfunctional, and fails to provide the extra nutrients and oxygen required by the tumor cells. The hypoxic status within the tumor becomes exacerbated, and further drives the tumor cells to secrete additional growth factors. Unlike normal physiological hypoxia observed in wound healing or new tissue generation, tumor hypoxia leads to a highly abnormal vasculature and vascular physiology which are causal to genetic instability, metastasis, immunosuppression, inflammation, cancer stem-cell (CSC) phenotype, epithelial-mesenchymal transition (EMT), resistance to cell death, and altered metabolism.

A key transcription factor expressed under hypoxic conditions is the Hypoxia-Inducible Factor 1 or HIF-1 [17, 18]. Several key genes related to tumor angiogenesis and oxygenation regulated by HIF-1 is listed in table 1.1.3.1 Vascular Endothelial Growth Factor (VEGF) family and their receptors (VEGFR) are the most potent and well investigated of these pro-angiogenic molecules [19, 20]. In addition to HIF-1, several other genes, proteins, enzymes, and chaperones related to tumor progression and therapeutic resistance have also been shown to be activated by hypoxia, such as glycolytic enzymes, glucose transporters (GLUT1 and GLUT3), and carbonic anhydrase IX (CA9) [18, 21-26]. Their role in angiogenesis or in cancer progression is under investigation.

Table 1.1.3.1 Genes regulated by HIF-1

Gene	Function	References
VEGF 1/2; VEGFR-1/2	Hypoxia-induced angiogenesis; cell survival and growth	[27-29]
Notch signaling	Cell differentiation, proliferation, and apoptosis	[30, 31]
Erythropoietin	Red blood cell production in kidney	[32]
Tie 1/2	Vessel formation, maturation, maintenance	[33, 34]
TGF- β	Differentiation, angiogenesis, tissue regeneration	[35, 36]

VEGF: Vascular Endothelial Growth Factor; TGF: Transforming Growth Factor

1.2 Therapeutic Approaches Targeting Hypoxia

Over the past several decades, clinical studies have been performed to overcome hypoxia by increasing tumor oxygen levels (hyperbaric, ARCON, and EPO therapies),

developing chemotherapy agents cytotoxic to cells exposed to hypoxia, or normalizing the tumor vasculature.

1.2.1 Hyperbaric, ARCON and EPO Therapies

Hyperbaric, ARCON, and EPO therapies attempt to increase the patient's overall systemic levels of dissolved (plasma) oxygen, perfusion, or hemoglobin, respectively, thereby the overall tumor oxygen levels. Hyperbaric oxygen treatment exposes patients to an elevated oxygen pressure environment prior to/during RT/CRT, thereby increasing the amount of dissolved oxygen in the blood plasma delivered to the tumor. This strategy preferentially affects regions of chronic hypoxia, not necessarily acutely hypoxic regions, and potentially explains the modest increase (10%) in locoregional control in HNC patients[32;37]. ARCON treatment targets both acute and chronic hypoxia by increasing perfusion (nicotinamide) and oxygen partial pressure (carbogen breathing). Clinical results are promising, a significant increase (>80%) in local control, but this treatment incurs a number of patient side effects, such as nausea, vomiting, and confluent mucositis (in 90% of patient population), which limits its clinical applicability [33]. Erthropoietin (EPO) injections reduce anemic-based hypoxia by increasing the oxygen carrying capacity (hemoglobin) of the blood. However, locoregional progression-free survival in cancer patients decreased. Severely anemic patients (< 9g/dL) may benefit from EPO, but increasing a patient's hemoglobin level beyond 14 g/dL actually decreases pO₂ levels due to venostasis obstructing perfusion.

1.2.2 Drugs Toxic to Hypoxic Cells

Tirapazamine (TPZ) is a new genre of drugs cytotoxic to hypoxic cells. TPZ is reduced in the absence of oxygen to form a free radical, which induces DNA breaks, chromosomal aberrations, and cell death. In the presence of oxygen, TPZ is oxidized to form a nontoxic agent. When applied *prior* to chemotherapy (CT) or chemoradiotherapy (CRT), an increase in the local progression-free and overall survival rate (60-80%) is observed (phase I and II studies)[35], but, when TPZ is applied *concurrently* with CRT, overall survival rates did not improve,[36] indicating a longitudinal dependency on therapeutic efficacy. Though promising, an international phase III clinical study was terminated due to an unexpected toxicity due to (1) activation of TPZ in poorly perfused organs and (2) poor diffusion of TPZ through hypoxic tumor tissue.

From the above studies, the targeting of hypoxia significantly influences therapeutic outcome by influencing tumor hemodynamics associated with diffusive (chronic) and perfusion-based (cycling, acute) hypoxia, and drug delivery. Unfortunately, the above protocols induce systemic toxicities thereby limiting their effectiveness. A more targeted approach is to modulate angiogenesis and the resulting vascular physiology and hemodynamics within the tumor.

1.2.3 Anti-angiogenic Therapy and Vascular Normalization

In 1972, Dr. Judah Folkman proposed a very different approach that targets the tumor vasculature as a treatment for cancer. His idea was to starve the tumor cells by chocking

off the blood supply to the solid tumors [37, 38]. However, in some tumors anti-angiogenic therapy (AAT) as a monotherapy did not show benefits in some clinical trials [39-42]. These puzzling results led to a number of new potential mechanisms, such as vascular normalization first hypothesized by Dr. Rakesh Jain in 2001 and 2004 [43, 44]. In this section, a brief history describing the formation of the first anti-angiogenic drug and subsequent clinical studies are presented. These results, or lack of results, from these studies led to the idea of vascular normalization, from which our 3-D hypoxia assay will be tested.

In 1971, Dr. Folkman was the first to prove the existence of pro-angiogenic factors that were released by the tumor cells, and proposed to block their action as a means to potentiate cancer therapy, e.g., arrest tumor growth [37, 38]. Donald Senger and Harold Dvorak identified this protein and developed a partially purified form of this protein in 1983, and named it vascular permeability factor (VPF) due to its ability to induce vascular leakage [45]. By 1989, researchers at Genentech isolated and cloned a protein mitogenic only to endothelial cells and named it vascular endothelial growth factor (VEGF)[46], which was later determined to be identical to VPF protein. Studies by Eli Keshet and Karl Plate (1992) demonstrated that VEGF was highly expressed within hypoxic regions of a tumor, and postulated that hypoxia was a key environmental trigger stimulating tumor angiogenesis [47, 48]. In the following years, additional forms of VEGF and its receptors were discovered, such as VEGFR-1 (FLT-1) by Carlie de Vries et al (1992) [49] VEGFR-2 (KDR) by Terman et al [50]. Unfortunately, clinical trials of anti-

angiogenic inhibitors by themselves did not significantly increase a patients' overall survival [7]. It was not until 2004 when the first angiogenesis inhibitor, bevacizumab (AvastinTM), was approved by the FDA, followed by a number of FDA approved anti-angiogenic drugs targeting the VEGF-VEGFR pathways (bevacizumab[51], ranibizumab[52], lapatinib[53], sunitinib[54], sorafenib[55]) and others pathways (e.g., PDGF, FGF, c-Kit, VEGFR1, VEGFR2, Tie-1, Tie-2[56, 57]). Approval was predicated on the results from clinical trials that demonstrated an unprecedented increase in OS for colorectal patients when bevacizumab was combined with chemotherapy drugs [8] [58]. Unfortunately, clinical studies targeting other cancers have not produced similar results. For example, in pancreatic cancer patients, an increase in OS was not observed (2009)[9]; in ovarian cancer patients, an increase in progression free survival (PFS) was not observed unless used in maintenance therapy (2010) [10-11][59]; and in metastatic breast cancer patients, an increase in OS was not observed, and in many cases favored the placebo arm (2010) in spite of an increase in PFS [12,13,14]. In fact, recent clinical and preclinical studies have suggested that angiogenic inhibitors can increase the invasiveness (glioma patients; 2009)[15] and metastatic potential (mouse models) (2009)[16,17,18].

To understand these temporary gains (PFS) without improving overall survival or invasiveness, the association between a tumor's angiogenic profile and hypoxic status is being proposed as a causal factor. Given that preclinical studies showed an increased benefit by combining antiangiogenic therapy with radiotherapy [60-63], a rationale

supposition is that angiogenic therapy (AAT) may have improved the vascular function to deliver more oxygen to the tumor cells, to delivery oxygen to more tumor cells, or both. This would also be true for chemotherapy agents. Such a finding appears counterintuitive because AAT would also reduce the vascular volume or microvessel density within the tumor. In 2001, Dr. Jain proposed the vasculature normalization hypothesis to explain this enigma [44].

Perhaps the most important lesson from the antiangiogenic clinical trials is that the antiangiogenic agents targeting endothelial cells must combine with those agents targeting cancer cells to reach appreciable impact on patient survival. Evidence of vessel normalization has been shown in many preclinical and clinical studies (table 1.2.3.1 and table 1.2.3.2). Before explaining the vessel normalization hypothesis, an overview of the molecular mechanisms associated with angiogenesis and pertinent to the phenotype changes in the microvasculature is discussed. In normal tissue repair or angiogenesis, pro- and antiangiogenic factors are exquisitely balanced and tightly choreographed. When pro-angiogenic factors are overexpressed, abnormal sprouting from an existing vessel (angiogenesis) is initiated, and the resulting newly formed vascular appears leaky, tortuous, and highly dilated with randomness to their interconnections or network. Pericytes are loosely attached to the capillaries or missing, and the basement membrane varies in thickness, lacks uniformity, and has large gaps or pores (Figure 1.2.3.1). The normalization hypothesis suggests that once the excess pro-angiogenic factors are removed and a balance restored, the vasculature returns to a normal or

efficient state of functionality, as shown in figure 1.2.3.1. By continuing to remove pro-angiogenic factors, the loss of vasculature inhibits the delivery of oxygen and nutrients, the supposition Dr. Folkman used when proposing AAT. However, this lack of oxygen can reduce the sensitivity of the tumor to radiation, inhibit drug delivery, and initiate a number of unfavorable biological responses hindering these cytotoxic therapies (e.g., cell repair mechanisms, dormancy, cancer stem cells prevalence and maintenance). To date, the details of why simply removing excess pro-angiogenic factors will spontaneously lead to vessel normalization and improve therapeutic outcomes remain unanswered.

To test the hypothesis of vascular normalization, numerous animal studies investigating the therapeutic response to anti-angiogenic agents has been performed. In various xenograft and orthotopic tumor models, a temporal response has been observed, which can start as early as one day after treatment and lasts for up to one week [11, 64-68]. Clinical studies also report a benefit [19, 69], as for glioblastoma patients where normalization window began on day one and lasted for approximately a month (e.g., a full course radiation therapy) [70]. Conceivably, the regimen of AAT, stage of tumors, characteristics of the host organ, and mechanism of angiogenesis and therapeutic targets all play a role in the duration of the normalization window and the outcome of the treatment. Clearly, an *in vivo* assay that can reliably identify biomarkers associated with vessel normalization and the methods to measure and monitor the normalization

process is critical to further improve the therapeutic gain and to discover the causes of the resistance to AAT in some tumors.

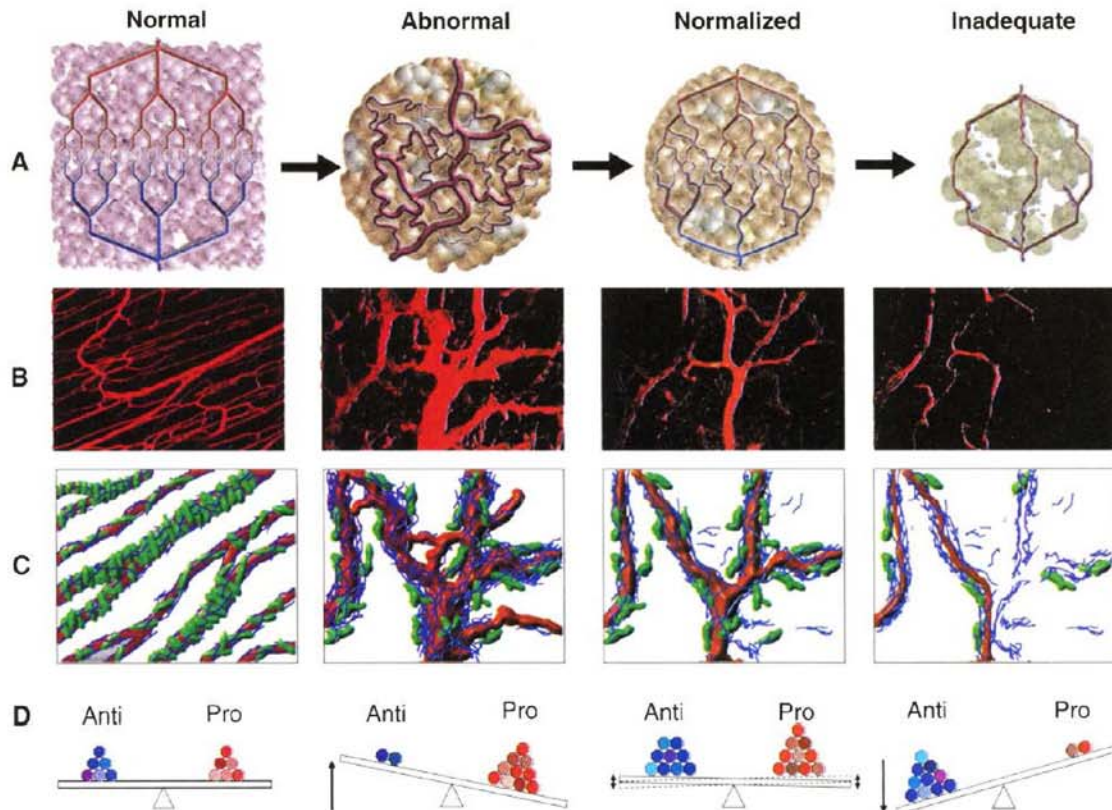


Figure 1.2.3.1 Vessel normalization hypothesis and observation in response to AAT. (A) Schematic illustration of abnormal vessel structure and normalized vessel structure after AAT. Overdose or prolonged AAT causes inadequate vasculature which hinders oxygen delivery. (B) On the left is a two-photon image showing normal skeletal muscle blood vessels; subsequent images show colon carcinoma vasculature transplanted in window chamber model at day 0, 3, and 5 after DC101 injection[66]. (C) Diagram showing the concomitant changes in pericyte (red) and basement membrane (blue) coverage during normalization. (D) Connection between molecular mechanism (pro and antiangiogenic factor change) and vessel phenotypic/functional response [71]. (Reprinted permitted.)

Table 1.2.3.1 Preclinical AAT induced tumor vessel normalization

Agent	Tumor model	Effect on vessel structure	Effect on vessel function
Trastuzumab	HER2 + breast carcinoma	↓ Diameter	↓ Permeability [72]
Gefitinib/PI-103	Fibrosarcoma	↓ Tortuosity, ↑ PVC	↑ TBF/oxygenation [73]
DC101	Pancreatic carcinoma	↓ Vessel volume	↑ TBF [74]
Palomid-529	Glioma	↓ Tortuosity	↓ Permeability [20]
Agent	Tumor model	Effect on vessel structure	Effect on vessel function
Trastuzumab	HER2 + breast carcinoma	↓ Diameter	↓ Permeability [72]
Gefitinib/PI-103	Fibrosarcoma	↓ Tortuosity, ↑ PVC	↑ TBF/oxygenation [73]
DC101	Pancreatic carcinoma	↓ Vessel volume	↑ TBF [74]
Palomid-529	Glioma	↓ Tortuosity	↓ Permeability [20]

HER2: human epidermal growth factor receptor-2; TBF: tumor blood flow; PVC: perivascular cell coverage. Reference numbers are listed in parentheses.

Table 1.2.3.2 Clinical AAT evidence demonstrating tumor vessel normalization

Tumor type	AAT agent	Effect on vessel structure	Effect on vessel function
Rectal carcinoma (n = 32)	Bevacizumab	↓ Vessel Density, ↑ PVC	↓ TBF, ↓ IFP [19]

Table 1.2.3.2 Continued

Glioblastoma (n = 31)	Cediranib	↓ Vessel size	↓ Permeability [70, 75]
High-grade glioma (n = 5)	Bevacizumab	↓ Vascular arcades and glomeruloid vessels	[76]
Prostate Carcinoma (n = 10)	Androgen ablation	Pruning immature vessel, ↑ PVC	[77]
HER2 + breast cancer brain metastases (n = 22)	Lapatinib	↓ Tortuosity	[78]

AAT: antiangiogenic therapy; PVC: perivascular cell coverage; IFP: interstitial fluid pressure; TBF: tumor blood flow; HER2: human epidermal growth factor receptor-2. Patient numbers are indicated in parentheses of tumor type.

1.3 Diagnostic Methods Used to Assess Hypoxia

Identifying reliable prognostic or surrogate markers of hypoxia is a priority in cancer research and therapy, affecting treatment response and metastatic progression.

Standard clinical procedures are highly invasive, where a polarographic needle electrode [79, 80] is inserted into the tumor or a biopsy and subsequent histological analysis is required. These techniques when applied to preclinical and clinical studies found that the spatial and temporal heterogeneity of hypoxia closely link to the poor outcome of cancer therapy, but quantifying the heterogeneity remains a challenging task. Recently, several imaging methods and modalities are currently under investigation to non-invasively assess tumor hypoxia, both directly and indirectly [81, 82]: PET/SPECT, MRI, Optics, thermoacoustics, dynamic contrast imaging.

1.3.1 Invasive Methods

The polarographic needle electrode (or Eppendorf pO₂ histograph) is the clinically accepted *gold standard* method to measure pO₂ levels *in vivo*. This instrument is based on electrochemical reduction of oxygen resulting in a current proportional to the amount of dissolved oxygen (DO) present in the tissue. At the tip of the needle consists of a gold cathode and silver-silver chloride anode. Near the Au electrode, oxygen reduces to form water, thus consuming oxygen, which is then oxidized (AgCl) at Ag electrode resulting an electrical current across the electrodes. A Teflon semi-permeable tip prevents tissue proteins from contaminating the tip as enters the tumor. To minimize the effects of oxygen consumption, the probe acquires pO₂ measurements within <1.4 second. During insertion of the needle measurements are taken in 0.7mm steps along the trajectory of the needle, where the needle moves 1.0 mm forward and 0.3 mm reversed to minimize physical disruption to the tissue (blood vessels). Variations in pO₂ are represented by a histogram. In clinical studies, a median-pO₂<10 mmHg or a high hypoxic fraction (HF<2.5, 5.0mmHg or HF2.5, HF5) is correlated to a lower overall and recurrence-free survival rate. In spite of its ability to directly measure pO₂, the Eppendorf probe cannot differentiate between chronic and acute hypoxia and is not widely used due to its invasiveness, lack of spatial information, a low signal-to-noise at low pO₂ levels, and inability to distinguish necrotic from hypoxic regions.

Another oxygen probe device to measure local pO₂ is OxyLite probe system (OxyLite, Oxford Optronix, Oxford, UK). It operates on the principle of fluorescence lifetime of

ruthenium chloride is oxygen level dependent; the lifetime of fluorescence is inversely related to the amount of oxygen at the tip[83]. The comparison of pO₂ measurement in normal and tumor tissue between OxyLite and the standard, polarographic needle electrode, was reported[84-86]. The correlation is better when pO₂ is less than 40 mmHg.

1.3.2 Histology

Current clinical methods to assess tumor hypoxia is by performing a tumor biopsy and immunohistochemical (IHC) staining for exogenous (pimonidazole, EF5) and endogenous (HIF1 α , GLUT-1, CA9) biomarkers. Two exogenous biomarkers used clinically to identify tumor hypoxia are pimonidazole and EF5. These 2-nitroimidazoles undergo bioreduction in the absence of oxygen to produce reactive intermediates. Under hypoxic conditions, the reactive products bind covalently to intracellular macromolecules, while in the presence of oxygen the reaction is oxidized back into its original form. Therefore, the amount of stable adducts retained in the cells is a measure of the lack of oxygen present in the cells. To assess tumor hypoxia, these agents are injected 24-48 hours prior to acquiring a biopsy, after which, immunohistochemistry or immunofluorescence imaging provides a relative measure of tumor oxygenation. In some clinical studies, pimonidazole and EF5 binding (median-pO₂, HF2.5 or HF5) did correlate with locoregional tumor control and disease-free survival [87] and event-free survival time[88], while in other studies the correlation is weak or insignificant. This is most likely due to the probe being more sensitive to chronic hypoxia. Histological

assessment of the staining pattern of these biomarkers is consistent with long diffusion lengths, consistent with chronic hypoxia, which is accentuated by acquiring a biopsy 1-2 days after injection primarily due to pimonidazole and EF5 pharmacokinetics. This explains, in part, why in some studies pimonidazole or EF5 binding did not correlate with Eppendorf probe measurements[89, 90]. Overall, the strengths of these exogenous probes are their ability to measure hypoxia at the cellular level, monitor spatial heterogeneity (if extirpated), provide relative oxygen concentrations, and predict clinical outcome. Its drawbacks are its invasiveness, preference to assess chronic hypoxia, and complex calibration (including *ex vivo* calibration) if absolute pO_2 measurements are desired.

The primary endogenous protein activated by low oxygen concentrations is the transcriptional factor hypoxia inducible factor 1, HIF-1. HIF-1 is a heterodimer consisting of a HIF-1 α and a HIF-1 β subunit, where the latter is targeted for proteasome degradation under normoxic conditions. *In vitro*, HIF-1 α protein levels in cultured cancer cells are tightly regulated by oxygen levels; however, *in vivo*, HIF-1 α expression in tumors is weakly correlated or lack correlation to pO_2 (Eppendorf probe). This is primarily due to additional mechanisms influencing HIF-1 α stability, such as the tumor microenvironment (acidosis, pyruvate and lactate, glucose), growth factors (IGF-2 and NO), and genetic mutations or oncogenes (VHL, p53, and PTEN). Under low oxygen levels HIF-1 α remains stable and transactivates over 70 genes that attempt to increase

the availability of oxygen to the tumor or modulate the metabolic activity of the cancer cells. The most widely studied proteins are VEGF (angiogenesis and metastasis), GLUT-1 (glucose metabolism), CA IX (pH microenvironment), and EPO (hemodynamics). Each of these downstream targeted genes of HIF-1 α range in their significance as a prognostic indicator[91-93], but when combined into a single multivariate statistic it strengthens in significance and provides a glimpse into the tumor oxygen microenvironment. For example, HIF-1 α stabilizes within minutes under hypoxic conditions decreasing quickly (<30 minutes) upon reoxygenation; GLUT-1 peaks approximately 16 hours after hypoxic insult increasing with distance from the blood vessels; and CA IX remains stable 16-92 hours under low oxygen conditions and is predominantly found in poorly perfused regions. Each of these factors is influenced under different forms of hemodynamics, and hypoxic-type.

The above techniques are (1) invasive, which significantly and permanently damage the tissue; (2) cannot distinguish between the different types of hypoxia; and (3) represented as tumor-averaged values, difficult or unable to link with in vivo function. These measurements, though useful, provide an incomplete picture of tumor hypoxia, such as those factors leading to different types of hypoxia, variations in these factors within the tumor, and the involvement of these factors in reoccurrence and metastasis of cancer.

1.3.3 Microscopy

Optical microscopy has often used to scan the detailed structure and function of microvasculature with submicron resolution. The microscopic measurement has been shown to reveal insights into the mechanisms of oxygen transport, but due to its limited resolution at depth, it cannot be used in clinical diagnosis except for surface imaging (e.g., melanoma). As an example, intravital confocal microscopy integrated with various techniques has been used to acquire microvessel functions and structures at various depth[94, 95], but with a penetration depth of confocal of 150-300 μm (see Chapter 3).

1.3.4 PET and SPECT

An *in vivo* imaging technique measuring hypoxic implements radiopharmaceuticals based on 2-nitroimidazoles ligands (e.g., pimonidazole and EF5) conjugated to PET (^{18}F or ^{124}I) or SPECT tracers (^{123}I or ^{98}Tm)[81, 82, 96]. Several different derivatives of this structure have octanol and water partition coefficients, e.g., compound solubility in octanol (non-polar solvent) to that in water(polar solvent), close to 1, which allows these tracers to be homogeneously distributed in the body one hour after injection [97]. In addition, their distribution is significantly impacted by reduced blood flow [98, 99]. Like their histological counterparts, these tracers are sensitive to tissue hypoxia at the micro-regional level. Studies using ^{18}F -MISO or ^{64}Cu -ATSM demonstrate that a tumor-averaged signal relative to muscle correlates to therapeutic response and poor outcome to radiation and chemotherapy [100]. The drawbacks of this technique include limited

spatial resolution afforded by PET, pharmaceutical effects due to radiation and dependences on washout kinetics, and poor temporal response (e.g., chronic hypoxia).

1.3.5 MRI

Several MRI techniques, such as Blood Oxygen Level Dependent (BOLD), can measure tumor hypoxia. These methods are attractive because they are noninvasive, do not require the need for a short-lived radioactive reporter molecule, and can have good spatial (~ 1.0 mm) and temporal resolution (50 ms) [101] thus allowing tumor oxygenation to be monitored in real-time tumor and changes during treatment. The BOLD signal measures the amount of deoxyhemoglobin in the blood, which the paramagnetic iron (Fe^{2+}) enhances the transverse (T_2) and apparent transverse (T_2^*) relaxation rates from water in blood and in tissue surrounding the blood vessel [102]. No reliable pO_2 conversion from T_2^* is available for BOLD MRI because of the extreme sensitivity of T_2^* to the basal state of tumor oxygenation and to many other physiological parameters, such as pH or blood flow [103]. Therefore, BOLD has been unable to provide a quantitative measure of pO_2 (SaO_2) in tumors [104] and the sensitivity decreased as spatial resolution increased [105]. Another recently developed method utilizes oxygen-sensitive reporter molecules for MR oximetry, in particular perfluorocarbons (PFCs). The PFC signal was found around the periphery of tumors after intravenous injection [106]. New echo-planar imaging methods termed FREDOM after an intra-tumor injection of PFC was able to form pO_2 maps in a tumor and revealed good

correlation with oxygen electrodes over time [107, 108]. However, a number of limitations exist, in particular the toxicity from PFCs and the reduced precision of pO₂ measurements when pO₂ drops below 10mmHg [109, 110]. As with PET, research groups are labeling ¹⁹F with 2-nitroimidazoles. It has shown to have a similar sensitivity to that of proton MRI and a small endogenous background signal; however, it requires long data acquisition.

1.3.6 Optical Imaging and Spectroscopy

Near infrared optical spectroscopic techniques based upon the characteristic absorption properties of hemoglobin molecules is widely used to measure hemoglobin concentration (CtHb) and oxygen saturation(SaO₂) in biological tissue[111]. Studies demonstrate that this technique can be used to measure the hemoglobin distribution and oxygen saturation in breast, brain, limb and joint studies [112, 113]. However, the absorption and scattering of light by tissue limits its spatial resolution and sensitivity as a function of depth making it difficult to provide local, quantifiable results.

1.3.7 Photoacoustic Tomography and Spectroscopy

Optical imaging techniques possess superior lateral resolution, but suffer poor axial resolution as a result of photon absorption and scattering in opaque medium propagation. The lateral and axial resolution also decays drastically as photons travel deeper. Biologists or physicians are always interested in detecting the tissue morphology and physiology in deep tissue. Bowen et al first recognized the potential of

applying the photoacoustic (or thermoacoustic) effect in imaging to mitigate the intrinsic scattering limitation in soft tissue from optical or NIR light [114, 115]. When pulsed energy is absorbed by the body, this absorbed energy is converted to heat, increases the local temperature, results in a subsequent volume expansion, and generates a broad-band acoustic wave (see figure 1.3.7.1). A transducer array is used to detect these ultrasound signals. Hence a basic photoacoustic imaging instrument is composed of two main components, a pulsed light source (Laser) and an array of transducers to detect acoustic signals. The photoacoustic scanners used in the studies implement a spherical transducer array to obtain as close to 2π projection of the tumors. These scanners implement a modified 3-D Radon transformation algorithm to reconstruct a volumetric image of the tumor [116]. These thermally-generated acoustic waves and resulting volumetric absorption maps provide a number of key advantages, such as increased sensitivity compared to optical energy in tissue and improved spatial resulting due to less tissue scattering.

In angiogenesis and hypoxia research, photoacoustic imaging provides *in vivo* measurement of tissue oxygen saturation levels (SaO₂) and hemoglobin concentrations (CtHb), two key vascular physiological parameters in the transport of oxygen to the parenchyma cells by the microcirculation system. Similar to optical spectroscopy, each biomolecule has an intrinsic absorption spectrum define by its molar extinction coefficient, $\varepsilon(\lambda)$. Due to the change in the absorption spectrum between deoxygenated-

hemoglobin and oxygenated-hemoglobin, spectroscopic methods can be employed to obtain both CtHb and SaO₂ levels. To acquire CtHb, photoacoustic images are acquired at the isosbestic wavelength (796 nm) of hemoglobin, where the molar extinction coefficient is independent of the hemoglobin's oxygen status (see figure 1.3.7.2). By acquiring photoacoustic images at wavelength ranging from 680 to 950 nm, spectral deconvolution algorithms are applied to estimate the SaO₂ of the blood within the tumor's blood vessels. By considering the hemoglobin absorption spectrum as the linear combination of oxy- and deoxy-hemoglobin spectra (figure 1.3.7.2), the SaO₂ can be derived by fitting the measured data to the following the equation for $\mu_a(\lambda)$,

$$\mu_a(\lambda) = C_{tHb} \cdot (SaO_2 \cdot \varepsilon_{HbO_2}(\lambda) + (1 - SaO_2) \cdot \varepsilon_{Hb}(\lambda)),$$

where $\varepsilon_{HbO_2}(\lambda)$ and $\varepsilon_{Hb}(\lambda)$ are the extinction coefficients of oxygenated and deoxygenated hemoglobin at wavelength λ .

In summary, photoacoustic tomography is a non-ionizing, fast scanning (3-12 seconds), noninvasive imaging modality employing laser-induced ultrasonic signals within the biological tissue. Similar to NIR optical spectroscopy, photoacoustic computed tomography spectroscopy (PCT-S) provides both CtHb and SaO₂ but significantly increases depth of imaging and spatial resolution based upon the center frequency of the ultrasound transducer. In addition to diffusion-limited chronic hypoxia in tumor, it has been shown that tumors also experience acute intermittent cycling hypoxia which could contribute to tumor metastasis [117, 118]. With Endra scanner, fast PCT-S scans

with more than 10 wavelengths can be acquired in 2-3 minutes. Photoacoustic imaging is a new technology with considerable promise, [98, 99] where early clinical studies in mammography have been performed or ongoing [119, 120].

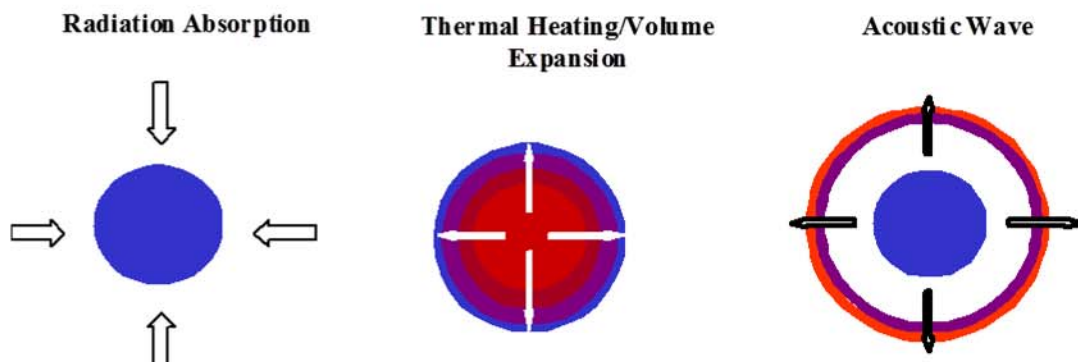


Figure 1.3.7.1 Three steps of photoacoustic signal generation.

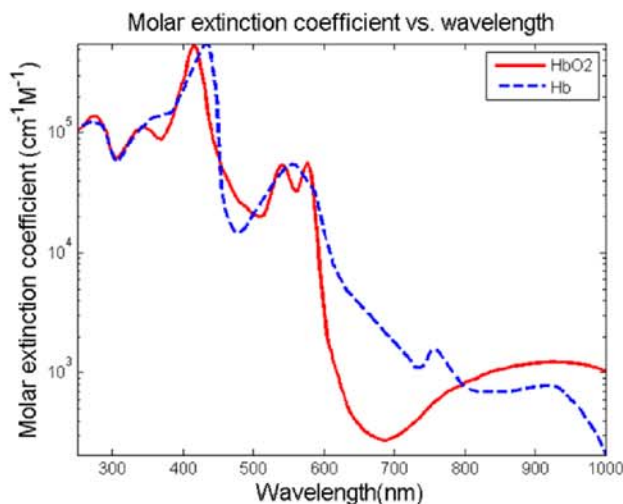


Figure 1.3.7.2 Absorption spectrum of oxygenated (red line) and deoxygenated hemoglobin (blue dash line). Isosbetic point occurs when molar extinction coefficient of oxy- and deoxy-hemoglobin is identical.

1.3.8 Dynamic Contrast Enhanced (DCE) Imaging

Dynamic contrast enhanced imaging is a method that measures the vascular physiology of tissue, for example perfusion, fractional plasma or blood volume, permeability-

surface area product, and other parameters unique to each organ. DCE technique implements a fast acquisition scanner, the administration or controlled injection of a (inert) contrast agent, and pharmacokinetic models from which the vascular physiological parameters are estimated by fitting the time-resolved image intensities (see figure 1.3.8.1). This concept was first applied to CT by Axel et al (1980) to simultaneously acquire the morphological and local functional status in brain tissue [121], as in MRI [122], ultrasound [123, 124], and PET [125]. For the research in this thesis, a standard methodology for DCE-CT has been developed, where the combined spatial-temporal resolution can be obtained, the contrast-to-noise ratio (CNR) is sufficient to measure sufficiently low fractional plasma volumes and perfusion, and the linearity between the CT signal in Hounsfield units and the contrast agent concentration is over a wide dynamic range necessary for tumors. By contrast the signal intensity of DCE-MRI is not linearly correlated to the contrast agent concentration, the signal intensity or CNR can depend upon many parameters in imaging sequence, and the influence of water exchange introduces additional parameters into the analysis, all of which complicates its implementation and introduces uncertainties.

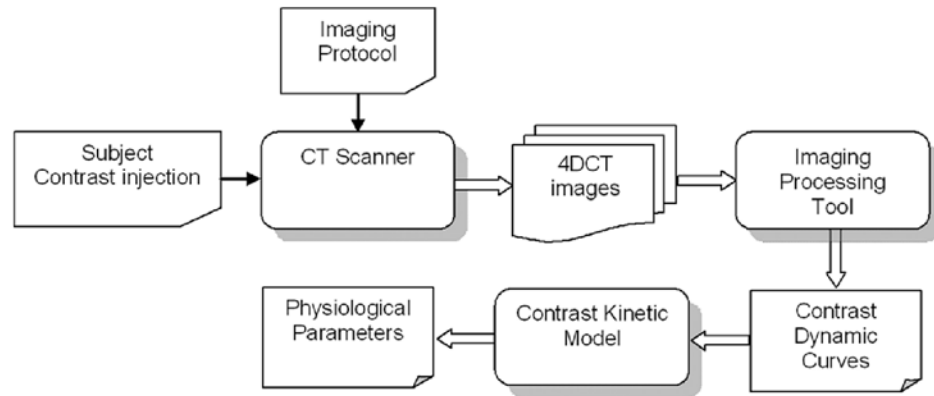


Figure 1.3.8.1 Basic Components and Work Flow of DCE-CT Imaging[126]. (Reprint permitted)

Another key to the success of DCE-CT technique is the selection of tracer kinetic model, which depends on knowledge of the tissue or organ structure and potential complexity of the vascular physiology. For the studies performed in this research, a two compartmental model was used to fit the DCE curves and estimate the vascular parameters associated with angiogenesis: perfusion (F), fraction of intravascular plasma volume (f_p), fraction of interstitial volume (f_{is}), and permeability surface area (PS). The contrast agent used was IsovueTM, an iodinated molecular with a molecular weight of 777, which is small enough to readily diffuse from the plasma volume into the interstitial volume while large enough not to cross the cellular membrane (see figure 1.3.8.2). By apply mass conservation; a set of coupled ordinary differential equations can be derived to represent the time-dependent contrast concentration within the intravascular and interstitial compartments.

$$\frac{dC_p(t)}{dt} = \frac{F}{f_p} \cdot \left[\frac{C_a(t)}{1 - Hct} - C_p(t) \right] - \frac{PS}{f_p} \cdot [C_p(t) - C_{is}(t)]$$

$$\frac{dC_{is}(t)}{dt} = \frac{PS}{f_{is}} \cdot [C_p(t) - C_{is}(t)]$$

In the above equations, $C_p(t)$ is contrast agent concentration in intravascular compartment, $C_a(t)$ represents the contrast agent concentration in the left ventricle or aorta, $C_{is}(t)$ is the contrast agent concentration in interstitial compartment, and Hct is the hematocrit. The CT intensity in a tissue voxel is the contribution from both the vascular and interstitial compartments:

$$C_{tissue}(t) = f_p \cdot C_p(t) + f_{is} \cdot C_{is}(t)$$

Once the DCE-CT images for $C_a(t)$ and $C_{tissue}(t)$ are acquired, a nonlinear least squares fitting algorithm is used to estimate the four physiological parameters.

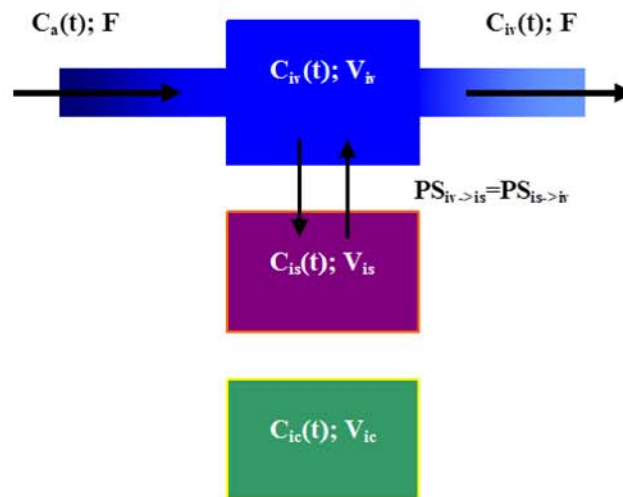


Figure 1.3.8.2 Schematic diagram of a two compartmental model to estimate tumor vascular physiology[126]. (Reprint permitted)

In summary, DCE-CT and PCT-S provides both intra-tumor vascular physiology (blood

perfusion, permeability, fraction of plasma volume, and fraction of interstitial volume) and hemoglobin status (hemoglobin concentration and oxygen saturation), from which the tissue oxygen concentration based on oxygen transport models can be obtained on a voxel-by-voxel basis. Dynamic contrast-enhanced computed tomography (DCE-CT) has been reliably used to quantify intra-tumor heterogeneity in vascular physiology for different tumors, including breast, pancreatic, ovarian, prostate and glioma cancer [127-129]. Similarly, photoacoustic CT spectroscopy has been used to measure the local distribution of SaO_2 and hemoglobin concentrations (C_{tHb}) in tumors. Given the similar spatial resolution of PCT-S and CT, the image volumes obtained from these modalities and their ability to highlight tumor vasculature (angiography) enables accurate image co-registration from these two modalities. Biophysical models will be used to fuse this information to obtain pO_2 levels.

1.4 Oxygen Transport Models

To develop a 3D assay of tumor hypoxia, a link between the microscopic (histology, invasive probes) and the macroscopic (imaging or scanner modalities) will need to be established. This will be accomplished through the use of oxygen transport models.

Oxygen and nutrient transport in the body occurs at a macroscopic and microscopic level. Macrocirculation is composed of the major arteries and veins, and rapidly transports oxygen and other substances toward or away from various organs.

Microcirculation consists of arterioles, capillaries, and venues and is responsible for the

delivery and exchange oxygen and nutrients within the surrounding tissue [130, 131]. Pathological microvascular is structurally abnormal or chaotic and highly dysfunctional, and is unable to deliver sufficient oxygen to tissues or tumors. Unlike other metabolic molecules, oxygen cannot be stored in the body (myoglobin in muscle is the only exception); hence, the adequate delivery of oxygen by the microcirculation system to the parenchymal cells at any given time is critical. Oxygen is either dissolved in plasma or bound to hemoglobin within red blood cells (RBC). Since oxygen has a low solubility in plasma, the majority of oxygen (98%) is carried via binding to hemoglobin. In addition to the blood hemodynamics, the topology of microvascular network, the barriers to oxygen diffusion barriers when crossing the vessel wall to the parenchymal cells, and oxygen metabolism rates all affect the local oxygen concentration.

A unique feature in the field of oxygen transport is the rich history of mathematical models. These models are simple in concept, where they are based on the physical laws of gas transport in fluids and mass conservation, but can also provide some predictive capability in determining tissue oxygen concentrations with modest input information. In many situations, it is difficult and sometimes impossible (depending on the extent of experiment) to conduct an experiment to simultaneously quantify the oxygen concentration and the relevant vascular physiology from a single vessel segment. Thus using a kernel of mathematical models can provide insight into the mechanisms of oxygen transport. August Krogh and Erlang first developed an ideal cylindrical model to study mechanisms of tissue oxygenation in a static or quiescent muscle almost a century

ago [132, 133]. Although Krogh had made a number of assumptions, the mathematical equations derived from his model set the stage for almost all subsequent theoretical works. Even with today's technology, the ability to simultaneously determine key biophysical or biochemical processes related to oxygen transport in microcirculation remains under investigation. However, the three key factors underlying these models of oxygen transport within tissue remain the same: (1) delivery and release of oxygen within the blood vessels, (2) diffusion of oxygen out of the blood vessels and into the parenchyma, and (3) rate of oxygen metabolism. An overview of these mechanisms is discussed, while the underlying foundations of our multivariate biophysical model of tissue oxygenation (MPO2) will be detailed in Chapter 3.

The main carrier and delivery mechanism of oxygen is through its binding and release from hemoglobin in blood. The hemoglobin protein has four subunits, each with a heme group and a globin chain. The heme group is composed of a porphyrin ring in which an iron (Fe) atom resides at its center, and can reversibly bind to oxygen. A normal adult human contains six different species of hemoglobins. Each share a similar principle function and structure, where hemoglobin-A makes up 92% of the total hemoglobin concentration. To date close to 200 structural variants of hemoglobin are known, where abnormal hemoglobin often has different oxygen binding relative to hemoglobin A. Hemoglobin binds up to four oxygen molecules. The nature of oxygen binding onto hemoglobin is cooperative (or allosteric), where the oxygen binding affinity to hemoglobin depends upon the existing bound oxygen. The release of oxygen from

hemoglobin in microvessels is controlled by many factors (pO₂, pH, temperature, concentration of carbon dioxide)[134]. A simplified mathematical form describing the binding kinetics is described by Hill's equation[134, 135].

$$SaO_2 = \frac{(pO_2/P_{50})^n}{[1 + (pO_2/P_{50})]}$$

In the equation above, the oxygen saturation index (SaO₂) refers to the fraction of oxygen molecular bound to hemoglobin, e.g., the fraction of oxygen 'receptors' occupied in a volume of blood. The pO₂ or oxygen partial pressure defines the oxygen concentration; the P₅₀ is the oxygen partial pressure at 50% of oxygen saturation; n is the Hill coefficient and describes the affinity of oxygen binding to hemoglobin.

Intravessel pO₂ is often estimated by Hill's equation when SaO₂ is known. Taken together, the SaO₂, pO₂, blood perfusion, and microvessel diameter are four major factors influencing the local availability of oxygen at any time in the micro vasculature.

From this equation, the release of oxygen (reverse binding to hemoglobin) occurs when blood plasma and tissue pO₂ are relatively lower. Gas exchange from the vessel compartment to the interstitial space takes place through oxygen diffusion and fluid transport mechanisms. For diffusion, the oxygen partial pressure (pO₂) gradient, the endothelial permeability to oxygen, and the blood vessel's surface area all contribute to the amount of oxygen diffused from microvessels to the tissue space. For fluid transport, the fluid exchange (Starling-Landis equation) due to differences in the hydrostatic and

osmotic pressures across the endothelium barrier of the blood vessels can carry the dissolved gases into the interstitial spaces. However, the second mechanism is commonly ignored because the amount of dissolved oxygen in plasma is significantly less than the oxygen released from hemoglobin. 50 years later, Duling and Berne provided the first systematic measurements of pO_2 using microelectrodes to test Krogh's model. They found a progressive longitudinal decline in perivascular pO_2 in arterioles proceeding capillaries as well as the capillaries [136-138]. Like any scientific investigation, their finding evoked more questions, for example why oxygen exchange occur in arterioles when oxygen exchange in capillary complex is adequate to provide oxygen and nutrients to surrounding tissue. This highlights the technical challenges in measuring key factors of oxygen transport. Contemporary thought accepted by the majority of researchers in the field of oxygen transport states that the oxygen diffusion pathway can occur between all three types of microvessels to the surrounding tissue and between any two types of microvessel segments (see figure 1.3.8.1). The regulation of local oxygen concentration from all possible diffusion and convection pathways and the physiological role of each pathway remain under investigation (figure 1.3.8.1).

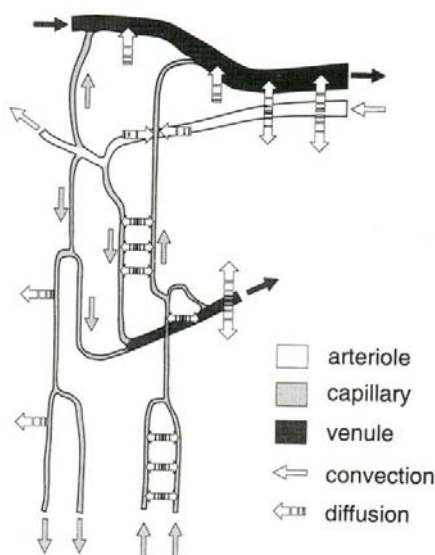


Figure 1.3.8.1 Schematic diagram of oxygen transport via diffusion/convection in terminal microvasculature(arterioles, capillaries, and venules)[139]. (Reprint permitted)

Finally, the rate of oxygen consumption of the tissue has a significant impact the oxygen gradient within the parenchyma and oxygen transportation rate from blood. Oxygen transport is a balance between the supply and demand of oxygen and nutrients, where the mitochondria consume most of the oxygen in the cells. In order to acquire the oxygen from blood, an oxygen tension gradient must exist between the vascular space and parenchyma tissue. Direct oxygen consumption (VO_2) can be measured by phosphorescence quenching microscopy (PQM, see Chapter 3) and the local rate of $d(pO_2)/dt$ quantified to determine VO_2 [140].

Overall, the principles behind oxygen transport within the microcirculation system is known (hemodynamics, physiology, diffusion lengths, metabolism rates), while the roles of many known proteins and regulatory mechanisms in oxygen transportation remain

unanswered (e.g., growth factors, cytokines, glutamine). Other areas of research in the field of oxygen transport remain under investigation, such as (i) the role microvessel structure in dictating the heterogeneous interstitial pO_2 profile; (ii) the contribution to the local tissue pO_2 by the arteriole network relative to the capillary network; and (iii) the importance of oxygen demand as modeled by Michael-Mentor kinetics and the impact on microcirculation. To address these challenges and many others in oxygen transport research, a look back in history demonstrates the importance of new and innovative diagnostic technologies and methods. For example, in 1628, William Harvey provided definite evidence that blood circulates within the body, but he did not know how the blood flowed from the artery to the vein and could not answer how gases and nutrients were delivered to the tissue. Harvey proposed the arterial blood poured into the flesh as into a “sponge” and find its way back to veins. It was over 30 years later, in 1661, when Marcello Malpighi used a microscope to discover the existence of capillaries within the lung of a frog, but he remained uncertain on the function of his great discovery. It took another 200 years until physiologists, such as Ernest Starley, August Krogh, and Eugene Landis, to understand the importance of the capillaries. Today thanks to technology, a clear understanding of the hierarchical structure of the microvasculature or lack thereof exists, but a complete understanding on the interplay between the microcirculation, oxygen transport and usage is lacking and requires more research. The ability to simultaneously measure and quantify pO_2 , hemoglobin status, and vascular physiology are the key to answering the above questions [141, 142].

1.5 A 3-D *in vivo* Assay of Hypoxia

Hypoxia has been shown to significantly impact clinical outcome, and its spatial-temporal variations can promote therapeutic resistance and metastasis. The *Gold Standard* method to measure oxygen concentrations is highly invasive, either through the use of needle-based probes or biopsy samples, and impractical. *In vivo* imaging methods, such as MRI or PET/SPECT, remain unavailable for clinical use or the lack temporal and spatial fidelity to characterize intra-tumor hypoxia. Other surrogate markers by themselves provide an incomplete picture. To enhance our understanding of hypoxia and in therapeutic interventions, a 3-D *in vivo* assay measuring intra-tumor oxygen concentrations is proposed. The long-term objective of this research is to characterize local regions within a tumor as diffusion- versus perfusion-based hypoxia, as acute versus chronic hypoxia, anemic-based, or as influenced by other microenvironmental features (interstitial hypertension, necrotic regions and transitional regions of necrosis, etc.). As a first step toward achieving these goals, a biophysical model is employed to fuse parametric maps of a tumor's physiological hemodynamics on a voxel-by-voxel basis. This assay will provide a multi-variable (multi-parametric) approach to quantifying oxygen concentrations, and thus provides a means to better differentiate the influence of therapeutic targets and protocols. Ultimately, this assay will be combined with immunohistochemistry (IHC) images to provide an advanced causal analysis linking the hypoxic microenvironment to biomolecular mechanisms while undergoing therapy, thus bridging the gap between bench top discoveries and clinical realization through the use of image-guided therapy.

Experimental methods to study oxygen transport are discussed at two different scales: (1) microscopic resolution in which optical techniques are the dominant approach to characterize vessel structure/functional properties in μm resolution, and (2) macroscopic resolution in which different *in vivo* imaging techniques are used (MRI, CT, PET). The microscopic measurement is a powerful tool capable of providing insight on the action of oxygen transport mechanism, but severely limited in its clinical use. *In vivo* imaging techniques cannot offer resolution afforded by microscopic techniques but are capable of monitoring the *noninvasively* vessel and tissue function over a tumor volume. Therefore, this study aims to develop a multivariate biophysical oxygen transport model which estimates oxygen status with structural and hemodynamic inputs (such as fraction of vessel volume and blood flow) acquired from contrast-enhanced imaging modality and photoacoustic spectroscopy and fuses this information to determine local oxygen concentrations (pO₂) (Chapter 3). To validate this fusion-based model dubbed MPO₂, hemodynamic data and models obtained from the literature (GPO₂) were compared to the accuracy, precision, and quantification of the MPO₂ model, where scanner resolution and noise were simulated (Chapter 4). Next, MPO₂ model was applied to *in vivo* preclinical tumor data and compared to OxyLite probe measurements of pO₂ (Chapter 5), and finally to a therapeutic study where pancreatic xenograft tumors were treated with the ant-angiogenic monoclonal antibody DC101 (VEGFR2 inhibitor) (Chapter 6). The results from these studies are discussed in Chapter 7, and future studies proposed.

CHAPTER 2. SPECIFIC AIMS

Hypoxia, and the etiology of hypoxia, can infer metastasis and therapeutic resistance in cancer patients. A key factor influencing the delivery of oxygen is the vasculature formed during tumor angiogenesis. Over the past three decades, drugs targeting angiogenic pathways have been developed, but with little or no success in improving the overall survival in patients. Application of anti-angiogenic therapy (AAT) has been shown to increase hypoxia and antagonize traditional cytotoxic therapies, such as radiation therapy and chemotherapies. Recent studies also demonstrate a decrease in hypoxia (increase in radiation therapy and chemotherapy) after the application of anti-angiogenic drugs. Given the varied response of these drugs on tumor oxygenation, diagnostic methods can provide valuable information to diagnose and guide therapy. A number of techniques have been reported to image hypoxia (or pO_2) or a feature or two associated with hypoxia; however, these methods lack the ability to measure the underlying vascular physiology and hemodynamics leading to hypoxia with the necessary spatial-temporal fidelity. **To investigate the role of hypoxia and oxidative stress in cancer biology and therapy, a novel in vivo 3-D oxygenation assay that quantifies oxygen concentrations and provides maps of tumor hypoxia maps within a tumor.**

The method combines two key components: (1) the ability to measure the local microvascular physiological hemodynamics using functional and molecular imaging modalities, such as Dynamic Contrast-Enhanced Computed Tomography (DCE-CT) and Photoacoustic Computed Tomographic Spectroscopy (PCT-S); and (2) the development of a biophysical oxygen transport model that fuses the multiple parametric maps obtained from functional and molecular imaging to calculate local pO_2 . Once these models have been validated, they will be tested under different anti-angiogenic regimes to anticipate tumor oxygenation and response to radiation therapy. To accomplish these objectives, we propose to:

Specific Aim 1: Develop and simulate the pO_2 distribution in normal tissue and tumor at microscopic and macroscopic level, and evaluate the influence of spatial resolution and noise on the accuracy and precision of pO_2 .

The goal of this specific aim is to determine the most accurate and precise mathematical model of oxygen transport in *normal* and *abnormal* tissue. This model and the corresponding measurements have a dependency on the spatial resolution (voxel size) and signal-to-noise (sensitivity) of the imaging modality. First, tumor and brain tissue vasculature, both vascular structure and function, are artificially generated based on microscopy measurements obtained from the literature, and pO_2 distributions calculated based on Green's solution to oxygen transport equations (Gold Standard or control). Second, imaging maps of perfusion, fractional plasma volume, fractional

interstitial volume, oxygen saturation, and hemoglobin concentration are formed at different voxel sizes (spatial resolution). Third, a modified Krogh cylindrical model is used to fuse the imaging information to obtain pO_2 maps within these tissues. The voxel-based pO_2 values are compared between the microscopic solution using Green function solution (GPO₂) and the image-based multivariate Krogh cylindrical model (MPO₂). The accuracy and precision of these pO_2 calculations based on measurement errors and spatial resolution are assessed.

Specific Aim 2: Compare in vivo imaging of tumor vascular physiology and hemodynamics to OxyLite probe measurements of pO_2 .

The goal is to perform PCT-S and DCE-CT imaging in a mouse model of cancer, acquire OxyLite probe measurements of pO_2 , and compare the measured pO_2 values to calculated value for different voxel-based mathematical models. Breast tumors (MCF-7, MCF-7VEGF, MDA-MB-231) growing in the mammary fat pads of athymic nude mice will be imaged to obtain tumor physiology (F, PS, fp, fis) and hemoglobin status (CtHb, SaO₂). Immediately after scanning, the OxyLite probe will be used to measure local pO_2 levels in the tumor along a central axis of the tumor. These measurements will be compared to in vivo data and MPO₂ results.

Specific Aim 3: Assess the predictive capability of the in vivo 3-D assay in combined anti-angiogenic therapy and radiation therapy.

The objective of this specific aim is to analyze therapeutic data of mice receiving both anti-angiogenic therapy and radiation therapy. Two cohorts of mice with pancreatic (BxPC-3) tumors will be treated with low and high doses of an anti-angiogenic drug, DC101. One-week post AAT, these tumors will be treated with 5Gy of X-ray radiation. These tumors will be imaged using DCE-CT and PCT-S, and the voxel-based mathematical model (MPO2) will be employed to calculate the pO₂ maps prior to AAT and prior to RT. These maps will be compared to the tumor volume response curves to ascertain the radiosensitivity of the tumors, and if MPO2 assay is consistent with therapeutic response.

CHAPTER 3. TUMOR MICROVESSEL STRUCTURE AND FUNCTION AND ASSOCIATED MATHEMATICAL MODELS OF OXYGEN TRANSPORT

The purpose of this study is to develop a multivariate mathematical model to estimate local pO_2 (MPO2 method) in a finite volume voxel. To verify this model, a reference or control is required. This reference utilizes microscopic data obtained from the literature (Section 3.1) and a Green's function algorithm to solve the set of coupled ordinary differential equations (ODE) of oxygen transport to obtain microscopic levels of pO_2 , which was shown to correlate with measurement (Section 3.2.1). Next, this same information was used to simulated in vivo image data that was used to test the MPO2 model (Section 3.2.2). In this chapter, an overview on the how the detailed microvascular structure and functional data was acquired by various optical techniques is discussed. Next, the use of microelectrodes to quantify pO_2 (Gold Standard) and validation of Green's function algorithm is presented. Finally, simulated parametric images of vascular physiology and hemodynamics are presented and the MPO2 model derived. The development of these techniques is used to investigate the specific aims outlined in Chapter 2.

3.1 Vascular Structure of the Reference Tissues and its Function

3.1.1 Window Chamber Animal Model for 3D Optical Tumor Vessel Imaging

Window chamber models and tumor transplants of SCID mice are two animal models often used to study the microvascular structure and microcirculatory function in tissue and tumors (see figure 3.1.1) [143-146]. These models provide real-time observations over time of the microvessel structure and function in living animals using optical techniques (e.g., intravital, confocal and two-photon microscopy), such as a vessel's segment length, diameter, and branching angle. When combined with fluorescence microscopy and phosphorescence quenching, functional data including blood flow, pO_2 and pH can be obtained [147-149]. However, window chamber models have a number of disadvantages, such as they are technically difficult to perform and maintain, requires specialized microsurgical skills and animal housing, and limits in the size of the tumors (<3 mm in diameter and <500 μm in thickness), which raises the question of whether they accurately represent oxygen transport in large tumors. Therefore, subcutaneous or orthotopic animal models provide a more realistic model to study oxygen transport mechanisms in large solid tumors; however, other methods beyond optical imaging must be developed.

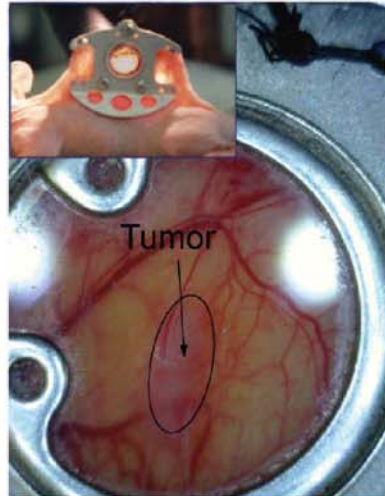


Figure 3.1.1.1: The window-chamber model consists of a titanium metal frame, which holds the dorsal skin fold in place. The front skin flap is excised, and tumor cells are injected into the back plane of the opposing side skin and covered by a round coverglass. The inset shows the mouse with window implanted, with a larger view of the window itself[150]. (Reprint permitted)

3.1.2 Methods Used to Quantify Microvascular Structure and Function

In Table 3.12.1, a combination of methods is used to quantify microvascular structure, and local physiology and hemodynamics. Optical techniques, such as confocal or two-photon microscopy, provide *in vivo* measurements of the microvascular geometry (diameters, segment lengths) and topology (branching angles) using the window chamber technique, but is limited to a small region of interest (ROI) [151, 152]. Other methods, such as fluorescence confocal and two-photon microscopy, measure a vessel's blood flow and oxygen saturation level [153-155], and through the use of video microscopy, hemodynamic data (blood flow and Hct) are obtained after an intravenous injection of an intra-vascular fluorochrome. Even though magnetic resonance microscopy can provide angiographs at depth, it has a minimum voxel size of 50 μm and

unable to clearly demark microvessel segments and provide hemodynamic information [149]. Similarly, micro-CT provides excellent spatial resolution of the microvascular structure within a tumor but can only be done *ex vivo* [156, 157].

The blood flow data with an individual blood vessel are obtained from labs that implement dual slit method and/or fluorescence-labeled RBCs. The dual slit method [158, 159] utilizes a cross-correlation technique to calculate the time-of-flight between video frames, where the traveling distance of a RBC is determined within two slits on the screen. The RBC velocity is equal to the ratio of the distance the RBC traveled (two slits) and the corresponding time-of-flight. This method also quantifies the local hematocrit by measuring the diameter of each vessel segment (total vascular volume). An alternative method to measure blood flow within an individual vessel segment is to use fluorescently labeled RBC [160, 161]. Approximately 0.5 to 1.0% of RBCs withdrawn from a donor animal is fluorescently labeled and injected back into the animal. RBC velocity is measured by determining the time-of-flight of individual RBC using video microscopy, and the RBC flux is measured by counting the number of fluorescently labeled cells that pass through a microvessel as a function of time. The hematocrit can also be determined if vessel diameter and RBC size are measured. The reason for determining the RBC flux (or blood perfusion) is that it is related to the intravascular pO_2 and not the RBC velocity [147]. The disadvantage of fluorescently labeled RBC method includes the extensive video microscopy image analysis to obtain the desired

parameters. Both methods require anesthesia to the animals which could significantly reduce hemodynamics [162].

Table 3.1.2.1: Methods to study detailed microcirculation structure and hemodynamics[95].

Microvascular Geometry			
Method	Endpoint	Advantage	Disadvantage
Confocal/two-photon microscopy	Vessel orientation/density	Full 3-D orientation	Laborious; limited ROI
Contrast-enhanced micro-CT	Vessel orientation/density	Full 3-D orientation	No concomitant functional data; laborious to inject Microfill contrast agent; ex vivo only
Magnetic resonance microscopy	Vessel orientation/density	Full 3-D orientation	No concomitant functional data; limit on voxel size $\sim 50 \mu\text{m}$; weak sensitivity; issue of high magnetic field
Microvascular hemodynamics			
Method	Endpoint	Advantage	Disadvantage
Dual slit photometry	RBC velocity; blood flow rate; flow direction	Automated; real time data, not technical difficult	Cannot get hematocrit and red cell flux
Fluorescent-labeled RBC	RBC velocity; blood flow rate; flow direction; RBC flux; hematocrit	All micro-hemodynamic parameters are obtainable	Not real time; need playback tape; time consuming

3.1.3 Intravascular pO_2 Determination (PQM and Microelectrode Method)

In this section, two popular methods used to quantify the intravascular pO_2 with micrometer resolution are phosphorescence quenching microscopy (PQM) and oxygen-sensitive microelectrodes. Phosphorescence quenching microscopy or PQM was developed by Wilson and his colleagues to measure the local pO_2 in vivo implementing a phosphor probe [163-165]. The phosphor is excited by a brief pulse of light in a finite volume close to $10 \mu\text{m}$ in diameter, and then decays to its ground state by emitting a

photon (phosphorescence) or transferring energy to a nearby oxygen molecule (collisional quenching). The phosphorescence decay is a linear function of oxygen concentration: $K = K_0 + K_q \cdot pO_2$ (Stern-Volmer equation), where K is the phosphorescence decay constant, K_0 is the rate constant in the absence of oxygen, and K_q is the quench constant. Both K_0 and K_q are temperature and pH sensitive (see figure 3.1.3.1-A). The microscope optics remain at the same location over a period of time in order to acquire an intensity decay curve (see figure 3.1.3.1-B), and from the phosphorescence lifetime and intensity, oxygen concentration can be determined [166].

In a typical intravascular pO_2 measurement, palladium-mesotetra-(4-carboxyphenyl)-porphyrin (Porphyrin Products, Logan, UT) is injected into the blood stream and binds to albumin or polythylene glycol, thus remaining in the circulation. This method produces accurate measurement at low pO_2 but becomes unreliable if the pO_2 exceeds 50 mmHg. Leaking of Porphyrin from blood to surrounding tissue (e.g., tumor) after long circulation contributes has been shown to increase the measurement error.

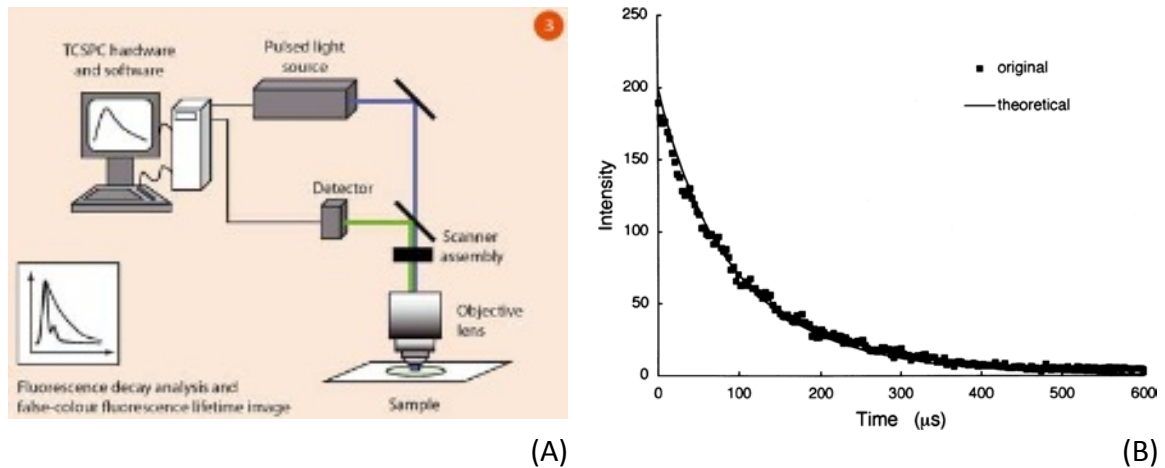


Figure 3.1.3.1.A-B: (A) Schematic illustration of Phosphorescence Quenching Microscopy[167]. (B) A typical example of a digitized phosphorescence decay curve measured in the interstitial space of rat cremaster muscle, the decay constant is extrapolated from the decay curve[167]. (Reprint permitted)

An alternative method is the use of oxygen microelectrodes. This technique is based upon the electrochemical reduction of intravascular pO_2 and also provides micrometer resolution [168-170]. The electrodes are placed on the tip of needle and inserted into the tissue. This can potentially damage the tissue and perturb the local oxygen status. This becomes significant if the probe penetrates the vessel wall in order to measure the intravascular pO_2 or when the probe affects or hinders blood flow and RBC flux. Another concern is the oxygen consumption from the probe itself ($10^{-6} \mu\text{L/min}$), which alters the local oxygen concentration during the measurement. Guidance or visualization of the probe in the tissue to verify the position inside vessels is often recommended.

3.1.4 Interstitial Tissue pO₂ Determination (PQM and Microelectrode Method)

Interstitial tissue pO₂ measurement can be carried out by oxygen microelectrodes or modified PQM method with specific Oxyphor probes. The modified PQM method developed by Wilson *et al* integrates an 635 nm excitation light guide (1 mm in diameter) and a second light guide used to collect 695 nm emissions (4 mm in diameter). The probes are positioned against the surface of skin (by drawing a grid on the skin) (figure 3.1.4.1-B). The excitation light diffuses through the tissue and stimulates phosphorescence of phosphor probe (R2 or G2 probes; i.v. injected). The emitted phosphorescence diffuses through from the tissue to the location where collection guide is placed and is measured. The contribution of final pO₂ measurement comes from the “banana-shaped” region from phosphorescence excitation optical fiber to collection optical fiber (figure 3.1.4.1-A). The “tissue pO₂” is the average pO₂ from intracellular, interstitial, and nearby intravascular compartments along the light path [171, 172]. This method assumes the tissue pO₂ is the main contributor to the measurement; however the authors could not provide definitive evidence to justify their claim. Additionally the spatial resolution of tissue pO₂ is poor considering large diameter guides are used in experiment. Thus the pO₂ measurement by microelectrodes is clearly more accurate but it is laborious. Hence depending upon the tumor size microelectrode method might not be a practical choice to profile interstitial pO₂ in entire tumor.

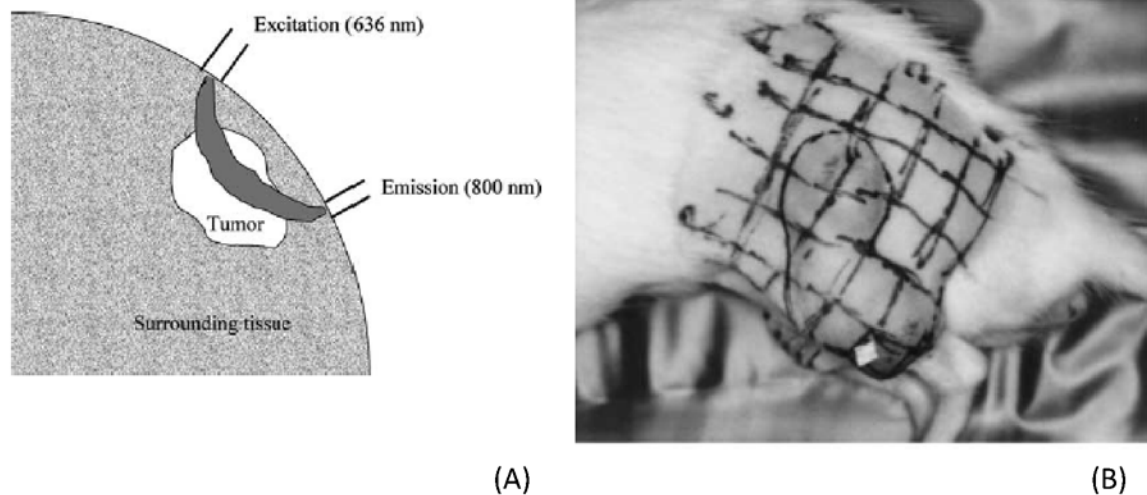


Figure 3.1.4.1.A-B: (A) Schematic representation of the pO₂ measurement in tumor-bearing rat *in vivo* using near-infrared light[172]. (B) Oxygen measurements in anesthetized Fisher rat with a subcutaneous 9L glioma tumor. A 6x5 grid is marked on the tumor skin to locate the excitation and emission light guides. (Reprint permitted for both figures)

3.1.5 Intravascular SaO₂ and Hemoglobin Concentration

Optical microspectrophotometry can measure the SaO₂ and hemoglobin concentration in every vessel segment within a vascular network by implementing intravital video microscopy. The principle of microspectrophotometry is identical to photoacoustic spectroscopy which leverages the difference in the absorption spectra between oxy- and deoxy-hemoglobin to estimate oxygen saturation and hemoglobin concentration [173-175]. Optical microspectrophotometry as with many other optical techniques is very laborious process and sensitive to vibrations (or motion). In Vivo quantification of SaO₂ using these methods is a relatively new, and can provide a noninvasive and reliable measurement in both thin tissue and solid organ [176, 177].

To obtain both structural and hemodynamic information, the data compiled from all of the above techniques were obtained from the literature and used in our simulations. The measurements have been adapted by several groups to study or to simulate the microvasculature behaviors or oxygen level in various organs[149, 178]. In the next section, the mathematical models used to simulate the pO_2 distribution in tissue are discussed, where these measurements are used as input parameters. In Table 3.2.1, the vascular structure parameters and hemodynamic values obtain from these studies are listed.

3.2 Mathematical Models of Oxygen Transport

As previously described, the interplay between theoretical models and experimental data, in particular *in vivo* imaging, has greatly enhanced our understanding of oxygen transport and the impact on therapeutics. With recent advances in *in vivo* micro imaging modalities (preclinical imaging), the concept of 3-D *in vivo* assay that combines mathematical modeling and high-resolution functional and molecular imaging to map oxygen levels and characterize tumor hypoxia can be realized. To test the feasibility and identify potential limitations, biophysics models and computation models are employed at the microscopic level, on the order of 1-10 μm and compared to the macroscopic level, on the order of 50-300 μm . For the former, a combination of confocal imaging and Green's function algorithm (GPO2-model) is used to calculate the oxygen level at the 10

μm level, while a multivariate solution based on a modified Krogh model (MPO2-model) is used to calculate pO_2 levels using in vivo imaging techniques as shown in figure 3.1.5.1.

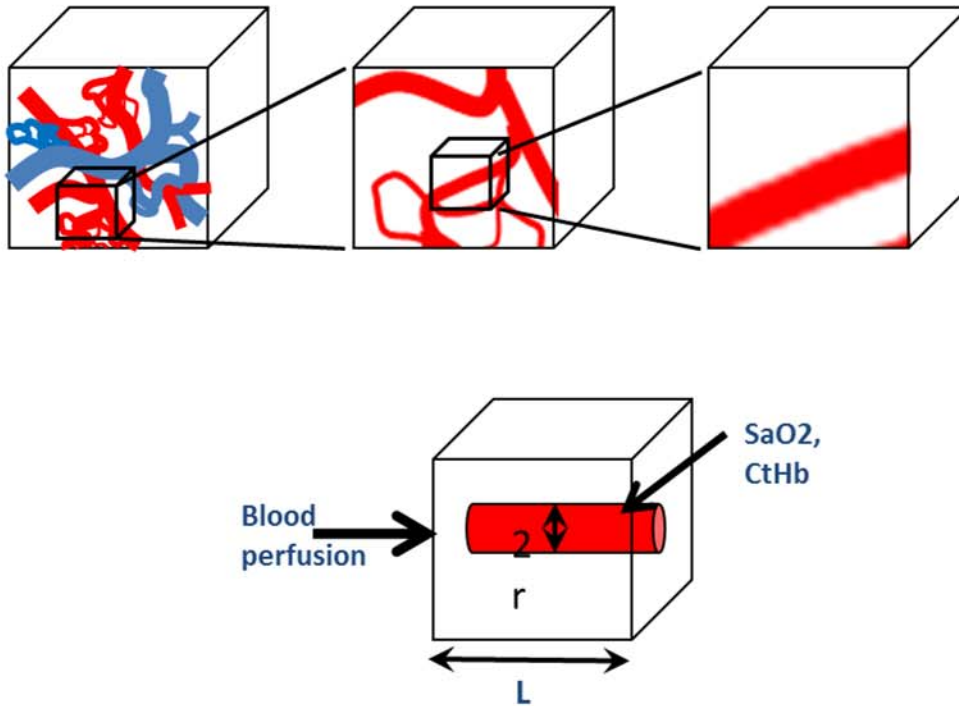


Figure 3.1.5.1: Schematic illustration of vessel complexity to voxel size. Tumor microvasculature is overall structurally tortuous and chaotic. To represent both structural and functional aspects of a vessel network inside a large voxel by an effective microvessel is problematic as shown on top-left corner. The complication of vessel tree confined in a volume is reduced as voxel size is decreased (the top-middle cartoon). As the volume of voxel becomes appropriate, the vessel configuration inside the voxel is comparable to an off-center single vessel configuration illustrated on top-right cartoon. Hence adapting a Krogh-based oxygenation model to estimate average pO_2 in a voxel is obtainable. MPO2 places the effective single vessel at the center of voxel and considers oxygen source (blood flow, SaO_2 , C_{tHb} , vessel diameter) as well as consumption (cell oxygen consumption rate, fraction of cell volume) attributes to determine the tissue oxygen level.

3.2.1 Green's Function Method to Calculate Tissue pO_2 by 3D Vasculature

Equations and Assumptions of Green's Function Method. The classical Krogh model

assumes the microcirculation network is composed of parallel, evenly spaced capillaries,

thus the tissue pO_2 can be estimated by an ideal cylindrical vessel model. This assumption is adequate for the skeletal muscle, where the capillaries run parallel to muscle fibers. However, in other organs, this assumption is no longer valid. Clearly, an oxygen transport model must consider the complexity of the vessel network topology. To deal with this complexity, Hsu and Secomb developed an approach where each vessel is represented as a distribution of oxygen sources within a defined tissue region. The local oxygen concentration is the sum of the pO_2 from those sources. There are several key assumptions in Green's function method: (1) the entire system is in a thermodynamically static state, (2) oxygen solubility and diffusion constants are homogeneous and isotropic, (3) myoglobin assisted oxygen transport is ignored, (4) a linear relationship between oxygen concentration and pO_2 in tissue is assumed (Henry's gas law), (5) a nonlinear relationship exists between pO_2 and oxygen consumption rate in tissue as defined by the Michaelis-Menten equation, (6) the cooperative binding of oxygen to hemoglobin exists as defined by Hill's equation, and (7) the transient pO_2 exchange between the RBCs and plasma is replaced by an average pO_2 (P_b) in vessel lumen. The impact of these assumptions is discussed.

Two coordinate systems are used in formulating the mathematical equations in tissue and in blood vessel (figure 3.2.1.1). A Cartesian coordinate system(x_1, x_2, x_3) is used to describe the tissue space, the oxygen concentration in tissue space is denoted by $C_t(x_1, x_2, x_3)$ or $P_t(x_1, x_2, x_3)$ which satisfies

$$D\nabla^2 C_t = M(P_t) \text{ or } D\alpha\nabla^2 P_t = M(P_t) \quad (1)$$

where D is the oxygen diffusivity, ∇ denotes the Laplacian, and $M(P_t)$ is the local metabolic rate. Note that the oxygen concentration is linearly related to oxygen partial pressure $C_t = \alpha P_t$ where α is oxygen solubility in tissue. In the vessel compartment, the oxygen reserve is the sum of bound oxygen and dissolved oxygen. Under normal conditions, the dissolved oxygen is much less than bound oxygen and is neglected. Therefore, the total available oxygen in blood is

$$C_b = HC_0 S(P_b) \quad (2)$$

$$S(P_b) = P_b^n / (P_b^n + P_{50}^n) \quad (3)$$

where H is hematocrit, C_0 is the fully saturated hemoglobin concentration, $S(P_b)$ is hemoglobin saturation, and P_b is the intravascular oxygen partial pressure. Notice that equation (3) is Hill's equation, and describes the cooperative binding of oxygen to hemoglobin. The rate of oxygen efflux per unit length along a vessel segment is denoted by $q(z)$. The conservation of mass implies that

$$F dC_b/dz = -q(z) \quad (4)$$

where F is the blood flow. The efflux is calculated by integrating around the radius of the vessel segment, r_0 :

$$q(z) = -D\alpha \int_0^{2\pi} r_0 \left(\frac{\partial P_b}{\partial r} \right) d\theta$$

For a vessel delivering oxygen, $q(z)$ exceeds the local tissue pO_2 at the interface with the blood. This relationship can be represented by the following equation as suggested by Hellums [179],

$$P_t(z) = P_b(z) - Kq(z) \quad (5)$$

where K is constant related to vessel radius. Equation (2), (4), and (5) can be combined as following:

$$FHC_0 \frac{d}{dz} S(P_t(z) + Kq(z)) = -q(z) \quad (6)$$

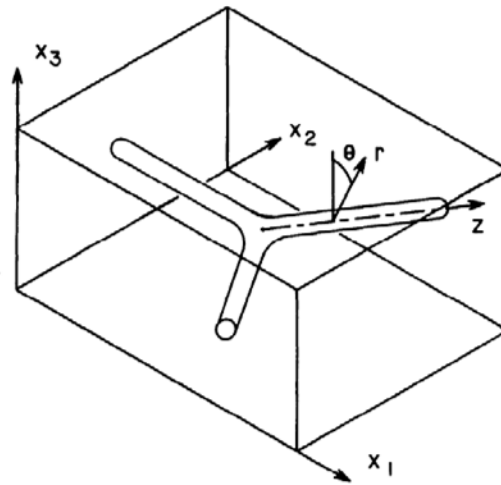


Figure 3.2.1.1: Coordinate systems: Cartesian system (x_1, x_2, x_3) for tissue space: local cylindrical polar system (r, θ, z) for one vessel segment).

There are several numerical methods to solve secondary partial differential equation (1). Finite-element methods lead to a large number of unknown parameters and require a 3-D grid or mesh capable of resolving individual blood vessels. Another approach is to consider each vessel segment as a part of a long vessel segment connected to an oxygen

source, similar to the electrons within an electric potential (or circuit). According to potential theory [180], the Green's function $G(x; x^*)$ is defined as the tissue pO_2 at a point $x=(x_1, x_2, x_3)$ resulting from a unit point source at x^* ,

$$\nabla^2 G = -\delta(x - x^*) + 1/V, \quad (7)$$

where δ represents the three-dimensional Dirac delta function and V is the entire tissue region volume. Since equation (1) is linear and Green's function is additive, Green's function can be decomposed into $G = G_1 + G_2$, where $G_1 = 1/|x - x^*|$ is the solution for point source ($\nabla^2 G_1 = -\delta(x - x^*)$) and G_2 is the solution for the constant term $1/V$ ($\nabla^2 G_2 = 1/V$) ($G_2 = c_1 x_1 + c_2 x_2 + c_3 x_3 + d_1 x_1^2 + d_2 x_2^2 + d_3 x_3^2$). The coefficients are determined by setting $G = G_1 + G_2$ and applying setting the net diffusive flux across each of the six boundary planes to zero,

$$\int_{\text{All surfaces}} \frac{\partial}{\partial n} (G_1 + G_2) dS = 0 \quad (8)$$

Given the kernel function $G = G_1 + G_2$, Green's function solution to equation (7) is

$$pO_2(x_1, x_2, x_3) = \int_{\text{sources}} G(x, x^*) q(x^*) dx^* \quad (9)$$

where $q(x^*)$ is the source distribution which includes positive source (oxygen supply) and negative source (oxygen sink).

Numerical Solution to Green's Function Algorithm. Blood vessels are discretized into m short segments and the tissue space is discretized into n small cubic regions. For the simulations performed in the specific aims, the distance between the centers of these

cubic regions is 15 μm . According to equation (9), the average pO2 at the blood-tissue interface of segment i and in tissue region i are

$$P_{b,i} = \sum_{j=1}^m G_{ij}^{bb} q_j + \sum_{j=1}^n G_{ij}^{bt} \varphi_j \quad \text{for } i = 1, \dots, m \quad (10)$$

and

$$P_{t,i} = \sum_{j=1}^m G_{ij}^{tb} q_j + \sum_{j=1}^n G_{ij}^{tt} \varphi_j \quad \text{for } i = 1, \dots, n, \quad (11)$$

where q_j represents the source strength of segment j and φ_j represents the (negative) source strength in tissue region j .

$$P_{b,i} = P_{c,i} - Kq_i \quad \text{for } i = 1, \dots, m \quad (12)$$

where $P_{c,i}$ is the intravessel pO2 at the midpoint of segment i . The oxygen consumption φ_j is represented by the Michaelis-Menten equation,

$$\varphi_j = -M_0 \frac{P_{t,j}}{(P_{50} + P_{t,j})} \quad \text{for } j = 1, \dots, n, \quad (13)$$

where M_0 is the maximum oxygen consumption rate; P_{50} is the pO2 at half of maximum consumption rate M_0 . To find $P_{c,i}$, equation (4) is integrated. It is calculated based on the rate of oxygen transport due to convective forces along the length of the vessel segment relative to its midpoint $f(P_{c,i})$, which can be expressed as a linear function of source strength q_j .

$$f(P_{c,i}) = f(P_{c,i}^0) - \sum_{j=1}^m \sigma_{i,j} q_j \quad (14)$$

$$P_{c,i} = f^{-1}(f(P_{c,i}^0) - \sum_{j=1}^m \sigma_{i,j} q_j) \quad (15)$$

Here, $P_{c,i}^0$ is the intravascular pO₂ of segment i in the absence of diffusive oxygen exchange, that is $q_j = 0$ for all j . For a series of segments forming a vessel without branches, $\sigma_{i,j}$ is equal 1 if segment j is upstream of segment i , 0 if segment j is downstream of segment i , and 0.5 when $i = j$. By combining equations (10), (12), and (15), the following nonlinear equation is used to determine pO₂ at each grid point:

$$\sum_{j=1}^m G_{ij}^{bb} q_j - f^{-1}(f(P_{c,i}^0) - \sum_{j=1}^m \sigma_{i,j} q_j) + K q_i = - \sum_{j=1}^n G_{ij}^{bt} \varphi_j \quad \text{for } i = 1, \dots, m \quad (16)$$

Initial estimates of tissue oxygen levels and vessel source strength are first defined, and tissue oxygen strength φ_j was calculated by using equation (13). The left hand side equations are solved together with net oxygen delivery equal to consumption equation ($\sum_{j=1}^m q_j + \sum_{j=1}^n \varphi_j = 0$) by biconjugate gradients stabilized method [181], giving updated values for q_i . The procedure is repeated using the updated values until convergence to a specific criterion is reached. Equation (11) with updated φ_i and q_i is used to calculate tissue pO₂. This procedure is also repeated after receiving updated vessel pO₂, φ_i , and q_i until convergence is reached.

Description Of 3D Microvasculature Data Source. In this study, the correlation of Green's function pO₂ (GPO₂) to the multivariate modified Krogh pO₂ (MPO₂) is evaluated within the brain (reference tissue) (0.15mm x 0.16mm x 0.14mm) and a tumor (1mm x 1mm x

0.15mm). Both structural and rheological data was obtained for each individual segment as reported by Dewhirst et al (<http://www.physiology.arizona.edu/people/secomb/network>) and Fonteanella et al [94, 161]. Briefly, each individual vessel segment in the network was represented by an ideal cylinder, where the diameter was assumed to be uniform and the blood flow and hematocrit (Hct) remained constant.

3.2.2 MPO2 Method to Calculate Tissue pO_2

Derivation of the MPO2 Model. The multivariate single vessel oxygen transport model, or the modified Krogh oxygenation model, shares many assumptions and governing principles with Green's function algorithm [135]. For example, the oxygen distribution in the tumor is dominated by diffusion; therefore, the oxygen partial pressure pO_2^T satisfies (see equation (1))

$$D \nabla^2 pO_2^T = H M(pO_2^T) \text{ where } M(y) = \frac{M_0 y}{p_0 + y},$$

where D is the oxygen diffusion constant, H is Henry's constant, and M is the tissue oxygen consumption rate, which follows Michaelis-Menton kinetics (M_0 is the maximum oxygen consumption constant and p_0 is the pO_2 at half-maximal consumption constant). For a single cylindrical vessel placed at the center of the voxel, the above equation can be written in cylindrical coordinate as

$$D \left[\frac{1}{r} \frac{\partial}{\partial r} \left(r \frac{\partial pO_2^T}{\partial r} \right) \right] = H M(pO_2^T) \quad (17)$$

where r is the radial distance from the center of cylinder and z is the vessel length. Note, this solution ignores the second derivative with respect to z .

Within the blood vessel, the bound oxygen is released based on the plasma pO_2 based on the hemoglobin dissociation curve. Thus the dissolved oxygen concentration in plasma, $C(r, z)$, is formulated as function of diffusion process (D), blood flow (F), and oxygen released from hemoglobin,

$$F \frac{\partial C}{\partial z} = D \left[\frac{1}{r} \frac{\partial}{\partial r} \left(r \frac{\partial C}{\partial r} \right) + \frac{\partial^2 C}{\partial z^2} \right] + R$$

Here R is the deoxygenated hemoglobin production rate, which is proportional to the dissolved oxygen concentration in plasma. The saturated hemoglobin concentration $C'(r, z)$ bound to the hemoglobin within the RBCs is represented by the following equation:

$$F \frac{\partial C'}{\partial z} = R'$$

where R' is the oxygenated hemoglobin production rate (Hill's equation). These two differential equations can be combined to form

$$F(1+m) \frac{\partial pO_2^B}{\partial z} = D \left[\frac{1}{r} \frac{\partial}{\partial r} \left(r \frac{\partial pO_2^B}{\partial r} \right) \right] \text{ where } m = n P_{50}^n H \lambda_{sat} \frac{(pO_2^B)^{n-1}}{(P_{50}^n + (pO_2^B)^n)^2},$$

where pO_2^B is the oxygen partial pressure in blood, λ_{sat} is the saturated hemoglobin concentration, n is the average oxygen bound to hemoglobin, and P_{50}^n is the partial

oxygen pressure when the oxygen saturation(SaO₂) is equal to 50%. At the boundary between the vessel wall and tissue, the oxygen partial pressure and its first derivative are required to be continuous.

$$pO_2^B = pO_2^T = pO_2 \text{ and } \frac{\partial pO_2^B}{\partial r} = \frac{\partial pO_2^T}{\partial r} = \frac{\partial pO_2}{\partial r} ; \text{ at } r = r_c$$

Therefore, the final expression for the pO₂ is

$$pO_2(r, z) = pO_2(z) - \frac{r_c^2 M H}{4D} \left[1 - \left(\frac{r}{r_c} \right)^2 \right] - \frac{r_T^2 M H}{2D} \ln \left(\frac{r}{r_c} \right) \quad (18)$$

$$pO_2(z) = pO_2(z=0) - \frac{M H}{(1+m)F} \left[\left(\frac{r_T}{r_c} \right)^2 - 1 \right] z \quad (19)$$

In principle, the initial pO₂ value is evaluated from SaO₂ which can be measured by PCT-

S. All simulation parameters of MPO2 model are listed in table 3.2.2.1.

Table 3.2.2.1 Simulation parameters used in MPO2

Parameter	Value	References
Oxygen consumption rate, M_0	$30 \mu\text{L}/\text{g}.\text{min}$	[182]
Blood flow rate, F , in sensitivity analysis	$0.15 \text{ mL}/\text{g}.\text{min}$	In-house DCE-CT data
Hct	0.4	
Vessel radius r_c in sensitivity analysis	$5 \mu\text{m}$	[182]
Saturated hemoglobin concentration C'	$8800 \mu\text{M}$	[134]
CtHb-PCT([Hb] from PCT-S)	3.0 g/dL	In-house PCT-S data
P_{50}	26 mmHg	[134]
n	3.0	
Henry's constant, H	$0.74 \text{ mmHg}/\mu\text{M}$	[135]
Oxygen diffusion constant D	$2000 \mu\text{m}^2/\text{sec}$	[183]
Oxygen solubility in blood	$0.0385 \mu\text{l}/\text{g}.\text{mmHg}$	[184]

CHAPTER 4. MPO2 PERFORMANCE AT VARIOUS VOXEL SIZES

In last chapter, the techniques used to acquire detailed microvasculature structure and associated hemodynamics was discussed. The fundamental principle and implementation of the Green's function algorithm used to calculate the microscopic pO_2 profile from the above data and of MPO2 model used to calculate the average pO_2 in a voxel were derived. This objective of this chapter is to evaluate the accuracy and precision of the MPO2 model at various voxel sizes and noise levels for brain and tumor tissue, where Green's function pO_2 (GPO2) was used as a reference.

4.1 MPO2 Validation Method Using Green's Function as Standard

4.1.1 Implementation of a Virtual Voxel Grid

Prior to applying a virtual voxel-based grid, the pO_2 distribution within the tumor and brain tissue was calculated using the Green's function algorithm (Chapter 3). The virtual grid is composed of isotropic voxels interspersed within the entire tissue volume (see figure 4.1.1.1 for 2D demonstration).

Since the diameter, length, hematocrit (Hct), and blood flow of each vessel segment were known, the fraction of vessel volume, hct, and effective blood flow simulating the measurements made by dynamic contrast-enhanced imaging (e.g., DCE-CT) in each was calculated and used as inputs to the MPO₂ model to calculate the average pO₂ in a voxel. The standard (or reference) pO₂ was the average of all pO₂ levels at the microscopic scale as determined by the GPO₂ model. Therefore, the virtual grid allowed the investigation of correlations between MPO₂ and GPO₂ with respect to voxel size. In addition, the number of data points was increased by translating the voxel grid to different locations (note, if a portion of the voxel lay outside of the tissue, it was excluded from the analysis). In the tumor, six different voxel sizes were investigated: 50, 100, 150, 200, 250, and 300 μm . In brain, 50 and 100 μm voxel size was simulated owing to the limited brain volume.

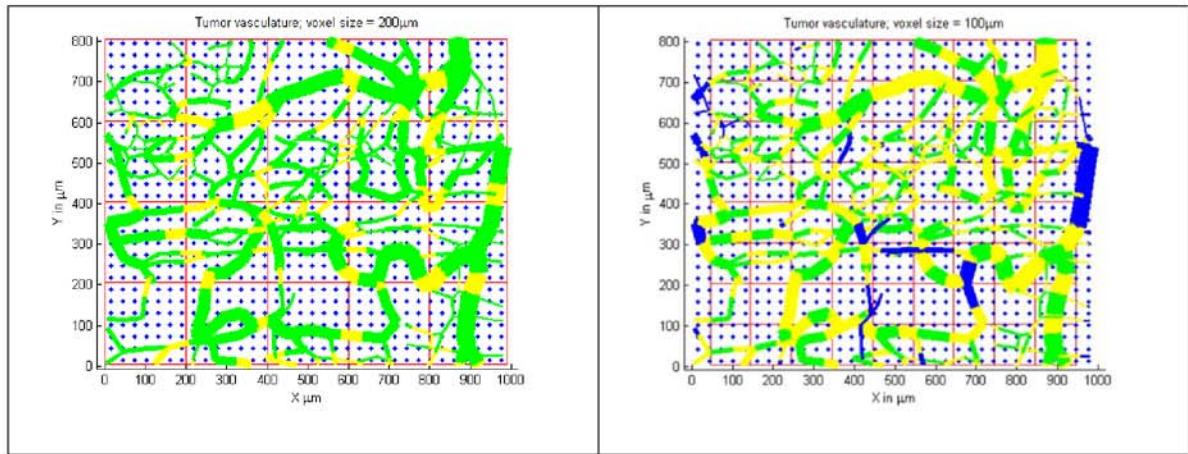


Figure 4.1.1.1: Schematic illustration of tumor microvasculature and lattice and voxel grid layout. Blue diamond represented the lattice points used to calculate pO_2 . Red grid represented the voxel grid with voxel size (200 and 100 μm). Entire vessel segments outside of the voxel grid were colored in blue; entire vessel segments dwelling in a voxel in green; the partial vessel segments which crossed at least two neighboring voxels in yellow. Since 200 μm voxel covered entire vasculature, no blue vessel should exist under layout.

4.1.2 The Average pO_2 of a Voxel Using GPO2 Model

Green's function algorithm first applied a set of equally-spaced, symmetric lattice points within the tissue (blue diamonds of figure 4.1.2.1.A). When implementing this algorithm to the brain and tumor tissue, the pO_2 was determined on this densely populated set of lattice points 15 μm apart, which was chosen to be sufficiently small so as to eliminate any systematic errors based on this parameter. The pO_2 , based on the GPO2 model, was the average of all the pO_2 values for those lattice points within a voxel (figure 4.1.2.1.B).

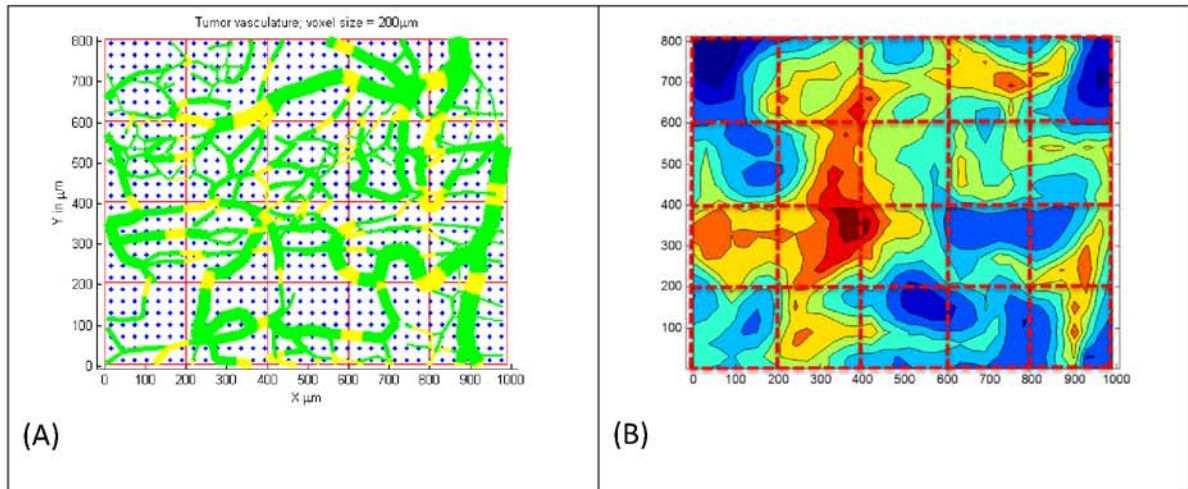


Figure 4.1.2.1.A-B: Demonstration of standard voxel GPO2 calculation. Figure B showed the tissue pO2 profile resulting from the tumor vasculature. The GPO2 of each voxel was the average of pO2 within the voxel.

4.1.3 The Fractional Vessel Volume in a Voxel

A stereological method was used to calculate the total vessel volume within a voxel based on the vessel segments (Figure 4.1.3.1). Briefly, a vessel segment is discretized into points uniformly along (r, θ, z) based on the orientation of the vessel's cylindrical coordinate system, where sampling along r and z was $1\mu\text{m}$ and angular sampling (θ) occurred every 5 degree. The fraction of the vessel volume within each voxel was determined by the fraction of discretized points. This method is accurate and accounts for the volumetric contribution from the vessel segments clipping the corner or edge of a voxel [185]. The equivalent radius of a single MPO2 vessel segment (r) is evaluated by cylindrical volume formula (vascular volume = $\pi r^2 L$), where the length of the vessel (L) is equal to the length of the voxel.

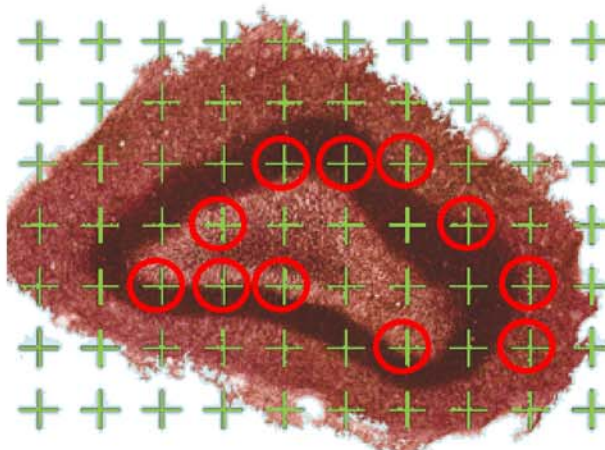


Figure 4.1.3.1: A Schematic illustration of stereology concept. An artificial regular grid (Cavalieri estimator) is superimposed onto a tissue section to estimate the area of interest (dark ring structure). A physical equivalent area representing a cross point is equal to the total area divided by the total number of crosses. Count the number of cross points hit the area of interest, marked by red circles in the figure. The area of interest is equal to the number of hits multiplying the physical unit area. This concept is also valid to estimate the volume of an irregular object.

4.1.4 The Blood Perfusion in a Voxel

Microvascular blood flow is assumed to be uniform in each vessel segment and follows mass conservation at every branch point. Blood flow into or out of a vessel were calculated perpendicular to the cross section surface. The magnitude of the blood flow along the x, y, and z directions from all crossing vessel segments was used to calculate the MPO2 vessel blood flow and a voxel's perfusion. This determination of the blood flow represents perfusion (blood flow divided by the volume of the voxel) as measured from dynamic contrast-enhanced imaging modalities, such as DCE-CT and DCE-MRI.

4.1.5 The SaO₂ and Initial pO₂ in a Voxel

A Krogh model requires the initial pO₂ as a determinant to calculate the pO₂ distribution around a cylindrical vessel. Most of Krogh type model simulation adapted a physiological pO₂ as the initial pO₂ value and used it as a constant in modeling study. Often the choice of initial pO₂ varies among the publications. In this study, the intravessel pO₂ by Green's function to be used to determine the SaO₂ as measured from in vivo imaging, which in turns, was used to determine the initial pO₂. The latter was used as one of the input arguments for MPO2 tissue oxygenation algorithm. The oxygen saturation level within a vessel segment was derived from intravessel pO₂ by inverting Hill's equation. The volume-weighted average SaO₂ of the voxel was calculated with the following formula:

$$SaO_2(voxel) = \frac{\sum_i S_i \cdot V_i}{\sum_i V_i}$$

S_i is the SaO₂ of the i^{th} vessel segment; V_i is the volume of the blood vessel inside a voxel contributed from the i^{th} vessel segment. The pO₂ within a voxel was calculated using the average SaO₂ and inverting Hill's equation; the initial pO₂ at the voxel entrance for MPO2 simulation was then set to be double of the voxel pO₂. The rationale is as follows:

$$pO_2(z) = pO_2(z=0) - \frac{M H}{(1+m) F} \left[\left(\frac{r_T}{r_c} \right)^2 - 1 \right] z ,$$

Given that this equation is linear along the z-axis (length of blood vessel), the relationship between the average pO₂ and input pO₂ is

$$pO_2(z) = pO_2(z=0) - \frac{M \cdot H}{(1+m)F} \left[\left(\frac{r_T}{r_c} \right)^2 - 1 \right] z,$$

which can be rewritten as

$$\langle pO_2 \rangle = \frac{pO_2(0) + pO_2(L)}{2}$$

or

$$\langle pO_2 \rangle = pO_2(0) + pO_2(L) = 2 \cdot pO_2(0) + \frac{M \cdot H}{(1+m)F} G_2(r_c, r_T) \cdot L$$

The second term on the right is a constant; therefore,

$$pO_2(0) = \frac{1}{2} \cdot \left(\langle pO_2 \rangle - \frac{M \cdot H}{(1+m)F} G_2(r_c, r_T) \cdot L \right)$$

However, an exception occurs if pO₂ is less than zero along the length of the blood vessel. In these situation, negative values are set to zero and a recalculation of pO₂(0) is determined.

4.1.6 Linear Regression to Evaluate the Correlation Between the GPO2 and MPO2

Models of pO_2

A linear least squared method was used to fit the pO_2 value as determined by the MPO2 and GPO2 models. A Pearson correlation coefficient was calculated to indicate the degree of linearity between the paired pO_2 values and the r-squared to determine the goodness-of-fit. To increase the number of data points in the regression analysis, in particular for the larger voxel sizes, and to better simulate tumor vascular physiology heterogeneity, the maximum oxygen consumption rates was varied randomly (in +/-50% range) relative to the initial value and the total tumor blood flow was chosen randomly (in +/- 25%) relative to the initial value. In addition, the voxel grid was moved to different regions within the tumor to simulate various vessel configurations in the voxels.

4.1.7 Sensitivity of MPO2 to Changes in the Vascular Inputs

MPO2 model considers several nonlinear relationships between two variables, including Hill's equation and Michaelis-Menton kinetics, when numerically calculating a voxel's pO_2 . Although the local pO_2 is the synergistic consequence of vascular physiology and microenvironment, some determinants will be more dominant than others in regulating the local pO_2 value. To compare the pO_2 response among the key inputs of MPO2 (blood perfusion, vessel radius, hemoglobin concentration, SaO_2 , and oxygen consumption rate), a single variable was adjusted to +/- 10 and 20 percent relative to its reference value while all other variables were held constant. The reference value of the blood perfusion, the hemoglobin concentration, and the SaO_2 were selected from in house

preliminary tumor DCE-CT and PCT-S measurements and the oxygen metabolic rate was chosen from publications. The percentage change in pO_2 was calculated and plotted to assess the sensitivity and relationship of each variable to the pO_2 .

4.1.8 MPO2 Uncertainty Analysis

All physical quantities are subject to uncertainties in their measurements. The MPO2 model simulated these uncertainties consistent with measurements acquired from *in vivo* functional imaging modalities. In the analysis, several 150 μm voxels were used to test the precision and error in the pO_2 from 5 to 25 mmHg range. A randomly generated Gaussian error function was used to simulate the uncertainty in the fractional vessel volume and blood perfusion in each voxel, where the full width at half maximum (FWHM) of the Gaussian error function was 20% of the voxel's nominal value. Ten simulated blood perfusion measurements and the fraction of vessel volume measurements were performed, and the corresponding pO_2 based on MPO2 model calculated. From these ten simulations, the average and standard deviation were used to determine the accuracy and precision of MPO2.

4.2 Results of Vasculature Characterization

4.2.1 Brain and Tumor Microvasculature Characterization

The microvasculature structure and associated physiology are directly related to the local delivery of oxygen within a tissue or organ. To test the feasibility of our *in vivo* 3-D pO_2 assay, the pO_2 distributions (or images) using Green's function method (GPO2)

(reference) and the proposed multivariate *fusion* model (MPO2) for a rat brain (normal control) and a tumor were compared, and the influence of the spatial resolution and noise of the imaging system on the systematic and statistic uncertainties in pO₂ investigated.

For these studies, the reconstructed microvascular networks of the brain (150 μm x 160 μm x 140 μm) and tumor (990 μm x 810 μm x 150 μm) as shown in Figure 4.2.1.1 A-B, were modeled based on acquired data from a scanning confocal microscope [186]. In Figure 4.2.1.2, the blood flow and diameter histogram of the brain and the tumor vessel network is displayed. The minimum diameter of both the brain and the tumor vasculature was close to 5 μm , but the range of blood flows from the minimum vessel to the largest showed a difference of a factor of 78 (0.5 nL/min against 0.0064 nL/min). 26 percent of the tumor vessel segments flow rates was less than 0.5 nL/min. In addition, those vessel segments with low flow rates appeared in capillaries (diameter \sim 5 μm) and arterioles (diameter $>$ 15 μm). For normal microvessel networks, a linear correlation exists between the vessel diameter and flow which is lost due to the abnormal vasculature in the tumor (Figure 4.2.1.3).

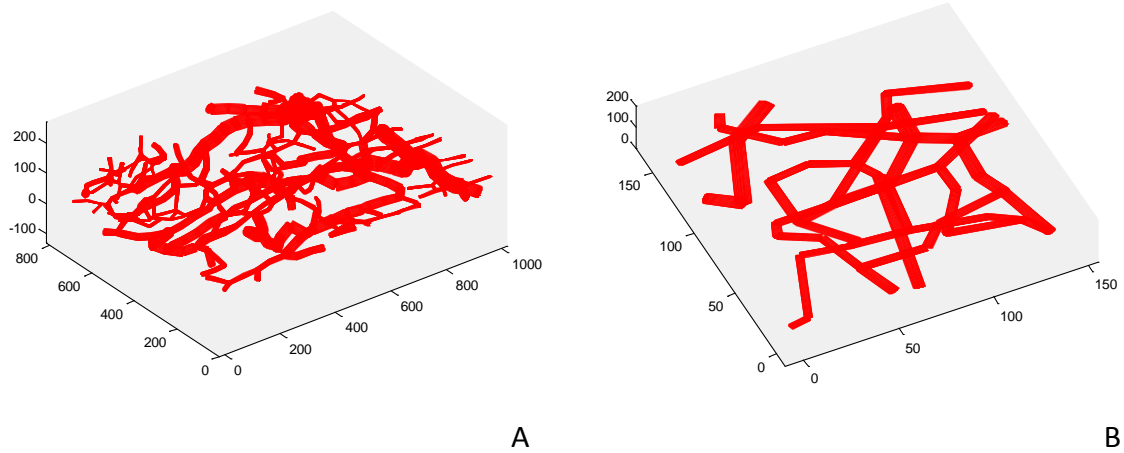


Figure 4.2.1.1.(A/B): Reconstructed microvessel network of tumor and brain by confocal scanning microscope at sub- μm resolution. The unit is μm in both microvasculatures.

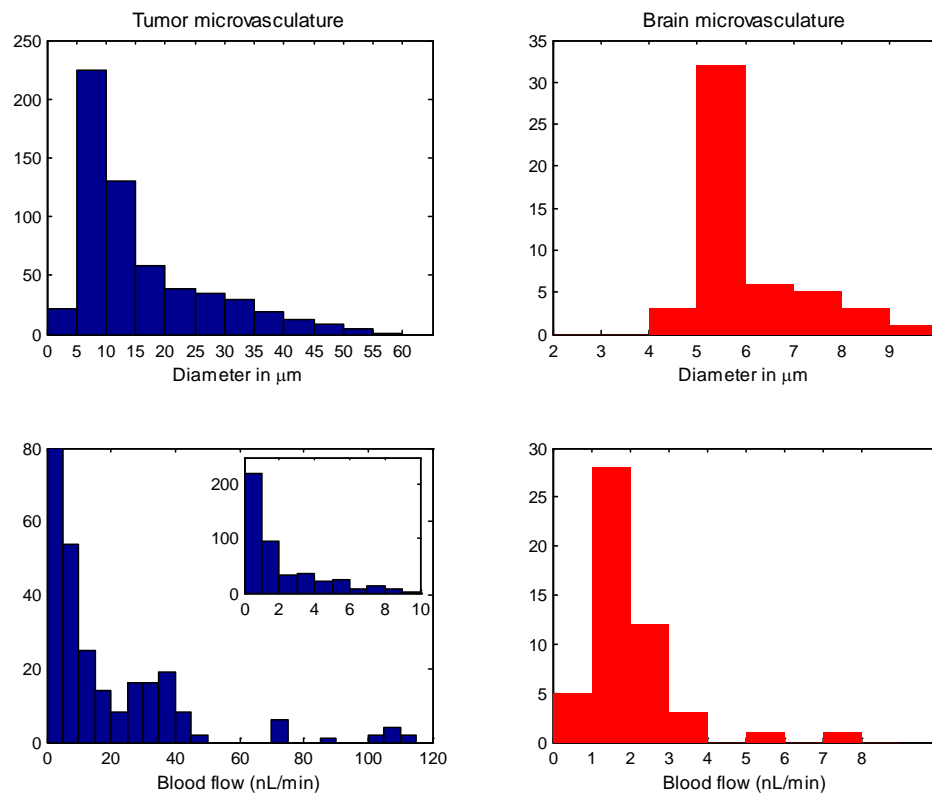


Figure 4.2.1.2: Tumor and brain microvasculature diameter and flow histogram. Tumor histograms are colored in blue; brain histograms in red. For tumor blood flow, the number of vessel segments with flow rate < 5 nL/min is close to 400; the inset displays the detail distribution of blood flow from 1 to 10 nL/min.

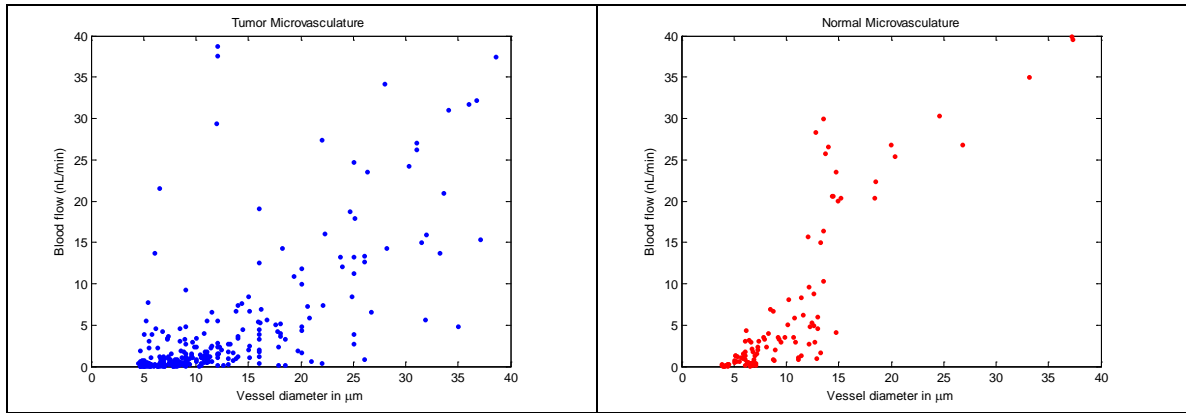


Figure 4.2.1.3: Blood flow correlation of tumor microvasculature on left and of brain vasculature on right.

4.2.2 The 3-D pO₂ Map as Determined by Green's Function Algorithm

The 3D pO₂ distributions in the tumor and brain tissue based on GPO₂ are displayed in

Figure 4.2.2.1. Note the spatial resolution of this data is 15 μ m.

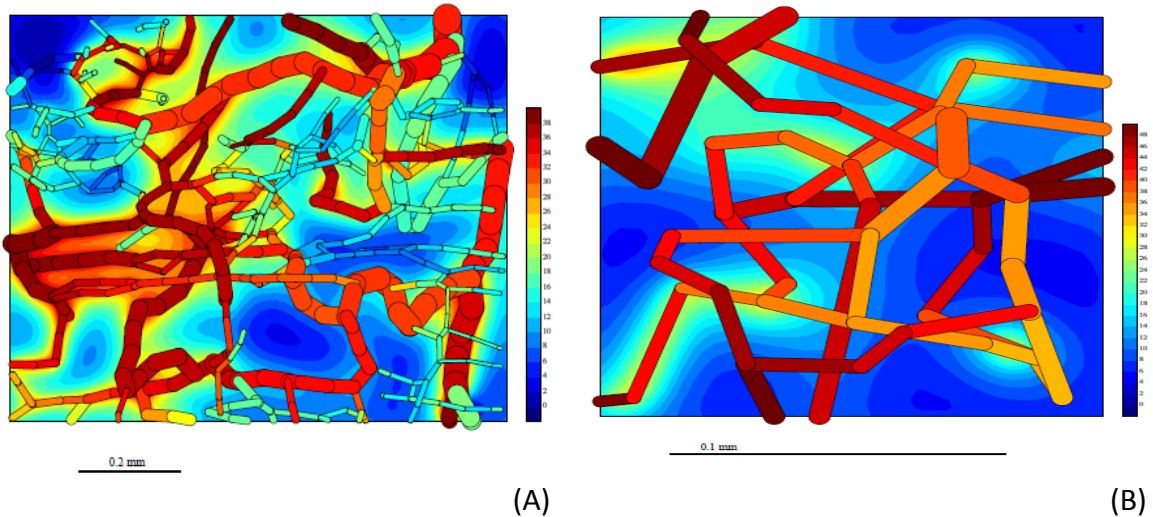
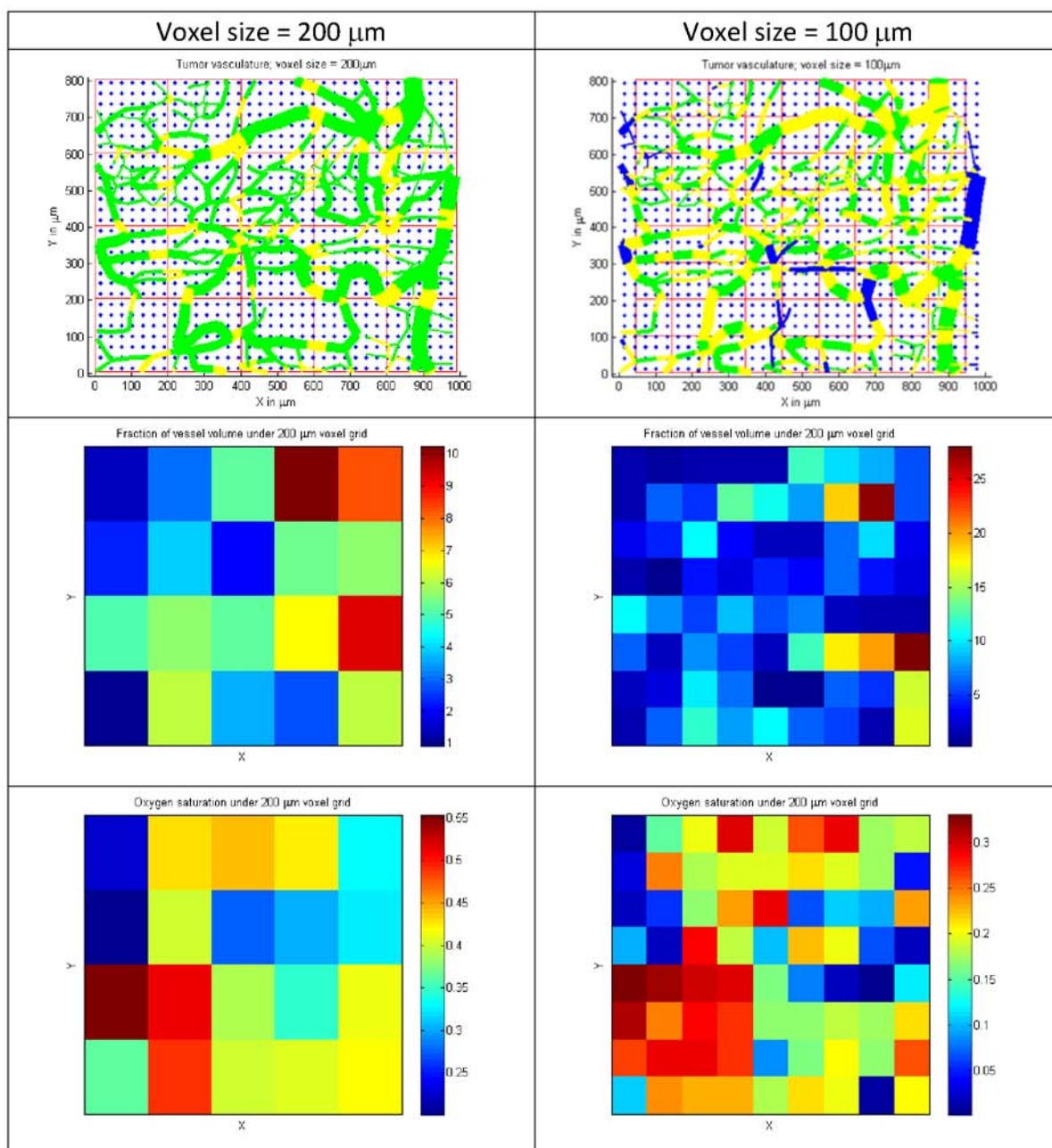


Figure 4.2.2.1: (A) Partial oxygen pressure distribution (pO₂) in tumor. The entire tumor region is 990 μ m x 810 μ m x 150 μ m in 2D view. (B) pO₂ in brain. The brain region is 150 μ m x 160 μ m x 140 μ m. The colorbars on the right indicate the pO₂ value. The scale bar in tumor represents 0.2mm; the scale bar in brain represents 0.1mm.

4.3 Comparing the Results of MPO2 Model to GPO2 Standard

In section 4.1.1, the concept of a virtual grid was introduced to simulate the spatial resolution of a parametric map obtained from a functional imaging (e.g., DCE-CT). First, the average pO_2 in a voxel based on the GPO2 model was calculated. Next, the vascular physiology and hemodynamics in each voxel were calculated and inserted into equations (18)-(19) to derive the corresponding pO_2 based on the MPO2 model. In Figure 4.3.1, an example of these maps (or images) of the vascular physiology, the MPO2, and the GPO2 values for pO_2 are displayed for 100 and 200 μm voxel sizes.



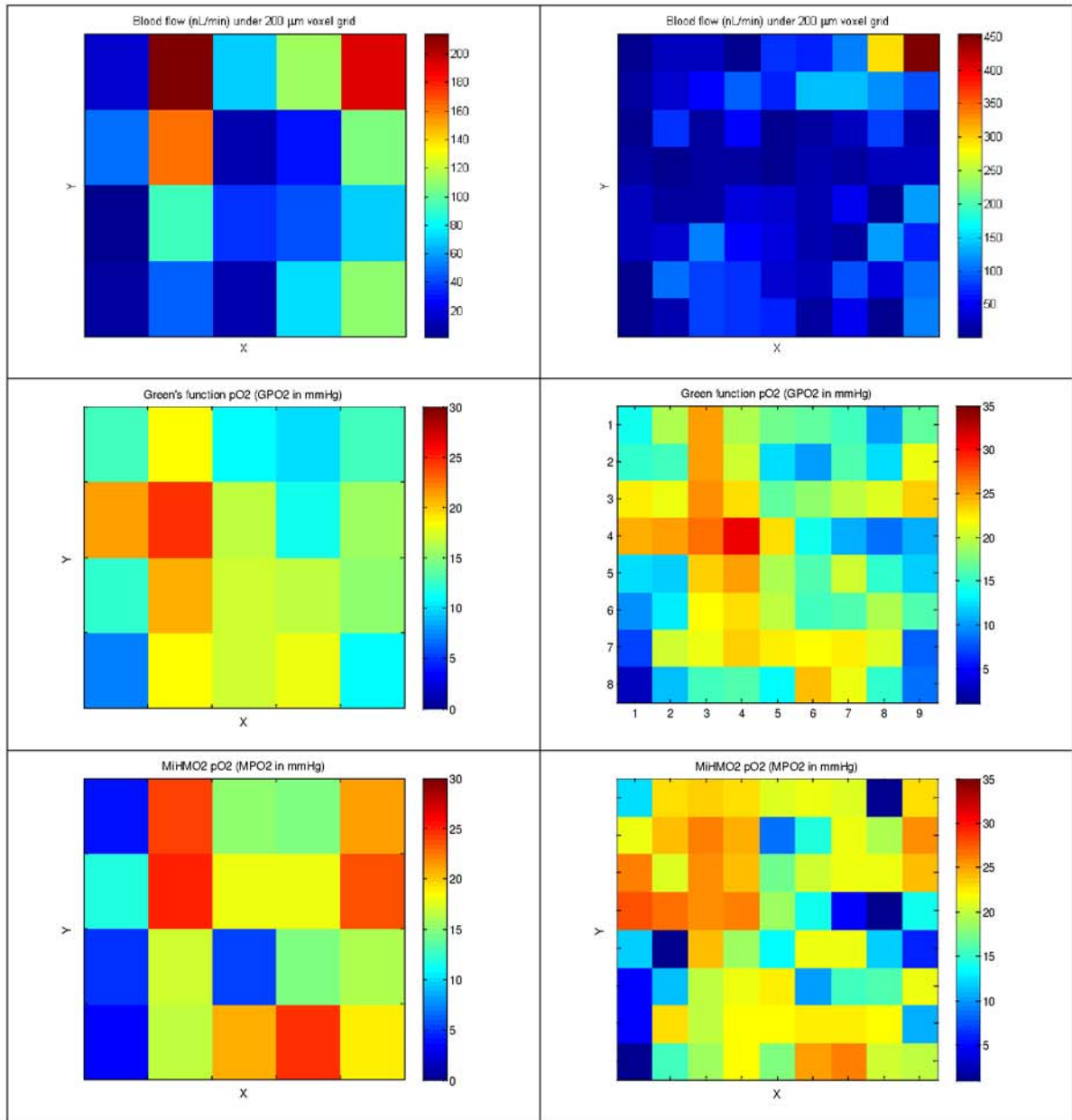


Figure 4.2.2.1: Heat map of SaO₂, blood flow, fraction of vessel volume, GPO₂, and MPO₂ under voxel grid = 200 and 100 μm . Blue diamonds represent the location of lattice points in ROI. Red grid represents the voxel grid with voxel size (200 and 100 μm). Entire vessel segments outside of the voxel grid are colored in blue; entire vessel segments dwelling in a voxel in green; the partial vessel segments which cross at least two neighboring voxels in yellow. The heat map colorbar indicates the value of three key inputs. The unit of fraction of vessel volume is in percentage; the value of SaO₂ goes from 0 (no oxygen binding) to 1 (saturated oxygen binding); the unit of blood flow is in nL/min.

4.3.1 Characterization of MPO₂ Distribution in a Single Voxel

MPO₂ is a multivariate, single-vessel, modified Krogh model. Knowledge of the typical pO₂ profile obtained from this model can help assist and further explore the oxygen transport mechanism in tissue, such as the causes to the accuracy and precision of this technique. The typical 2D view of the pO₂(r,z) distribution within a voxel from a single vessel placed at its center is shown in Figure 4.3.1.1, where the blood flow was from left to right. The cellular density, as determined from imaging ($f_{\text{cell}}=1-f_{\text{BV}}-f_{\text{is}}$), in the tissue region was assumed to be uniform. The partial oxygen pressure decreased monotonically in radial and longitudinal orientation (Figure 4.3.1.1). The anoxic region, where tissue pO₂ was equal to zero, could exist at the remote corners, where oxygen supply from vessel was weak.

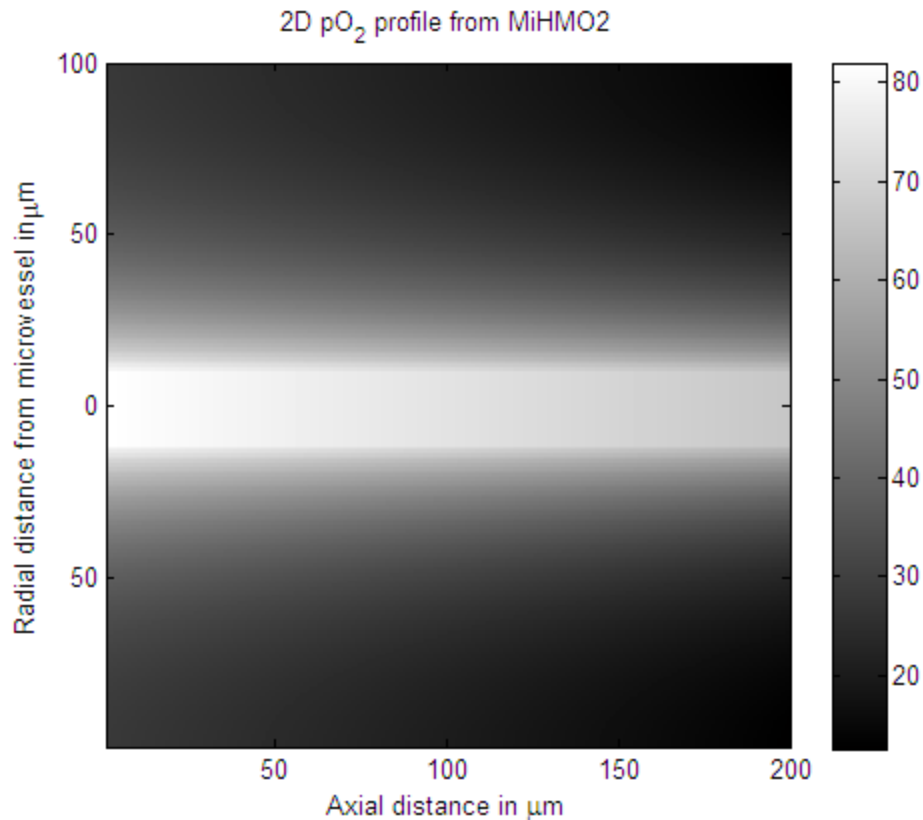


Figure 4.3.1.1: Two-dimensional pO₂ profile demonstration by single vessel MPO2 model in a 200 μm voxel. A single 20- μm diameter vessel is placed at the center of a $(200 \mu\text{m})^3$ voxel. The origin of a cylindrical coordinate is located at the entrance of blood vessel with z-axis oriented toward to blood flow direction. The cylindrical vessel configuration leads to pO₂ distribution symmetry in radial and azimuthal direction. Anoxic region, pO₂ = 0 mmHg, could occur at the remote corners in MPO2 modeling. Any negative pO₂ from MPO2 calculation is replaced by zero mmHg. Average tissue pO₂ by MPO2 algorithm excludes the pO₂ contribution from the vessel lumen. The unit of gray color bar is mmHg.

4.3.2 MPO2 Sensitivity to Vascular Inputs

MPO2 integrates or fuses variables based on biophysical models where the measured inputs are obtained from in vivo imaging. In this section, the sensitivity of pO₂ on these variables was simulated. Each variable in turn was modified by -20, -10, 0, +10, and +20

percent relative to baseline values while holding all other parameters constant, and the change in the pO_2 value measured.

Displayed in Figure 4.3.2.1 is the percent error in the pO_2 as a function of the blood vessel radius, perfusion, metabolic rate, SaO_2 and hemoglobin concentration. Based on these results, each factor affected the pO_2 values but in different ways. For example, changes in the metabolic rate showed the highest impact to tissue oxygenation in -20% group, while changes in the blood perfusion was dominant in 20% group. The oxygen consumption rate had the largest impact on tissue pO_2 , where the average absolute percent change in pO_2 percentage was 16.0%. The hemoglobin status as determined by SaO_2 and $CtHb$ resulted in a 12.6% and 15.0% variation in pO_2 , respectively, and the physiological parameters such as the vessel diameter and blood perfusion changed the pO_2 by 9.7% and 15.2%, respectively.

Figure 4.3.2.1: Partial oxygen pressure sensitivity of five MPO2 input parameters. The pO2 response are organized into five groups (-20%, -10%, reference, 10%, and 20%). All responses are in percentage and normalized with respect to the referenced determinant; accordingly the response of the reference group is zero.

4.3.3 Linear Regression Results of MPO2 versus GPO2

A key objective of specific aim one is to validate the accuracy of the MPO2 at various voxel sizes, at various scanner spatial resolutions. In figures 4.3.1.1 and 4.3.1.2, scatter plots of the pO2 within each voxel for as determined by MPO2 and GPO2 were fit to a line (linear regression analysis) for normal brain tissue and tumor as a function of voxel size. For the rat brain tissue, both 50 and 100 μm voxel sizes demonstrated a high level of correlation with a slope of 1.0, an offset of less than 0.85 mmHg, and an Rsq of 0.86 and 0.91, respectively, and p-value less than 0.01. Similarly, the correlation between MPO2 and GPO2 for the tumor was very good for voxel sizes of 100, 150, and 200 μm , where the slopes were 1.0, offsets within ± 1 mmHg, and Rsq values of 0.80, 0.83, and

0.75, respectively with p-values less than 0.01. However, for small (50 μm) and large (250 and 300 μm) voxel sizes, the quality of the fits decreased. The scatter plot for a 50 μm voxel size had two outlier groups, one where the MPO2 overestimated the GPO2 values and another that underestimated these values (the short-dash and long-dash oval curves, respectively). Even though the slope and offsets were reasonable, the variance in the data was significantly larger (e.g., Rsq of 0.71) due to this systematic affect. Unlike the 50 μm voxel data set, a decrease in the slope and increase in the offset was observed, with an increase in the variance (Rsq).

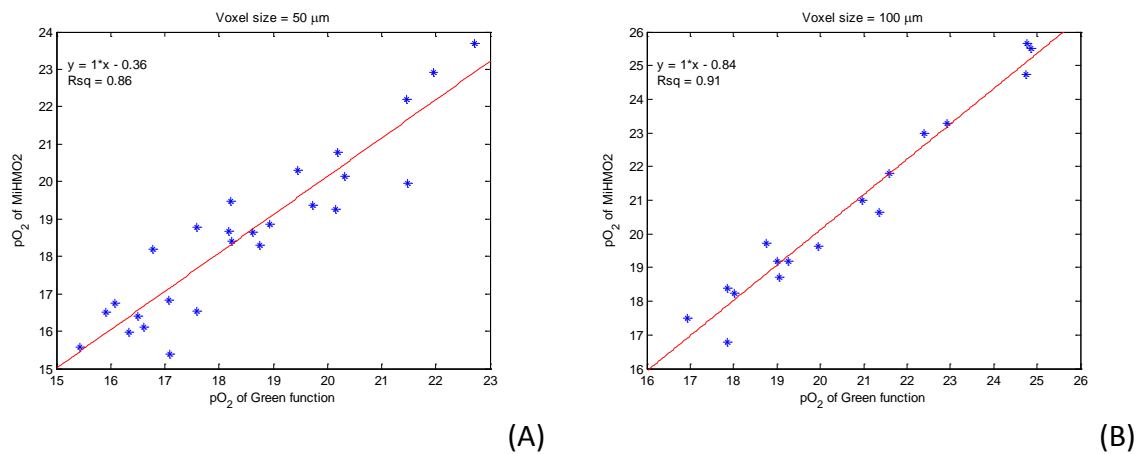


Figure 4.3.3.1: Brain pO2 scattering plot of MPO2 and GPO2. Brain pO2 correlation plots at voxel sizes 50 and 100 μm are shown in the panel A and B. The abscissa consists of the average Green's function pO2 of the voxels; the ordinate consists of the MPO2 from the same voxels. Red lines are the linear regression fitting; the result of linear regression fitting and Rsq are displayed on top-left corner.

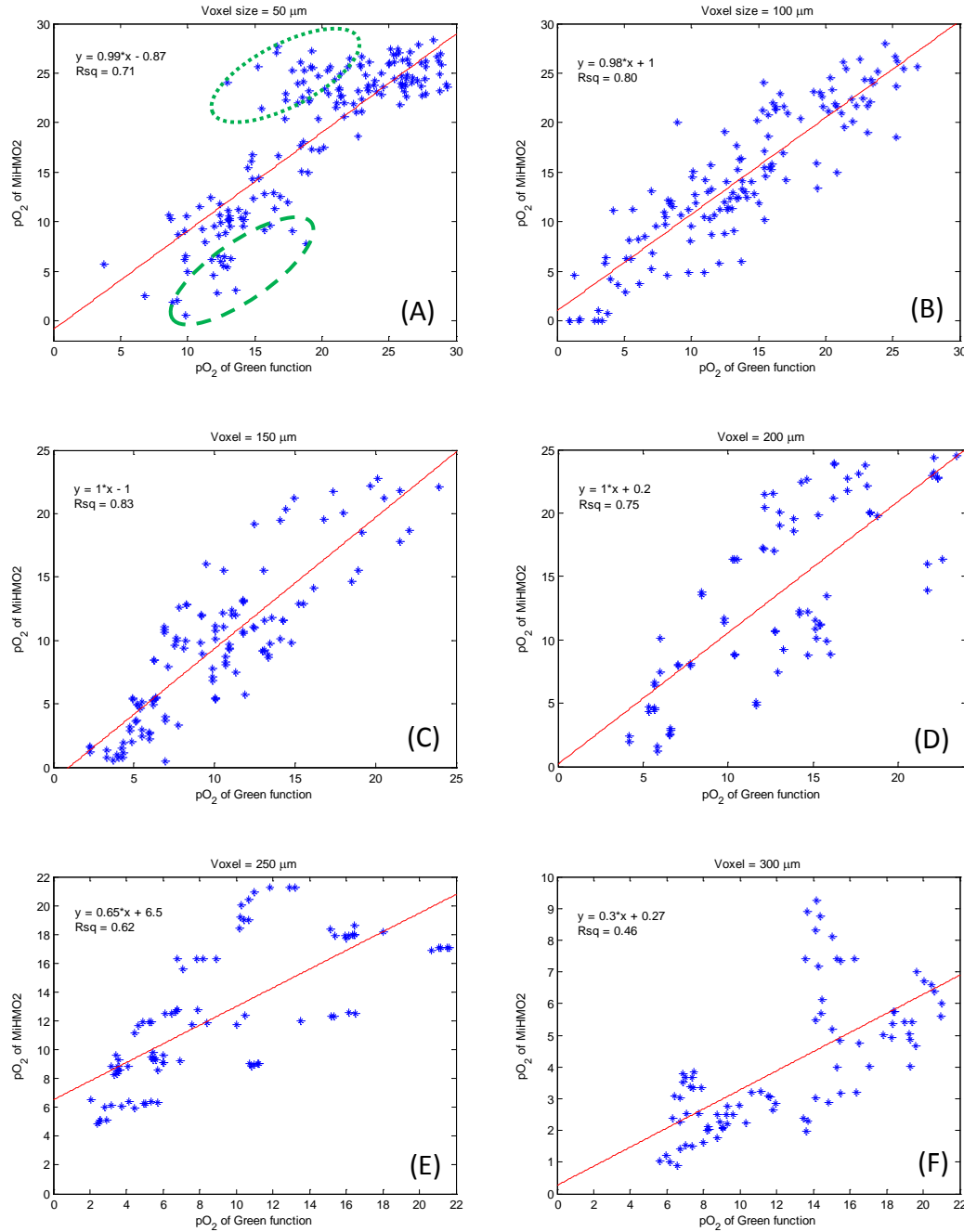


Figure 4.3.3.2(A/F): Tumor pO_2 correlation of MPO2 and GPO2 as function of the voxel size. Six pO_2 scattering plots of pO_2 (mmHg) at voxel sizes (50, 100, 150, 200, 250, and 300 μm) are displayed in the panel (A-F). At 50 μm voxel size (panel A), the underestimated MPO2 outliers are enclosed in a long dash oval; the overestimated MPO2 grouped in short dash oval.

4.3.4 The Nearest Neighbor Algorithm to Correct for 50- μ m Voxel Outliers

The underlying causes of the outliers were investigated. In figures 4.3.4.1.A-B, the location of the overestimated ($MPO_2 \gg GPO_2$) and the underestimated outliers ($MPO_2 \ll GPO_2$) were identified. The overestimated outlier voxels were either located near (not in voxel) a major arteriole or the fraction of the vessel volume was more than 0.8. On the other hand, the underestimated voxels had a low fractional vessel volume and the vessel density of the surrounding voxels was also very low. This observation reflected the abnormal tumor vasculature heterogeneity. To improve the regression analysis, a nearest neighbor algorithm was adopted to correct outliers by considering the boundary conditions imposed by these voxels. The nearest neighbor algorithm replaced the pO_2 value in MPO_2 model by the average pO_2 from the nearest surrounding neighbors. After applying this algorithm, the variance in the 50- μ m voxel plots greatly improved (Figure 4.3.4.2-A) (see Appendix A for detailed explanation on algorithm implementation), where the two outlier populations disappeared and the Rsq improved from 0.71 to 0.81 (figure 4.3.4.2-B).

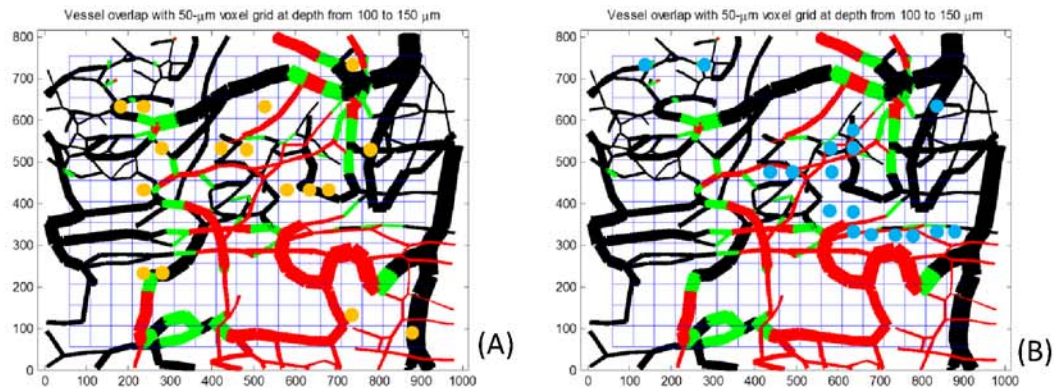


Figure 4.3.4.1.A-B: Outlier voxel location in tumor microvasculature. The overestimated outliers, of which MPO2 is exceedingly greater than Green's function pO2, are marked with yellow solid circles in panel A; the underestimated outliers, of which MPO2 is exceedingly lower than Green's function pO2, are labeled with blue solid circles in panel B.

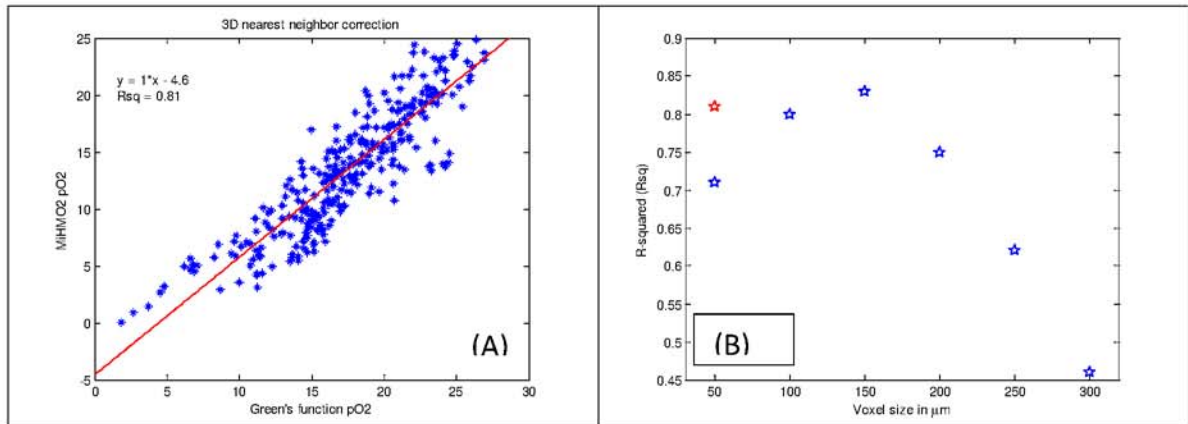


Figure 4.3.4.2.A-B: The correlation scattering plot after nearest neighbor correction on 50-μm grid on tumor vasculature was shown in figure (A); two outlier population in figure 5.4.3.2-A was disappeared. The goodness of fit (r-square) as function of voxel size is demonstrated in figure (B). The blue stars represented the rsq values from figure .4.3.3.2; the red star highlighted the rsq improvement by nearest neighbor algorithm.

4.3.5 MPO2 Uncertainty Analysis

Any physical measurement contains two essential components: (1) a value giving the best estimate possible for the quantity measured, and (2) the degree of uncertainty associated with this value. Since the MPO2 model is a function of measurements acquired from imaging, simulations were performed to understand the influence of error propagation of these measurements to the calculated pO2 value. These simulation results are displayed in figure 4.3.5.1 and suggest that MPO2 showed that the average coefficient of variation (CV) was 7% after adding in noise (20 percent) to the fractional vascular volume and 3.4% for blood perfusion.

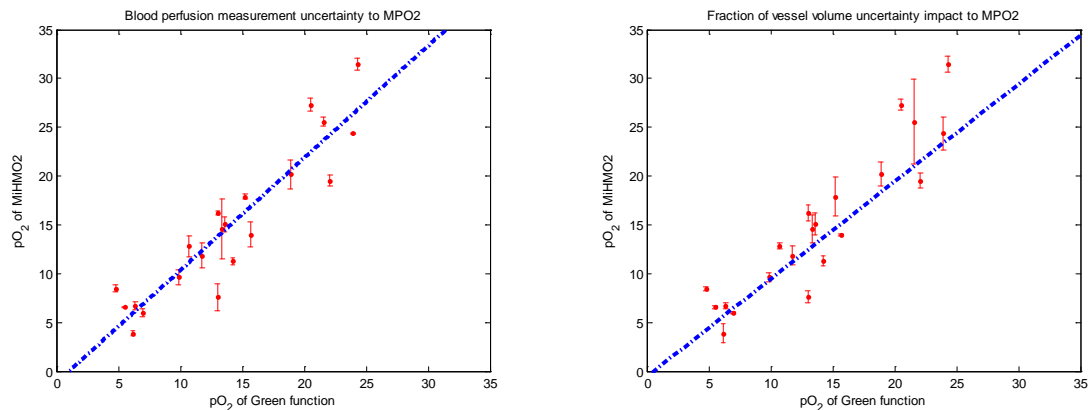


Figure 4.3.5.1: Response of MPO2 to the perfusion measurement uncertainty (on left) and the f-plasma measurement uncertainty (on right). Horizontal axis represents the Green's function pO₂ of the voxel and vertical axis the average pO₂ from 10 simulated MPO2 with blood perfusion and fraction of vessel volume uncertainty following Gaussian error function. The blue dot-dash line is the pO₂ regression line of 150 μm voxel (see figure 4.3.3.2-C).

CHAPTER 5. COMPARING IN VIVO PO₂ MEASUREMENTS BASED ON THE MPO₂ MODEL AND OXYLITE OXYGEN SENSOR

In Chapter 4 (specific aim 1), a correlation was demonstrated between the local pO₂ levels calculated using the modified Krogh model, MPO₂ model, and Green's function algorithm, GPO₂ model, which was based on the detailed microvascular structure and functionality of tumor and brain tissue. In this chapter, an OxyLite oxygen sensor is used as a *Gold Standard* to measure the local pO₂ in a tumor. These measurements are compared to the pO₂ as determined from the MPO₂ model, where the input parameters to this model (the physiology of the tumor's hemodynamics: perfusion, fractional plasma volume, fractional interstitial volume, oxygen saturation, hemoglobin concentration) are measured using DCE-CT and PCT-S. Thus, a direct comparison between the theoretical and measured pO₂ values, (MPO₂) and OxyLite probe respectively, is possible.

5.1 Introduction

The polarographic needle oxygen sensor, or Eppendorf probe, is an accurate method to measure *in vivo* tissue pO₂ (considered the Gold Standard). It is composed of two electrodes, where the current generated by the electrochemical reaction at cathode ($\text{O}_2 + 2\text{H}_2\text{O} + 4\text{e}^- \rightarrow 4\text{OH}^-$) is proportional to the oxygen concentration [187]. Due to cost, it is not widely used within clinical and basic research facilities. However, the OxyLite oxygen sensor (Series-E, Oxford Optronix, Oxford, UK) provides an easy-to-use and low cost alternative. It employs phosphorous quenching technique to quantify the local oxygen concentration. Oxygen, as a triplet molecule, has the ability to efficiently decrease the fluorescence and phosphorescence of certain luminophores, which is called "collisional quenching"[188]. An LED emits a pulse of blue light (475 nm) exciting a chemical complex at the tip of the probe, which subsequently emits photons at 600 nm. When an oxygen molecule collides with the excited complex, the excess energy will be transferred to the oxygen molecule, thus quenching the fluorescence signal. The degree of quenching is directly related to the oxygen concentration or partial pressure level of the oxygen-containing media [188, 189].

The OxyLite sensor has a number of advantages over the Eppendorf probe: (1) low cost and flexible; (2) not based upon oxygen consumption [190]; (3) long-term pO₂ measurement stability; (4) no electric hazard during measurement. Several studies have shown close agreement between the pO₂ measurements using the OxyLite probe and

the polarographic needle oxygen sensor [86, 191], and thus used as the *Gold Standard* technique to validate MPO2. First, OxyLite calibration data was obtained where the dissociation curve -- SaO_2 versus pO_2 -- was analyzed for ex vivo blood samples. Second, the dissociation curves for breast tumors with differing angiogenic phenotypes were investigated, where photoacoustic imaging was used to measure SaO_2 levels. Finally, the local pO_2 levels calculated using MPO2 model and measured hemodynamic images (DCE-CT and PCT-S) was compared to OxyLite measurements.

5.2 Material and Method

5.2.1 Calibration Phantom

A closed blood circulation system was constructed to validate or calibrate the OxyLite oxygen sensor by measuring the oxygen saturation (SaO_2) and partial oxygen pressure (pO_2) in recently expired blood. This *blood* phantom consisted of a tonometer, a capillary pump, a hot plate (maintain temperature), a set of flow gauges and a mixing chamber (figure 5.2.1.1), and by controlling the flow rates of nitrogen and oxygen, the amount of oxygen exposed to the blood within the tonometer was varied to obtain a range of SaO_2 and pO_2 levels. The OxyLite probe (series E, temperature integrated) was placed within the tonometer to monitor blood pO_2 , and after reaching a steady-state level (2-3 minutes), a sample was drawn and the SaO_2 measured using a co-oximeter (682 co-oximeter, Instrumentation Lab). The plot of the SaO_2 as a function of pO_2 was fit to Hill's equation,

$$SaO_2 = (pO_2)^n / (P_{50} + (pO_2)^n),$$

to determine Hill's coefficient, n , and the pO_2 at the fifty percent SaO_2 level, P_{50} .

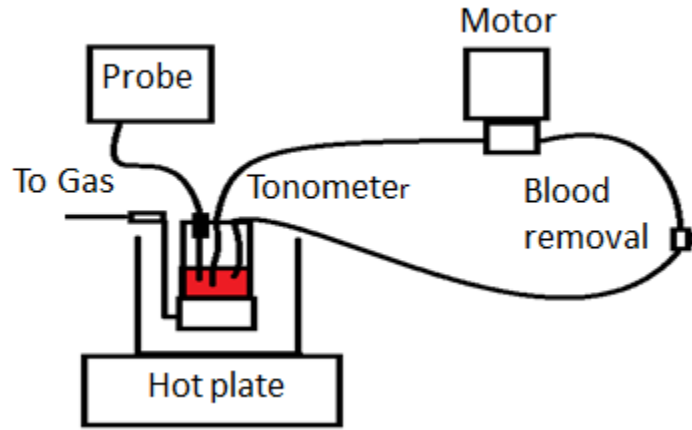


Figure 5.2.1.1: Experimental setup for blood phantom SaO_2 and pO_2 quantification with various mixtures of air and Nitrogen.

5.2.2 Animal Models

Three 6-8 week old female athymic (nu/nu) mice (Harlan Sprague-Dawley, Indianapolis, IN) were injected with $1-5 \times 10^6$ MCF-7, 1×10^6 MCF-7^{VEGF} (stably transfected with the VEGF165 gene) or MDA-MB-231 breast cancer cells in 0.1 mL of Hanks' buffered saline into the mammary fat pads. For mice implanted with MCF-7 cancer cells, an estradiol pellet (0.72mg, 60 day formulation) was implanted using a sterile 14-gauge trocar 24 hours prior to tumor implantation in order to provide a supplemental release of estrogen. Tumors were allowed to grow to an average diameter of 8-12mm prior to *in vivo* imaging and Oxylite probe measurements. All animal preparation and procedures

for this study were reviewed and approved by the Indiana University Institutional Animal Care and Use Committee.

5.2.3 Imaging Protocols

Prior to Oxylite probe measurements, each mouse was imaged using dynamic contrast-enhanced CT (DCE-CT) and photoacoustic CT spectroscopy (PCT-S) to determine vascular physiology (perfusion, F ; permeability surface-area product, PS ; fractional plasma volume, fp ; and fractional interstitial volume, fis) and hemoglobin status (oxygen saturation, SaO_2 ; hemoglobin concentration, $CtHb$), respectively. While under anesthesia (0.1 mg/kg (i.m.) acepromazine and 0.1 mg/kg (i.m.) torbugesic or 1-2% isofluorane), each mouse was positioned within the photoacoustic scanner (SAS; OptoSonics, Inc or Nexus128; Endra, Inc) so its tumor was at or near isocenter, and scans were obtained at 10 or more wavelengths throughout the near infrared spectral range (690-940 nm). Each set of acquired data was reconstructed for each wavelength ($0.1 \times 0.1 \times 0.1 \text{ mm}^3$ voxel size) implementing a 3-D filtered backprojection algorithm and co-registered across wavelengths (AFNI) to correct for small shifts or movement between scans. Corrections to the image intensities were performed to account for variations in the photon fluence emitted by the laser/OPO source as a function of the wavelength, the beam profile at the surface of the tumor, and the photon attenuation within water and tumor. The corrected spectral information was fit to a linear combination of the oxy- and deoxy-hemoglobin absorption spectra implementing a nonlinear multivariate fitting routine based on Levenberg-Marquardt least squares

method. The weights assigned to each point in these fits were set to the measured errors as determined by the residuals within the blood phantom (eight percent of signal intensity). The results of the fit provided an estimate of the CtHb and SaO₂ for each voxel comprising the tumor. The entire process, including visualization, fitting algorithms and analysis, was performed using an IDL code developed in-house. An example of a SaO₂ parametric map is shown in figure 5.2.3.1.

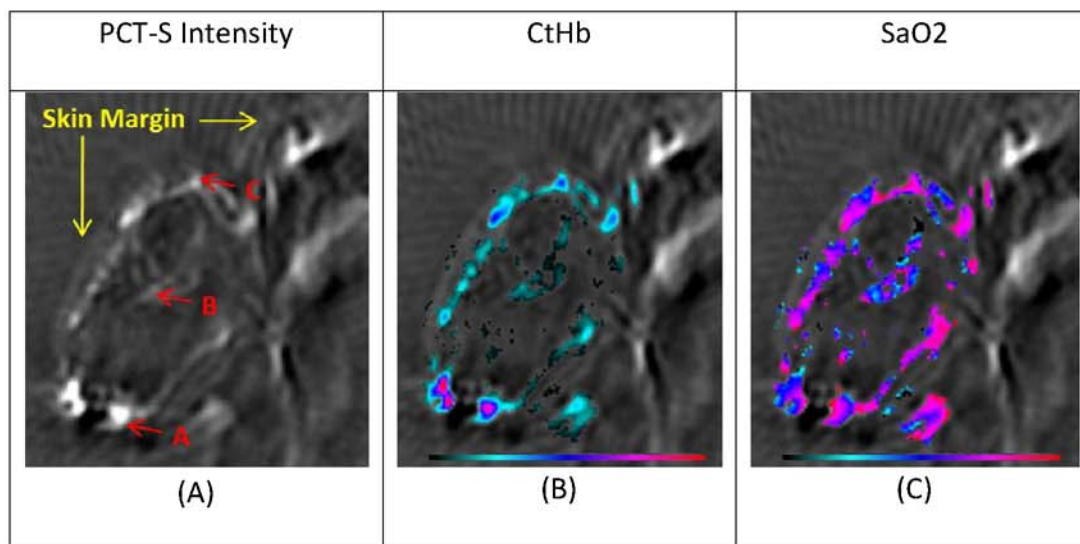


Figure 5.2.3.1: An example of CtHb and SaO₂ parametric map using photoacoustic spectroscopy (PCT-S). Figure A showed the intensity of PCT-S, three locations (A, B, C) were marked on the tumor; figure B showed the CtHb concentration in tumor; figure C showed the corresponding SaO₂ distribution in tumor. The CtHb and SaO₂ at location A, B, C are (41.1 μ M, 0.913), (11.6 μ M, 0.412), (31.9 μ M, 0.78).

Next, each mouse was positioned within a CT scanner (Brilliance, Phillips) so the heart and tumor are within the field-of-view (40×0.625mm collimation). CT scans were acquired (80kVp; 80mAs) prior to, during, and after an i.v. injection of a radio-opaque contrast agent (Isovue-370; Bracco Diagnostic). CT images were reconstructed with a

0.293 x 0.293 x 0.625 mm³ voxel size in the transaxial and slice planes, respectively. The dynamic contrast enhanced curves within each voxel was fit to a two-compartmental model to obtain physiological maps of perfusion, permeability-surface area product (PS), fractional plasma volume (F_p), and fractional interstitial volume (F_{is}). Further details of the data analysis can be found in a publication by Cao M *et al* [127]. An example perfusion map the MCF7 tumor is displayed in figure 5.2.3.2.

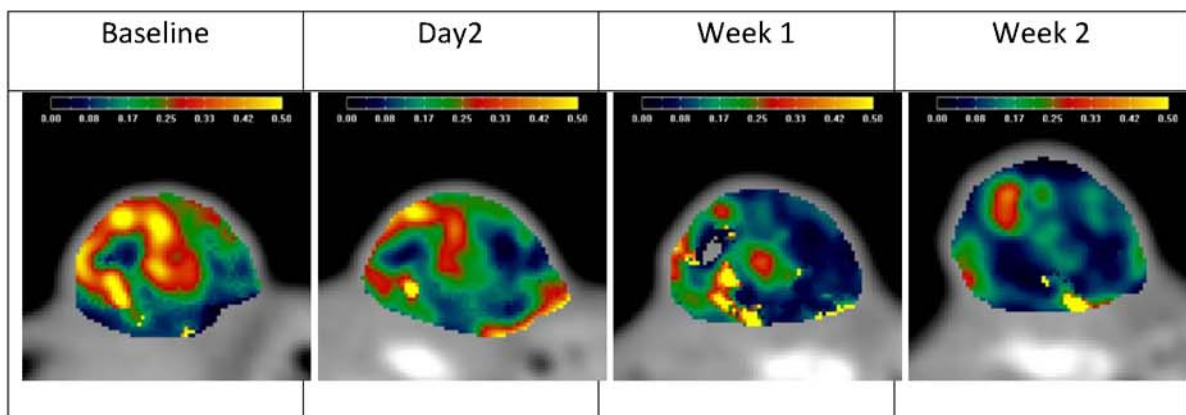


Figure 5.2.3.2: 3D in vivo parametric tumor perfusion map using DCE-CT

5.2.4 Oxylite Probe Measurements

The Oxylite oxygen probe was first inserted into a 21 gauge needle and mounted onto a 3-D micrometer stage. The probe was inserted laterally into the tumor and along the central axis through the tumor (figure 5.2.4.1), and incrementally recessed in 1 mm steps until the probe was completely removed from the tumor. At each step, pO₂ values were recorded every 5-10 seconds for 1-2 minutes until an equilibrium value was obtained. Once the pO₂ measurements were completed, PCT scans of the tumor were

obtained to determine and validate the insertion of the OxyLite probe. The corresponding SaO_2 at needle insertion locations were estimated from the PCT-S spectral images. Given the spatial sampling of the OxyLite probe is approximately 0.3mm, SaO_2 images were rebinned to 0.3mm prior to determining SaO_2 levels. The SaO_2 (PCT-S) and pO_2 (OxyLite probe) measurements were fit to Hill's equation to determine n and P_{50} of the tumor. Next, the hemodynamic parameters obtained from PCT-S and DCE-CT, in combination with metabolic rates from the literature (M_0), was used as inputs into the MPO2 model to calculate pO_2 . The correlation and linear regression analysis of OxyLite pO_2 and MPO2 pO_2 was performed.

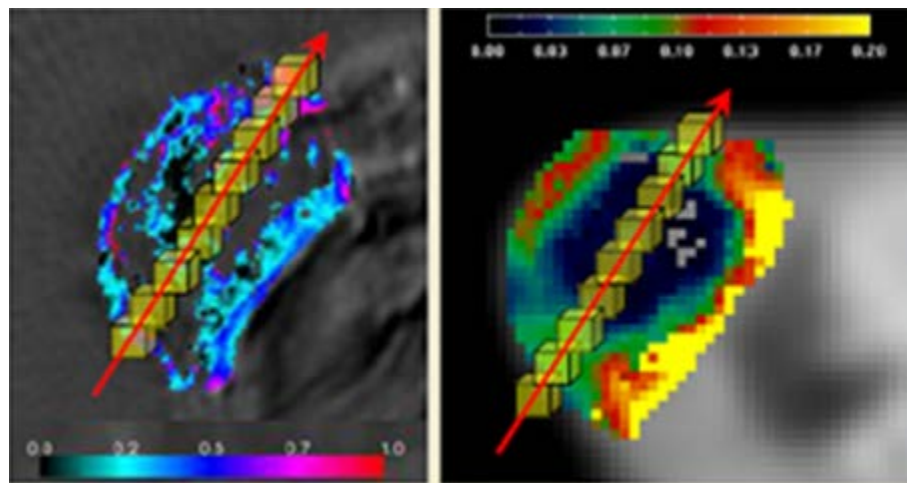


Figure 5.2.4.1: A 1.0 mm³ yellow cubic ROI was placed at position along a straight line through the center of the tumor, which approximates the actual position of the OxyLite probe (red).

5.3 Results

5.3.1 Comparing the Dissociation Curves for Blood in a Calibration Phantom and Breast Tumors

Displayed in Figure 5.3.1.1.A are the paired measurements of SaO₂ and pO₂ as measured by the co-oximeter and pO₂ OxyLite probe, respectively. Note that the fitted values for n and P50 are listed in lower-right corner. In Figure 5.3.1.1 B and C, the plots and fitted results for the pair measurements obtained from the MDA-231 and MCF-7 tumors are shown. Given a 10 percent uncertainty in the measured SaO₂ measurements using PCT-S, the Hill's coefficient (n) and P50 for MCF7 tumors are 1.76 (+/-0.25) and 17.2 (+/-1.3) mmHg, respectively, and for MDA-MD-231 tumor are 1.63 (+/-0.32) and 20.7 (+/-2.1) mmHg. The reduced chi-square values were 1.82 and 1.02, respectively.

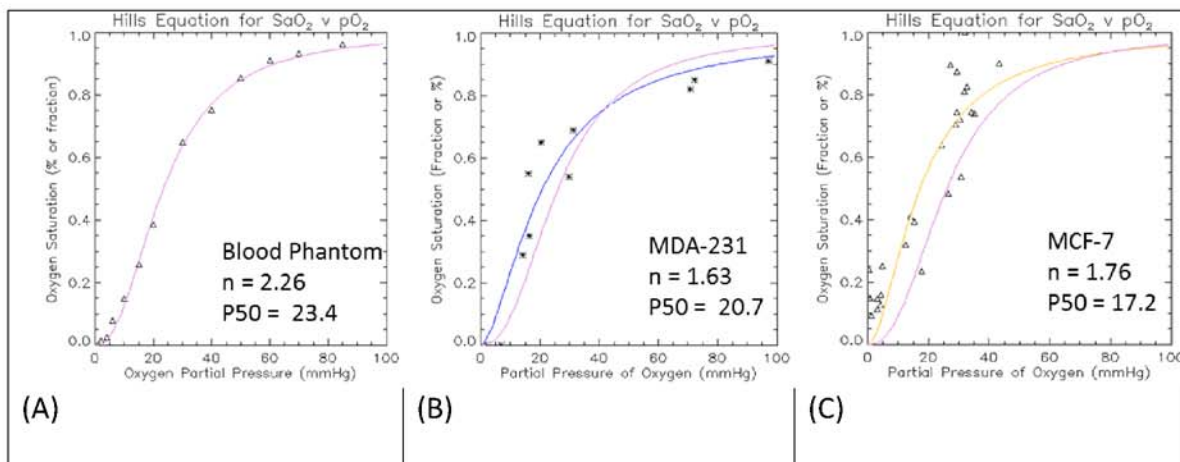


Figure 5.3.1.1.A-C: The oxygen saturation (SaO₂) and oxygen partial pressure (pO₂) plot of blood phantom (A), of MDA-231 tumor (B), and of MCF-7 tumor (C).

5.3.2 Comparing pO₂ Measurements Using MPO₂ Model and OxyLite Probe in MCF7

Breast Tumors

In figure 5.3.2.1.A-C, the local value for perfusion, fraction of plasma, and fraction of intracellular volume using DCE-CT are plotted as a function of distance along the central axis of the tumor. Similarly, the values for the hemoglobin concentration and oxygen saturation were calculated from PCT-S images (binned to 0.3 mm voxels), see figure 5.3.2.2.A-B. Given the inability to provide absolute position measurements, the imaging data was shifted along the central axis until overlap with OxyLite probe visually overlapped. These hemodynamic parameters were used as inputs into the MPO₂ model for pO₂ on a voxel-wise basis and compared to OxyLite probe measurements of pO₂ (see figure 5.3.2.3.A). The linear regression analysis for all the data points and after removing the outlier points are displayed in Figure 5.3.2.3.B-C, where the slope, y-intercept and p-value are (0.8,0.91), (0.9mmHg, 0.1mmHg), and (0.12, 0.07), respectively.

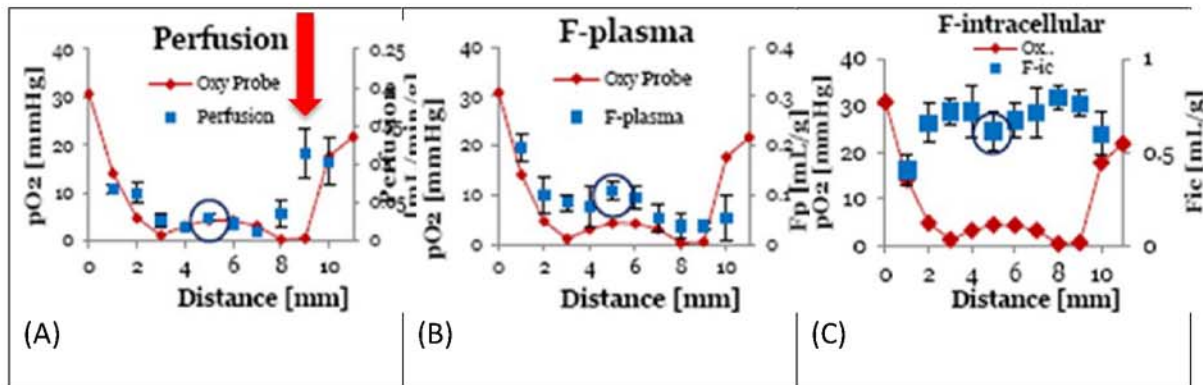


Figure 5.3.2.1.A-C: Co-localized vascular physiology (perfusion, F-plasma, and F-intracellular) quantification along the axial of track in MCF tumor. Red arrow in perfusion indicated the voxel with significant trend deviation of perfusion and pO₂ by OxyLite probe. The distance on horizontal axis represented the voxel position along the track.

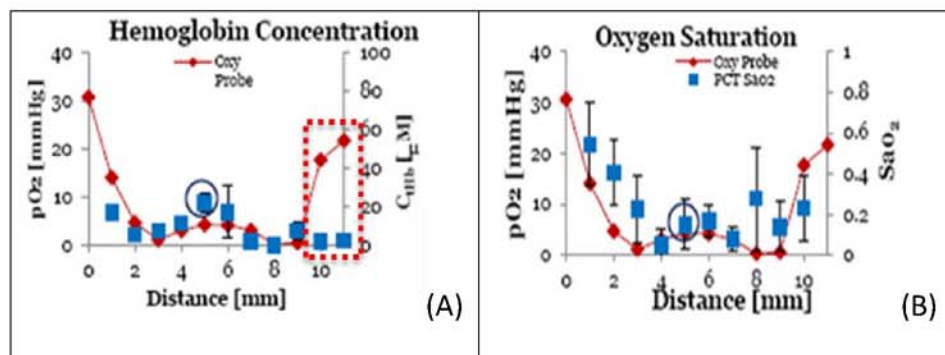


Figure 5.3.2.2.A-B: Co-localized hemoglobin and Oxygen saturation quantification. The voxels were coregistered with those in figure 5.3.2.1. The red dash box indicated two voxels with significant trend deviation of the hemoglobin concentration and OxyLite probe pO₂.

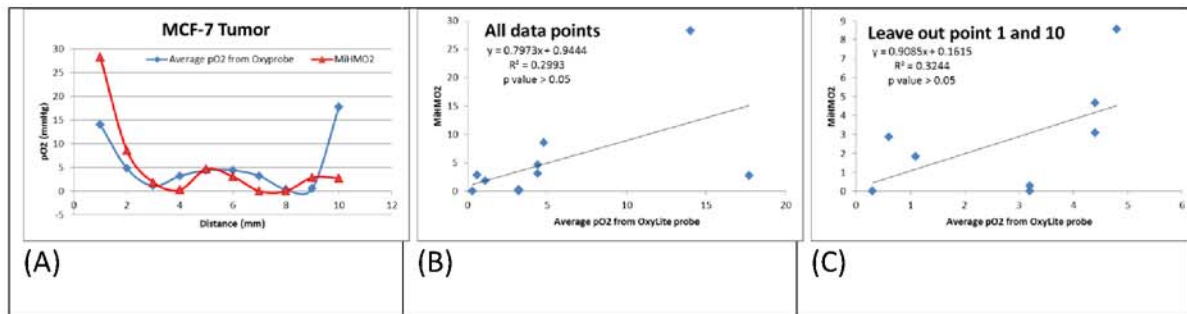


Figure 5.3.2.3.A-C: Correlation and regression of MPO2 and OxyLite pO₂ of MCF tumor.

5.3.3 Comparing pO₂ Measurements Using MPO2 Model and OxyLite Probe in MCF7

Tumors Receiving AAT

Previous section showed the MCF tumor vascular physiology quantifications using DCE-CT/PCT-S and the corresponding pO₂ using OxyLite needle probe. In this section the parallel measurements of a MCF tumor receiving anti-VEGF drug were demonstrated.

Figure 5.3.3.1.A-C demonstrated the local perfusion, fraction of plasma, and fraction of intracellular volume using DCE-CT; figure 5.3.3.2.A-B displayed hemoglobin

concentration and oxygen saturation. The linear regression analysis for all the data

points is displayed in Figure 5.3.3.3.B-C, where the slope, y-intercept and p-value are 1.5, 0.07mmHg, and 0.01, respectively.

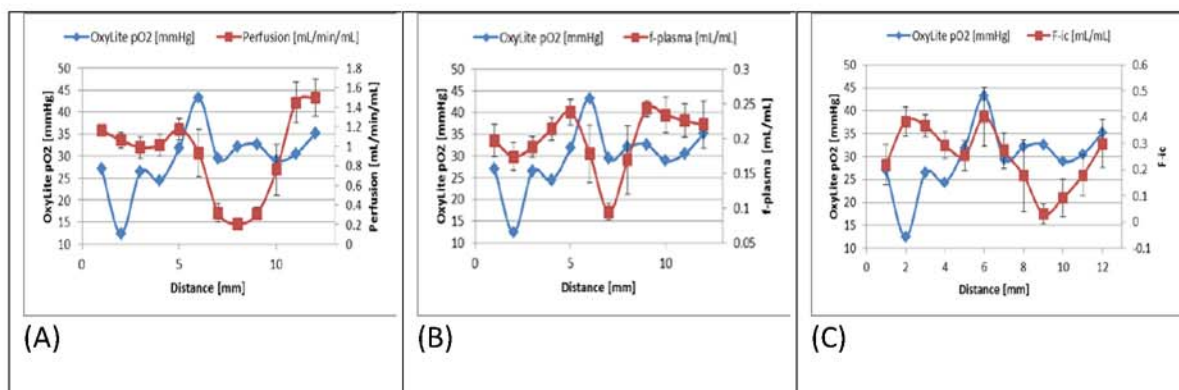


Figure 5.3.3.1.A-C: Co-localized vascular physiology (perfusion, F-plasma, F-intracellular) measurements of MCF/VEGF tumor.

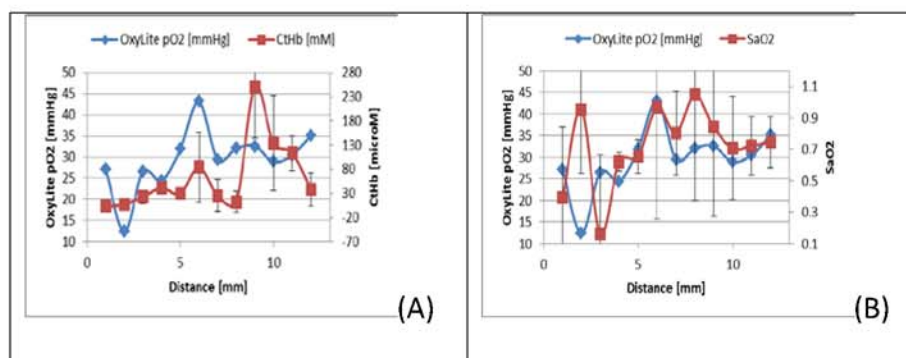


Figure 5.3.3.2.A-B: Co-localized hemoglobin and oxygen saturation of MCF/VEGF tumor.

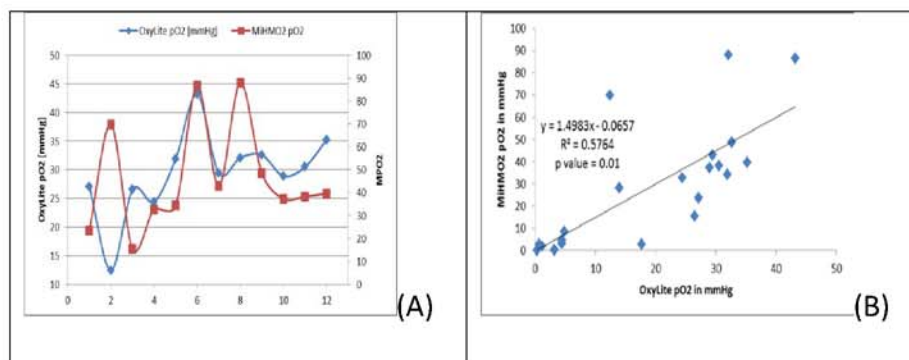


Figure 5.3.3.3.A-B: Correlation and regression of MPO₂ and OxyLite pO₂ of MCF/VEGF tumor. The regression analysis contained both MCF and MCF/VEGF data.

CHAPTER 6. MOUSE PANCREATIC TUMOR HYPOXIA QUANTIFICATION

6.1 MPO2 as a Means to Monitor the Efficacy of AAT

Over the years, the Stantz lab has been developing new imaging methods and animal models to study tumor angiogenesis and hypoxia. Dynamic contrast-enhanced CT method (DCE-CT) developed in this lab provides methods to quantify intra-tumor pathological parameters, such as blood perfusion, fraction of vessel volume, fraction of cell volume, and permeability, with high resolution ($\sim 300 \mu\text{m}$). The high resolution and fast acquisition of DCE-CT has enabled longitudinal monitoring of tumor progression and identification of tumor heterogeneity in structure and function aspects [127-129, 192]. In addition, the Stantz lab has developed photoacoustic imaging, a relatively new *in vivo* imaging modality capable of quantifying hemodynamic parameters including those discussed above and those associated with the hemoglobin status of red blood cells, e.g., oxygen saturation and hemoglobin concentration.

Recently, a preclinical study was performed to monitor the efficacy of antiangiogenic therapy (DC101, a monoclonal antibody blocking VEGFR2 activity) in combination with radiation therapy (RT), where DCE-CT was used to identify diagnostic parameters associated with radiation sensitivity in pancreatic tumors [74]. Given the high mortality rate of pancreatic patients and the inability to improve survival rates over the past 40 years [193, 194], developing new therapeutic regimens and diagnostic tool are urgently needed. In this section, the MPO2 model is used in an attempt to calculate the oxygen concentration and profile of mouse pancreatic tumors based on the vascular physiologies measured by DCE-CT. First, MPO2 model pO₂ values were compared to outcome (tumor growth) in these mouse pancreatic tumor studies. Second, the MPO2 was leveraged to investigate new aspects underlying tumor vascular associated with normalization.

6.2 Material and Method

6.2.1 Experiment Design

Six groups of nude mice were used to study the influence of AAT on RT in pancreatic tumors.

1. Controls (n=11). These mice did not receive DC101 or radiation therapy.
2. Radiation therapy cohort (RT; n=4, 12, 6 for 3-, 5-, 7-Gy dose). These mice received a single fraction of radiation.
3. High-dose DC101 cohort (HD, 150mg/kg; n=11). These mice received an intraperitoneal (i.p.) injection of 150 mg/kg DC101.

4. Low-dose DC101 cohort (LD, 40mg/kg; n=10). These mice received an i.p. injection of 40 mg/kg DC101.
5. High-dose DC101 plus RT (5Gy; n=6). These mice received an i.p. injection of 150 mg/kg DC101, and after one week post AAT, they received a single fraction of radiation (5Gy).
6. Low-dose DC101 plus RT (5Gy, n=8). These mice received an i.p. injection of 40 mg/kg DC101, and after one week post AAT, they received a single fraction of radiation (5Gy).

Human pancreatic carcinoma BxPC-3 cells (5×10^6) were subcutaneously injected into the flanks of 6- to 8-week-old female athymic nude mice (Harlan Sprague-Dawley), and allowed to grow to a diameter of 7 to 11 mm. DC101, a gift from ImClone Inc., was injected intraperitoneally at either a dose of 40 mg/kg (low-dose; LD) or 150 mg/kg (high-dose; HD). Radiation therapy was applied in a single fraction at a dose rate of 1.6Gy/min (X-RAD 320 Biological Irradiator) using an x-ray tube (kVp of 250KV). Mice of mono-DC101 groups (at both high dose and low dose) were subject to DCE-CT scan within 24 hours before injection and imaged again at day 2, 7, 14, and 21 after injection. Mice from combined therapy group had baseline scan before DC101 injection and 1-week post-DC101 injection. Immediately after the second scan, tumors on mice were treated with 5Gy x-rays. Therapeutic response, the tumor growth delay curve for each mouse was calculated by measuring the tumor volume every 3 days using calipers [74].

6.2.2 Impact of Perfusion on Pancreatic Tumor Hypoxia

Blood perfusion was found to correlate to the primary treatment outcome— the relative tumor growth rate. Medical physicists and oncologists discovered in the mid of 20th century that cell radiation sensitivity depends on oxygen concentration [62, 63]. It is conceivable that increased blood perfusion owing to tumor vessel normalization leads to an elevation in oxygen levels to more cancer cells in the tumor, thus enhancing radiation therapy. In this section, the (1) theoretical pO₂ for mice negatively and positively responding to radiation therapy (NRT and PRT) was compared to pO₂ values based on the MPO₂ model, where DCE-CT measurements were used as inputs; (2) the correlation of the theoretical pO₂ and the relative tumor growth rates were compared; and (3) the impact of vessel tortuosity to tissue oxygen concentration investigated.

Three theoretical schemes were designed to test MPO₂ by correlating experimental observation in the NRT and PRT cohorts to pO₂ model values (note, the average vascular attributes are listed in table 6.2.2.1). After DC101 treatment, blood perfusion in the PRT cohort remained close to baseline values (0.15 mL/min/g) while in the NRT group decreased to 0.10 mL/min/g. Since we did not have an accurate measurement of the hemoglobin concentration from this study, a value of 1.0 g/dL and 3.0 g/dL was used to compute the pO₂ value at the upper and lower ends of this range which was observed from various types of microvasculature by PCT-S. Two diagnostic parameters – the average pO₂ and hypoxic fraction (HF) – was calculated using the MPO₂ model to evaluate the influence of the vessel physiology on the oxygen status. HF represents the

percentage of cells in a region of interest falls under the established hypoxic threshold.

A 5 mmHg as hypoxic threshold was adopted in this study, hence HF5 means the percent of cells in a volume staying under 5 mmHg milieu.

Table 6.2.2.1: Average DCE-CT structural and functional measurements of the control (baseline), the positive responding tumor (PRT), and the negative responding tumor (NRT).

	Perfusion(mL/min/g)	f-plasma(mL/g)	F-cellular(mL/g)	Hct	SaO2	Tortuosity
Baseline	0.15	0.3	0.5	0.25	0.5	1 to 1.2
PRT	0.15	0.25	0.5	0.25	0.5	1 to 1.2
NRT	0.1	0.25	0.5	0.25	0.5	1 to 1.2

6.2.3 Impact of the Fractional Plasma Volume on Pancreatic Tumor Hypoxia

In previous section, the impact on hypoxia relief from blood perfusion normalization was addressed. To investigate the concomitant decrease in the blood vessel volume on hypoxia, the oxygen concentration at baseline for NRT and PRT cohorts using MPO2 using the parameters listed in table 6.2.2.1 were simulated.

6.2.4 Impact of Vessel Tortuosity on Pancreatic Tumor Hypoxia

Two distinct aberrant vessel structure features are overwhelming in tumor vasculature: tortuosity and vessel dilation. Tortuosity refers to the ratio of the sinuous vessel length to the straight distance between two ends of the vessel segment. Tortuous vascular path cripples the blood flow which is a dominant cofactor in oxygen transport. Structural normalization after AAT could correct for either or both abnormalities, depending on the mechanism of action. DCE-CT can only quantify the total vessel volume and not the detailed vessel configuration within a voxel. MPO2 model was

leveraged to analyze the influence of these structural changes associated with vascular normalization on tumor oxygen concentrations.

In Table 6.2.4.1, four hypothetical scenarios (A-D) were simulated comparing the tortuosity and vessel dilation on pO_2 . All other determinants of MPO₂ were held constant. The partial oxygen pressure (pO_2) in scenario A served as reference for scenarios B-D. Scenario B represented the pO_2 response from a 20% correction in vessel tortuosity and scenario C a 20% reduction in the radius. Scenario D and B had identical volume reduction, but the volume reduction in scenario D was driven by vessel dilation correction (geometrical normalization) while in scenario B by tortuosity correction (topological normalization). The oxygen status from scenarios B and D would demonstrate improved efficiency in the microcirculation with respect to vessel volume reduction.

Table 6.2.4.1: Four scenarios to compare hypoxia improvement by geometrical normalization against topological normalization.

	Radius in μm	Tortuosity
Scenario A	10.00	1.2
Scenario B	10.00	1.0
Scenario C	8.00	1.2
Scenario D	9.13	1.2

6.2.5 Simulation of DCE-CT and PCT-S Uncertainty

In previous section, the impact of blood perfusion, the fraction of plasma volume, and vessel tortuosity on the local oxygen concentration was investigated, where the SaO_2

and Hct were assigned as constant. The influence of the DCE-CT measurement uncertainty on the precision of pO₂ (MPO2-model) was simulated. In this pancreatic study, blood perfusion and the fractional plasma volume (f-plasma) were the two variables used in the MPO2 algorithm. In addition to f-plasma, the impact from the uncertainty in SaO₂ and Hct acquired by PCT-S was estimated to better understand the significance of the oxygen supply capacity in microcirculation to tissue oxygen concentration. Similar to the approach in section 4.1.8, these input parameters were varied by +/- 10%.

6.2.6 Mapping Pancreatic Tumor Hypoxia Heterogeneity

Recent studies have demonstrated that the pO₂ distribution in tumors is heterogeneous and may develop regions where tumor cells are exposed to chronic or acute forms of hypoxia. The implication of chronic and acute hypoxia in cancer therapy complication and cancer metastasis has recently received attention and currently under intense investigation[195-197]. MPO2 can be used to display 3D entire oxygen tension heterogeneity with high spatial resolution. In this section, MPO2 was used to provide map out pO₂ and HF5 distributions. Two mice, one from the PRT and NRT cohorts, were used to demonstrate the relationship of these parameters in the context of combined DC101 and radiation therapy. The parametric maps and histogram of the blood perfusion and fraction of plasma were analyzed and compared between NRT and PRT tumors.

6.3 Results

6.3.1 Experimental Observations of Pancreatic Tumor with DC101

Displayed in Figure 6.3.1.1-3 are the three major findings from the pancreatic cancer study: (1) Combined therapy (DC101 plus RT) showed greater inhibition in the relative tumor growth rate than mono-therapy (DC101 or RT), which indicated the treatment efficacy from the combined therapy was better than that of mono-therapy (see black markers versus gray markers in figure 6.3.1.1); (2) there was not a DC101 dose effect on tumor growth rates for either of the combined therapies (HD/LD DC101 + RT; gray circle versus square in Figure 6.3.1.1) or the monotherapies (HD/LD DC101; black circle v.s. square in figure 6.3.1.1); and (3) the vascular normalization occurred within 48 hours (see 6.3.1.2-C for detailed illustration).

With regard to the second finding, in addition to the tumor growth rate insignificance between HD/DC101 plus RT and LD/DC101 plus RT, the average blood perfusion and fraction of plasma of the combined therapy groups (HD/LD DC101 plus 5-Gy RT) showed no statistical significant difference as a result of high standard deviation [74]. Cao et. al. regrouped all mice from the two combined therapy groups based on changes in blood perfusion, thus forming a positive (radiation) responding tumor (PRT; blood perfusion at least 15% higher than the baseline perfusion) and a negative (radiation) responding tumor (NRT; blood perfusion at least 15% lower than the baseline). These two groups demonstrated a statistically significant difference in their tumor growth rates and in their average perfusion. The fractional plasma volume for these two groups remained

statistically equivalent (Figure 6.3.1.2 and 6.3.1.3). In comparison with the RT-only groups (5- and 7-Gy), PRT showed the lowest tumor growth rate over the 30 days of the experiment, while NRT had the worst tumor growth rate among four groups (figure 6.3.1.2). Three key conclusions were determined from the pancreatic study: **(1) blood perfusion was a reliable prognostic biomarker to evaluate pancreatic cancer combined treatment efficacy; (2) there was no clear correlation of blood perfusion normalization to DC101 dosage (based on body weight) in pancreatic tumors; and (3) DC101 normalized tumor vascular by modulating perfusion and not necessarily vessel structure as described in this chapter (some care must be taken given the interconnectivity of these two parameters).**

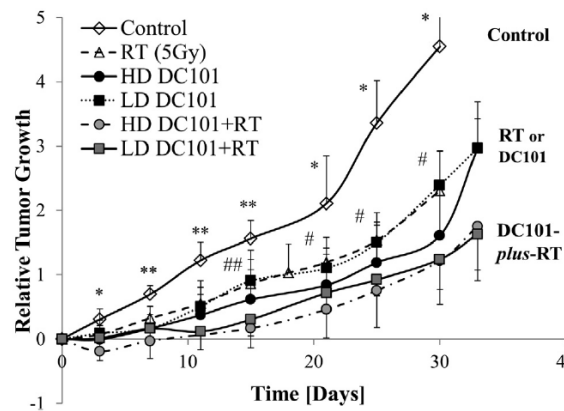


Figure 6.3.1.1: Relative tumor growth comparison of control, mono low-dose DC101, mono high-dose DC101, mono radiation therapy, DC101-plus-RT (HD and LD). (* $P < 0.05$, ** $P < 0.01$ control group to mono RT or DC101; # $P < 0.05$, ## $P < 0.01$ DC101 to DC101-plus-RT groups; error bar: standard deviation). Reprinted with permission from N. Cao[74].

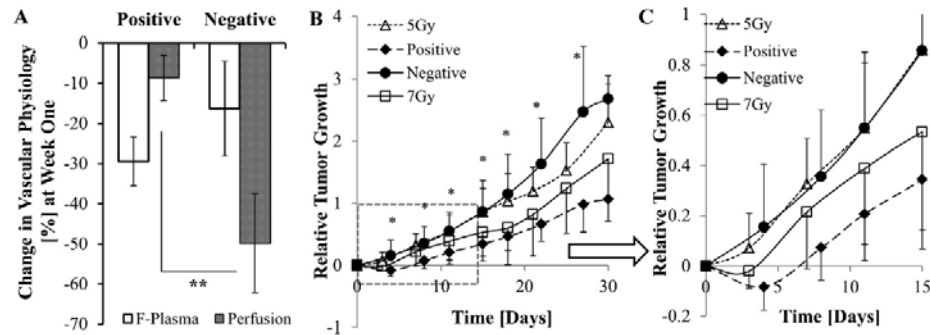


Figure 6.3.1.2: Key physiology adjustment in positive and negative responding group. (A) Average percentage change with respect to baseline in perfusion and fraction of plasma of the positive ($n=4$) and negative ($n=5$) responding tumors one week post DC101 treatment. Error bars represent the standard deviation (B-C) Relative tumor growth chart of the positive, the negative, mono-RT at 5Gy/7Gy over time. The valleys in PRT and 7-Gy RT indicated the onset of vessel normalization. Error bar indicates the standard deviation. (* $P<0.05$; ** $P<0.01$). Reprint permission by Cao et. al.[74].

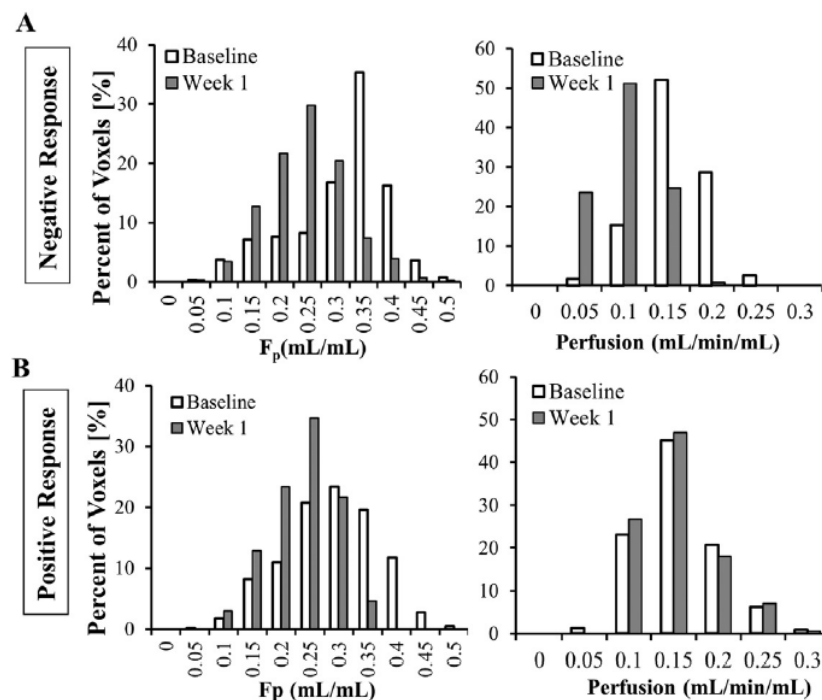


Figure 6.3.1.3: Blood perfusion(F) and fraction of plasma(Fp) histogram of PRT and NRT. Reprint permission by Cao et. al.

6.3.2 Simulation Results of Blood Perfusion to Hypoxia

The average pO₂ and hypoxia fraction at 5 mmHg (HF5) in PRT, NRT, and the control groups for all combinations of hemoglobin concentration (CtHb) and vessel tortuosity are displayed in figures 6.3.2.1 (CtHb = 1.0 g/dL) and 6.3.2.2 (CtHb = 3.0 g/dL). Since the pattern of two hemoglobin concentrations was similar and the pO₂ from 3g/dL hemoglobin concentration was close to the perivascular pO₂ determined by the microelectrodes[144, 178], the simulation outcomes of high hemoglobin concentration (3g/dL) was used to demonstrate all following simulation results.

Comparisons between the positive (PRT) and negative (NRT) responding treatment groups were performed to estimate the impact of blood perfusion on the local oxygen concentration, while holding the fractional plasma volume constant (0.25mL/g). Note, the PRT blood perfusion was 50% higher than that of NRT. Shown in Figure 6.3.2.2, the average pO₂ of the PRT cohort at a tortuosity of 1.0 (25.687 mmHg) surpassed the average pO₂ of the NRT cohort (17.032 mmHg). The corresponding improvement of in the pO₂ of the PRT group was 51% higher than NRT. Similar improvement was found in the other two tortuosity parameters. For the HF5 diagnostic parameter, MPO₂ identified an increase in the HF5 of 30% more for the NRT group compared to the PRT regardless of tortuosity.

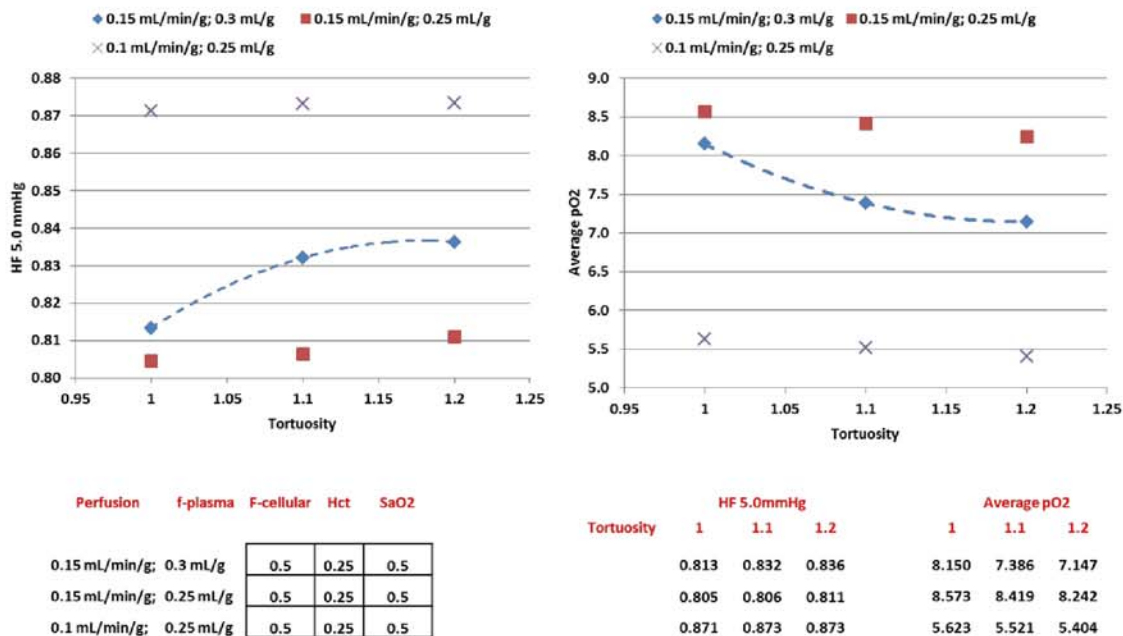


Figure 6.3.2.1: Average pO2 and HF5 of the positive and the negative responding group at hemoglobin concentration 1.0 g/dL. Two plots on the top illustrate the HF5 and the average pO2 of three groups at MPO2 tortuosity from 1 to 1.2. Blue diamonds connected with dash lines highlight the baseline reference in HF5 and the average pO2 plot. Table on the bottom lists the MPO2 determinants to compute the pO2 distribution in a voxel size = 300 μ m and the corresponding numerical pO2 result in median pO2, average pO2, and HF5 at various tortuosity.

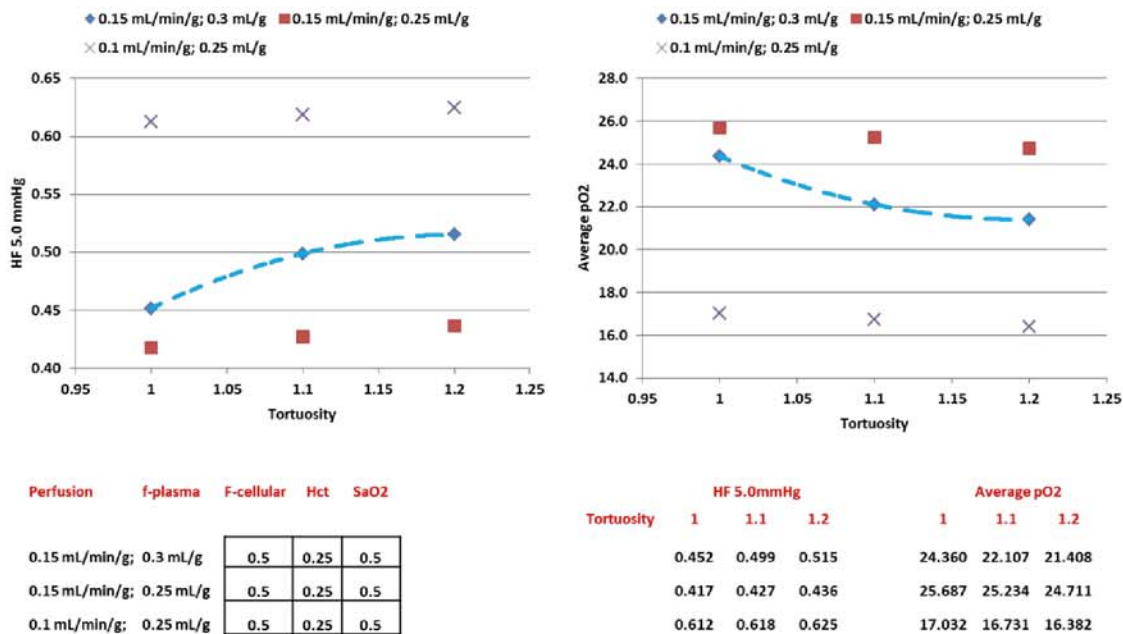


Figure 6.3.2.2: Average pO2 and HF5 of the positive and the negative responding group at hemoglobin concentration 3.0 g/dL. Please read the caption in Figure 5.6.2.2 for description.

6.3.3 Simulation Results of Fraction of Plasma to Hypoxia

The fraction plasma volume relates the size of the effective vessel in MPO2. To evaluate its impact, the pO2 of the positive responding group (PRT) was compared to the control, since they had on average the same blood perfusion (0.15 mL/min/g). However, the fractional plasma volume of the control tumors was approximately 17% higher than that of the PRT. The improvement in the pO2 from the fractional plasma volume was only about 5% when the tortuosity of both groups was equal to one. This pO2 difference however increased to 14% and 15% when the tortuosity increased to 1.1 and 1.2, respectively. The changes in the HF5 were similar to the average pO2.

6.3.4 Simulation Results of Vessel Tortuosity to Hypoxia

Tortuosity relates to the topological complexity of network architecture. It is conceivable that two vasculatures with identical total vessel volume but different tortuosity yield diverse blood flows and pO_2 outcomes. Three tortuosity values were assigned – 1.0, 1.1, and 1.2 – in MPO2 to investigate the impact of vessel tortuosity on tissue oxygenation. In all three groups (the control, the PRT, and NRT), MPO2 showed that a highly tortuous vessel (1.2) reduced the pO_2 compared to normal vessels (tortuosity of 1.0). In the NRT group, the reduction in pO_2 due to tortuosity (1.0 versus 1.2) was nearly 14%, while in the PRT and control groups, this reduction was 4%.

6.3.5 Simulation Results of Synergistic Normalization to Hypoxia

Previous MPO2 analysis considered the impact from individual physiological attributes on the tumor's pO_2 . Tortuosity in the PRT was most likely less than the NRT and control groups, thus the improvement in the pO_2 levels between PRT and NRT groups as reported in the blood flow section should be more than 51%. If DC101 normalized tortuosity in the PRT group (1.0) but failed in NRT group (1.2), the improvement in the pO_2 was due to the synergy between favorable blood flow and tortuosity and would be approximately 57%. ***This improvement should become more significant when the difference in tortuosity becomes even higher.***

6.3.6 Simulation Results of DCE-CT and PCT-S Uncertainty

MPO2 response to the uncertainty from the fraction of plasma(f-plasma). The simulated f-plasma uncertainty of 10% in the control, PRT, and NRT was ± 0.03 mL/g, 0.025 mL/g, and 0.025 mL/g, respectively. Accordingly, the corresponding lower and upper f-plasma in these three groups was 0.3 ± 0.03 (control); 0.25 ± 0.025 (PRT); and 0.25 ± 0.025 (NRT). The error bars in figure 6.3.6.1 indicate the resulting pO_2 with the lower and upper f-plasma for hemoglobin concentrations set at 1.0 and 3.0 g/dL and tortuosity set at 1.0, 1.1 and 1.2. For high or low hemoglobin concentrations, the pO_2 difference between the PRT and NRT groups remained significant for a 1.1 or 1.2 tortuosity value. The pO_2 difference for a tortuosity of 1.0 between the control and PRT group became insignificant, while either one with respect to NRT remained significant.

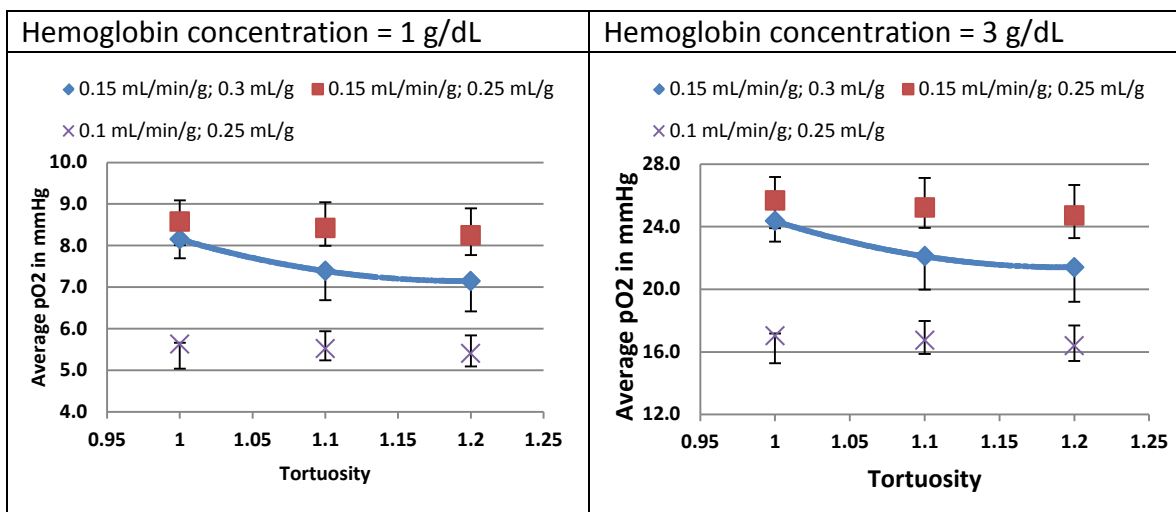


Figure 6.3.6.1: Sensitivity test of fraction of plasma in MPO2. The upper and lower value of an error bar is determined by MPO2 with upper and lower f-plasma (1.1 and 0.9 times of the average f-plasma).

MPO2 response to the uncertainty from oxygen saturation (SaO_2). An average SaO_2 of 0.5 was assigned to all three groups, and a 10 percent uncertainty in SaO_2 was investigated (e.g., a value of 0.45 and 0.55 for the lower and upper limits). This uncertainty in the SaO_2 (figure 6.3.6.2) demonstrated a nonlinear response, but did not nullify the significance in pO_2 difference between PRT and NRT at any tortuosity. This result was expected because the blood perfusion for the PRT group was 50% higher than that of NRT after DC101 treatment, where the tissue pO_2 in oxygen concentration improvement resulting from the robust increase in blood perfusion surpassed the concern of the 10 percent SaO_2 uncertainty.

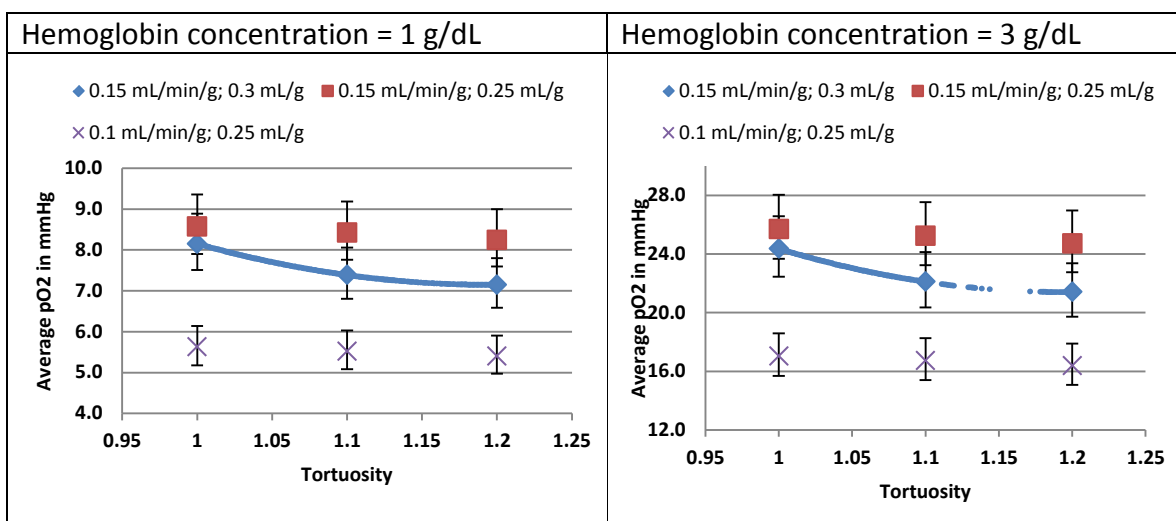


Figure 6.3.6.2: Sensitivity test of SaO_2 in MPO2. The upper and lower value of an error bar is determined by MPO2 with upper and lower SaO_2 (1.1 and 0.9 times of $\text{SaO}_2 = 0.5$).

MPO2 response to the uncertainty from hematocrit (Hct). Similar to SaO_2 , the hematocrit (Hct) was assigned a value of 0.25 based upon the observation from PCT-S and literature. The uncertainty test of Hct was identical to f-plasma and SaO_2 . In Figure

6.3.6.3, the 10 percent uncertainty in the hematocrit had the highest impact on pO₂ in the control group, and minimum influence to the pO₂ in the positive responding tumors.

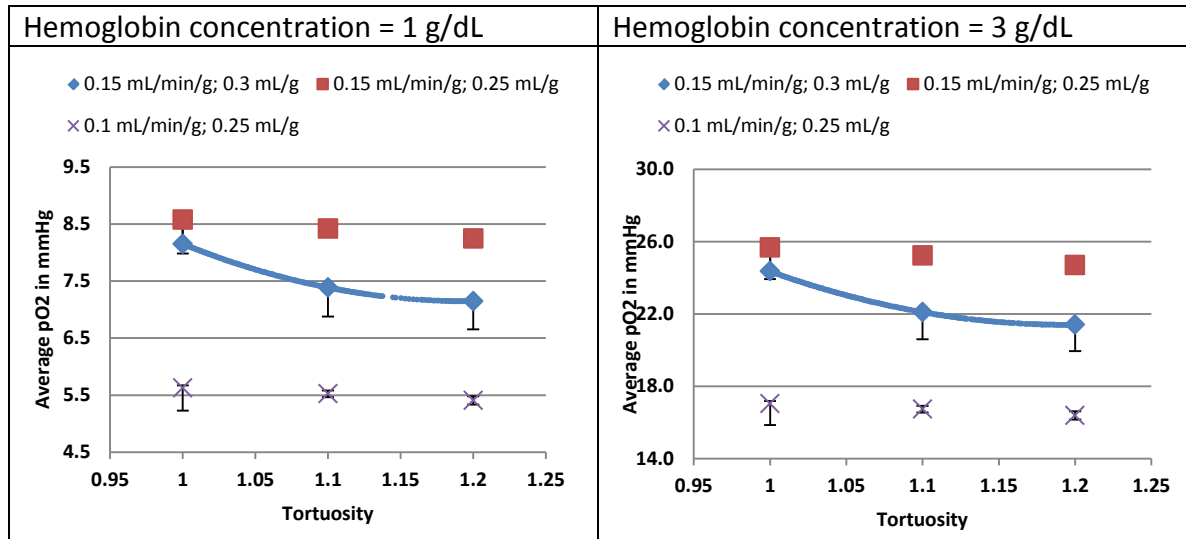


Figure 6.3.6.3: Uncertainty test of Hct in MPO2. The upper and lower value of an error bar is determined by MPO2 with upper and lower Hct(0.225 and 0.275).

6.3.7 Tortuosity Normalization vs. Dilation Normalization

Displayed in Table 6.3.7.1 is a summary of the oxygen level response from (1) 20% tortuosity reduction, (2) 20% dilation reduction, (3) competition of tortuosity and dilation correction under the condition of even volume reduction. These results show that for the same percent correction, the vessel tortuosity was more efficient than correcting for the vessel dilation when trying to increase tumor oxygen levels. Note, the reduced vascular volume based on the 20% correction in dilation (vessel radius) is 30% more than 20% tortuosity correction. The same observation was found under the condition of equal volume reduction. For example, a 3.0 g/dL hemoglobin concentration (scenario D; topological normalization) improved the average oxygen level 20% with

respect to the reference (scenario A), while scenario B (geometrical normalization) improved oxygen levels by only 8%. In terms of HF5, topological normalization reduced hypoxic fraction by 19%, while geometrical normalization by only 7%. These findings support the idea of the diverse mechanisms contributing to AAT-induced vessel normalization.

Table 6.3.7.1: Oxygen response of various normalization mechanisms

Result of Hb = 1.0 g/dL			
	(HF5, Average pO ₂)	% change of HF5	% change of ave. pO ₂
A: R=10 μ m, tort = 1.2	(0.836, 7.147 mmHg)		
B: R=10 μ m, tort = 1.0	(0.805, 8.573 mmHg)	3.72 %	-20%
C: R=8 μ m, tort = 1.2	(0.807, 8.570 mmHg)	3.47 %	-20%
D: R=9.13 μ m, tort = 1.2	(0.824, 7.75 mmHg)	1.4 %	-8.4%
Result of Hb = 3.0 g/dL			
A: R=10 μ m, tort = 1.2	(0.515, 21.41 mmHg)		
B: R=10 μ m, tort = 1.0	(0.417, 25.69 mmHg)	19%	-20%
C: R=8 μ m, tort = 1.2	(0.425, 25.57 mmHg)	17%	-19%
D: R=9.13 μ m, tort = 1.2	(0.478, 23.17 mmHg)	7%	-8%

6.3.8 Oxygen Concentration Maps of the Pancreatic Xenograft Tumors

In Figures 6.3.8.1.A-D, the four montages are summarized for a single mouse. The top panel of each montage displays the perfusion and f-plasma histograms of the two tumors (red arrow indicated the location of the average value); the middle panel displays the tumor blood perfusion and f-plasma maps (DCE-CT); the bottom panel displays the theoretical pO₂ and HF5 distribution as determined by the MPO₂ model. Displayed in Figures 6.3.8.1.A-D are the abnormal heterogeneous blood perfusion and f-plasma distribution in the pancreatic tumors. In the PRT mouse (figure 6.3.8.1.A-B),

tumors one-week after DC101 treatment showed a similar distribution of perfusion and f-plasma relative to baseline values, but a reduced the spread in histogram. In the NRT mouse (Figures 6.3.8.1.C-D), DC101 significantly reduced both the average blood perfusion and the spread in histogram (or heterogeneity in distribution map).

The wide range in f-plasma and low variance in f-plasma frequency distribution at baseline suggests the existence of highly chaotic vessel structure in tumor. In each PRT tumor, the perfusion distribution at baseline (prior to DC101 treatment) was similar to that at week-one (one week post DC101 treatment); however the perfusion distribution of the NRT tumors at week-one was different from baseline.

The fractional plasma volume (f-plasma) at baseline and week-one post-DC101 indicated a reduced overall vessel volume but maintained a spatial heterogeneity in both NRT and PRT mice. Perfusion in the PRT mice did not decrease post-DC101 treatment as shown in the histogram, where the sub regions in tumor with high perfusion (hot spots) moved to different part of tumor and the heterogeneity appeared to be unchanged between the baseline and the week one groups. The map of HF5 tracked that of pO₂. DC101 alleviated the global oxygen concentration in the tumor; however, some regions clearly remained highly hypoxic, subsequent influence from those highly hypoxic domains to tumor metastasis is unknown and requires further investigation.

Figure 6.3.8.1.A: Positive responding group: Mouse 174302.M1

Left tumor(LT) perfusion and f-plasma at baseline and week one

Right tumor(RT) perfusion and f-plasma at baseline and week one

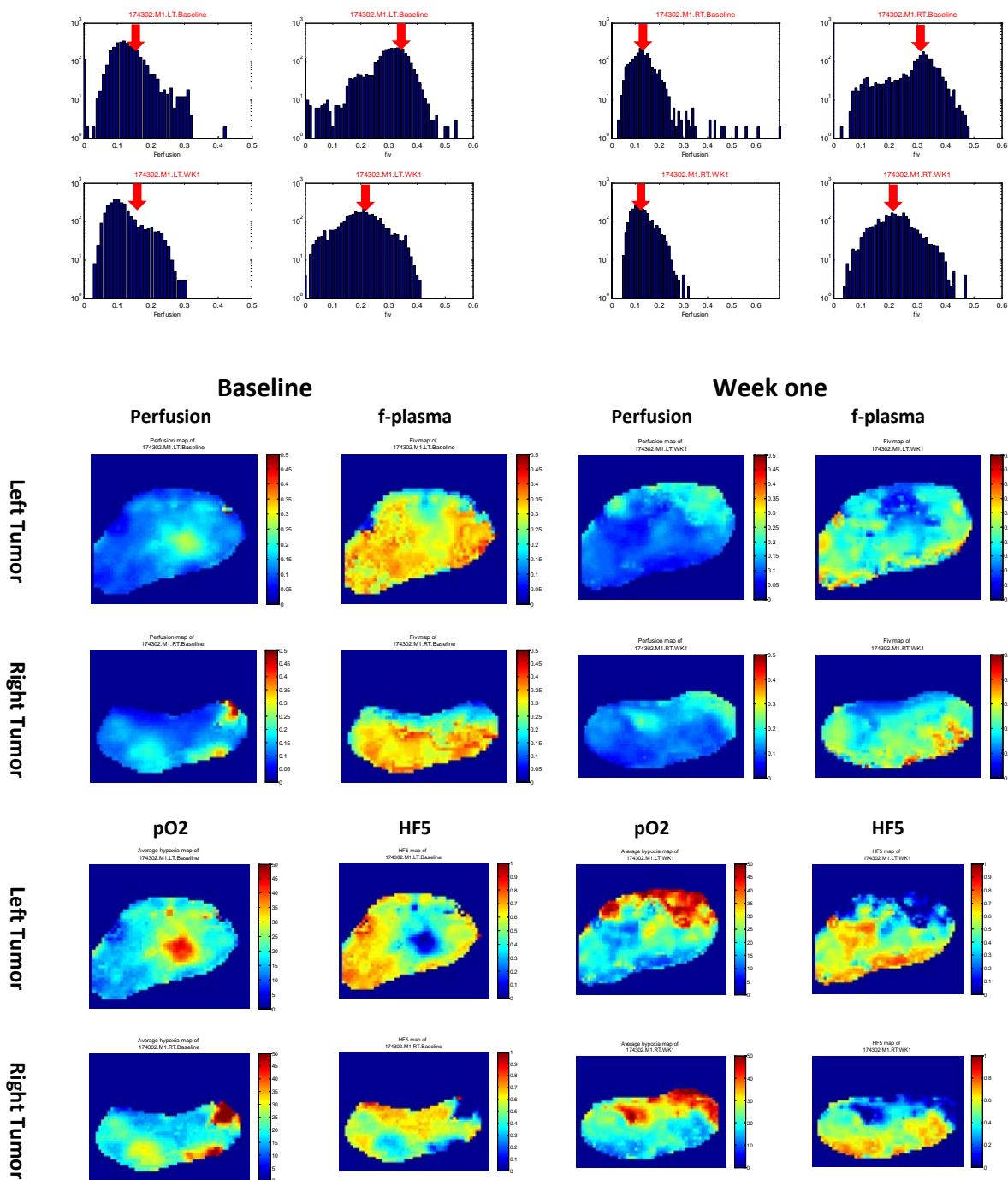


Figure 6.3.8.1.B: Positive responding group: Mouse 174302.M3

Left tumor(LT) perfusion and f-plasma at baseline and week one

Right tumor(RT) perfusion and f-plasma at baseline and week one

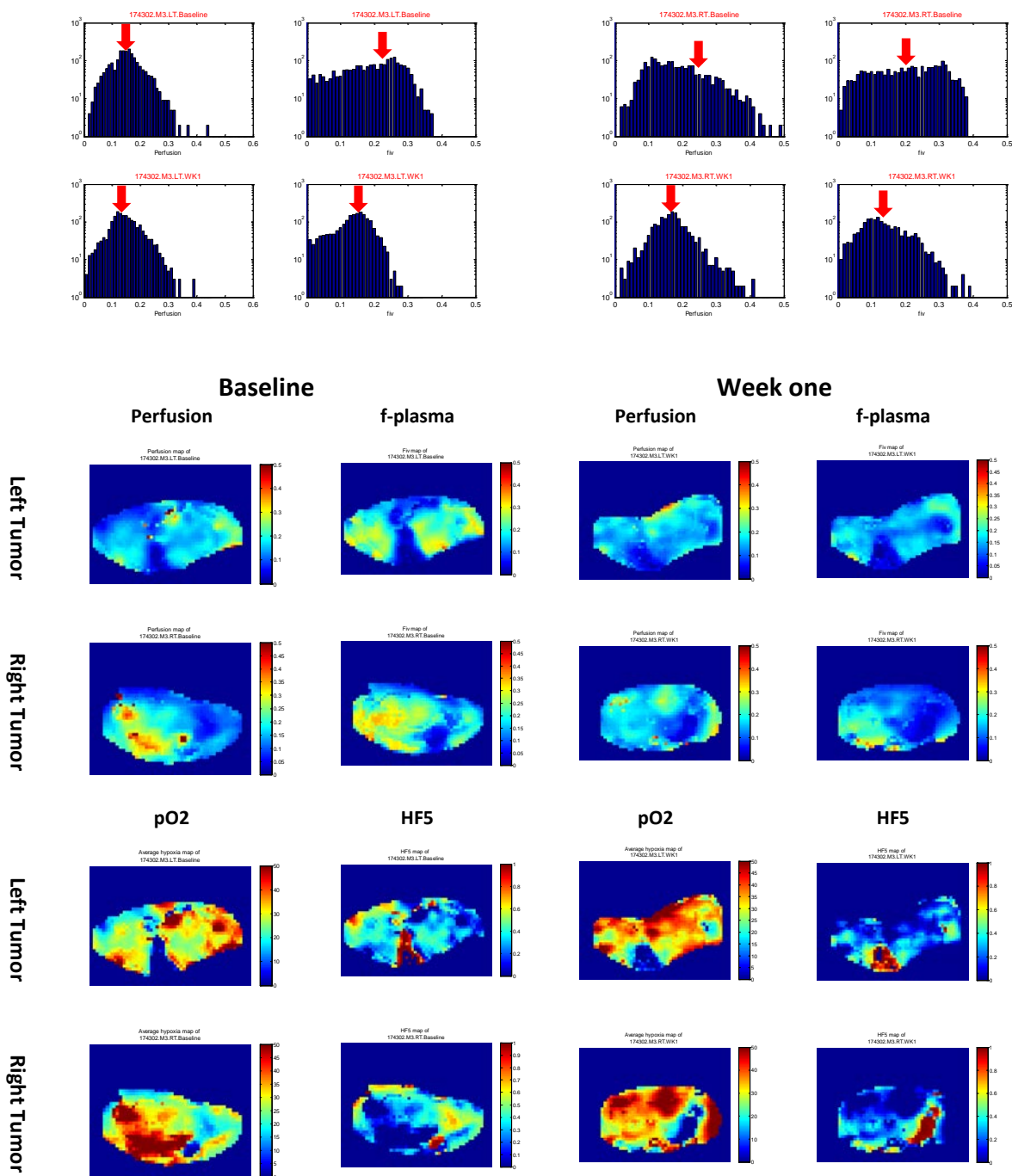


Figure 6.3.8.1.C: Negative responding group: Mouse 174303.M1

Left tumor(LT) perfusion and f-plasma at baseline and week one

Right tumor(RT) perfusion and f-plasma at baseline and week one

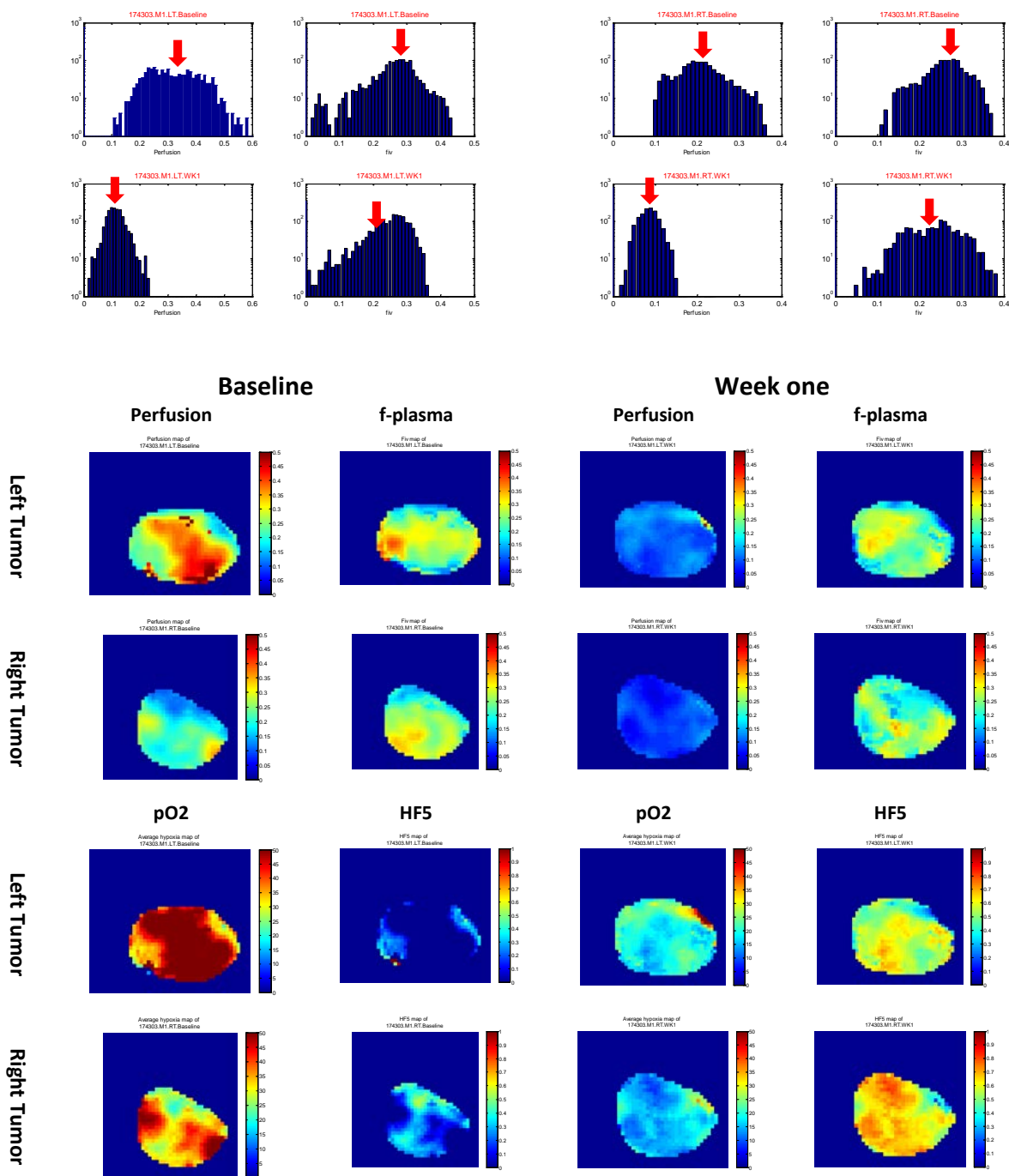


Figure 6.3.8.1.D: Negative responding group: Mouse 174303.M3

Left tumor(LT) perfusion and f-plasma at baseline and week one

Right tumor(RT) perfusion and f-plasma at baseline and week one

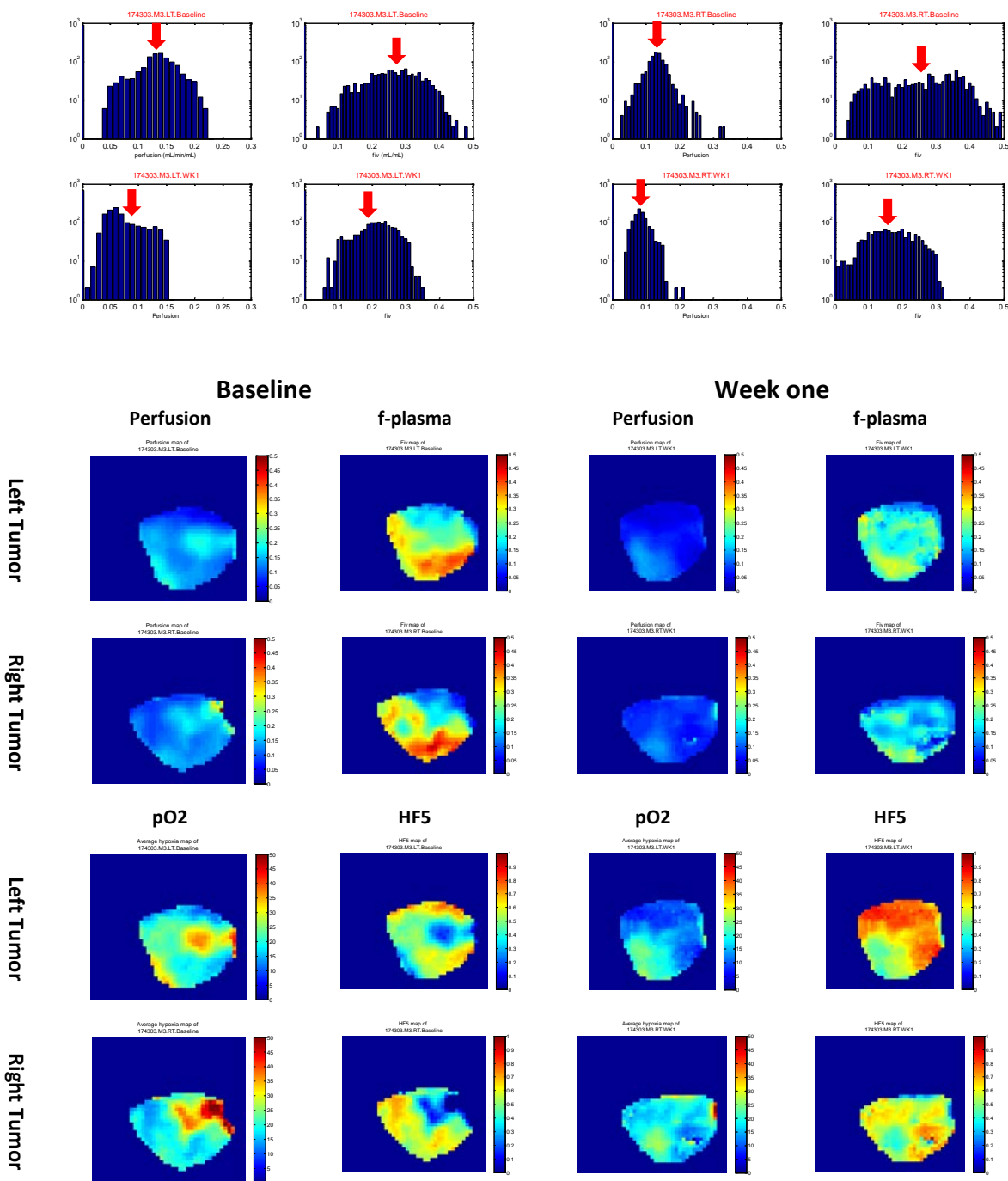


Figure 6.3.8.1.A-D: Histogram and distribution of key MPO2 inputs and outputs. Each figure displays a single mouse DCE-CT functional quantification and the corresponding simulated tumor pO2 status at baseline(pre-DC101) and one week post DC101 treatment. Each figure is composed of three sections: perfusion/fraction of plasma

volume(f-plasma) histogram on the top; perfusion(F)/f-plasma montage at the middle; simulated pO₂/HF5 montage on the bottom. The middle montage demonstrates the perfusion and f-plasma map of two tumors in a mouse determined by DCE-CT in single voxel resolution; the top histogram displays the perfusion and f-plasma value distribution from all voxels in the tumor shown in the middle montage. Two histograms on the left of histogram panel represent the blood perfusion in voxel at baseline and week one; two histograms on the right show the distribution of the fraction of plasma in voxel. The red arrow in the histogram indicates the location of the average value from all voxels. The bottom montage displays the simulated pO₂ and HF5 in each voxel by MPO2 adapting the corresponding voxel perfusion and f-plasma inputs. In the title of each figure, LT represents left tumor; RT: right tumor; WK1: week one.

CHAPTER 7. DISCUSSION

7.1 Mathematics in Biology and Medicine

Mathematics is widely used in the fields of Physics, Chemistry, and Engineering.

Mathematics in theoretical Physics and Chemistry is no longer used merely as a technique aid but as a conceptual tool for the foundation of new hypotheses and the parameters to test these hypotheses. In the Life Sciences, mathematicians and biologists, including medical scientists have a long history working together. In comparison to other scientific fields, mathematical biology or biophysics is highly interdisciplinary which requires an understanding of both biology and mathematics, where systems are often nonlinear and complex, involve multiple signaling pathways or biomechanisms, and far from a simplified ideal system. Moreover, experimental verification of these mathematical models of these biological systems are often difficult due to technical challenges to obtain data noninvasively, the inability of identifying relevant measurable parameters and bridging the microscopic and macroscopic, and the need to simultaneously acquire several parameters due to complexity of the system. In spite of these challenges, significant progress in understanding and solving fundamental biological problems has and will continue to occur by concurrently developing and advancing theoretical biophysical models and technology.

7.1.1.1 Using GPO2 as a Standard to Validate MPO2

In this study, a novel integrative approach was proposed to fuse multiple *in vivo* imaging parameters based on mathematical models capable of quantifying tumor hypoxia with high spatiotemporal resolution. The biophysical presumption underlying this approach states that a single vessel with multi-functional attributes can adequately represent the real microvasculature, and if the voxel was *small enough*, the pO₂ calculated using this model (MPO₂) would approach the actual pO₂ exerted by the local vasculature (see figure 3.1.5.1). The key to the success of this methodology relies on an accurate measure of the tissue's vascular hemodynamics and metabolic rate within a single voxel. Recent advances in the spatial resolution and acquisition speeds of *in vivo* imaging can realize such a methodology. However, testing and validating such a model is difficult, requiring the measurement and co-localization of vascular physiology, hemoglobin status, and oxygen metabolic rates. To the best of our knowledge, this has yet to be accomplished. To overcome this obstacle, an alternative approach was developed where the pO₂ was calculated using a network-based model approach – Green's function model (GPO₂) – and used as a standard or reference. This reference model was compared to the modified multivariate Krogh model (MPO₂), which was used for image fusion. Validation of MPO₂ mathematical model by GPO₂, another mathematical model based on Green's function solution, invites some concerns, but again this is a logical first step to test the feasibility (limitations) of the proposed MPO₂ technique. Green's function considers every vessel segment contribution to the local oxygen concentration level, highlighting the importance of vessel geometry and

topology to oxygen transport. A second, or more important feature, is that the computed pO₂ based on GPO₂ was verified by the experimental measurement [198]. To date, this is the only report directly comparing experimental data and theoretical oxygen transport models. Yet, the microvessel structure and functional parameters (or attributes) used in this study were acquired by the integration of the intravital confocal scanning microscopy with other optical techniques, where the intrinsic photon penetration depth is limited to the superficial vasculature. Given that a tumor's vasculature might be structurally and functionally different from those near the periphery, these results are only representative of a tumor.

7.1.2 Discrepancy Between the PO₂ Calculated from MPO₂ and GPO₂ Models

In Figure 4.3.3.2, the correlation between GPO₂ and MPO₂ was dependent on the voxel size or spatial resolution of the imaging system. Voxel size in the range from 50 to 200 μm showed a better coefficient of determination (R^2) compared to 250 and 300 μm in a tumor. For larger voxels sizes, the increased vascularity degraded the correlation between pO₂ values. Increasing the complexity of the model (two parallel cylinders) did not improve these results (see Appendix for method of a multi-vessels MPO₂ model). Unlike the tumor, there were no outliers for 50 μm voxels in the brain tissue. This discrepancy reflects the underlying difference between the physiological and pathological angiogenesis. The average inter vessel distance in the tumor was higher than that in the normal vessel network of the brain. In the tumor, two outlier groups

were observed: (1) the overestimated group, of which MPO₂ was greater than GPO₂, and (2) the underestimated group, of which MPO₂ was lower than GPO₂. The location of all outlier voxels was identified and highlighted the inappropriate assumption in the boundary conditions used in MPO₂. Most of the overestimated voxels enclosed one vessel segment imperceptibly clipping through the voxel corner and the underestimated 50- μm voxels were filled with several vessels or a large vessel (arteriole). Another underestimation scenario occurred when the voxel resided nearby the large vessel segments. Given that the largest tumor vessel diameter was close to 60 μm and 13 percent of the tumor vessel segments possessed a diameter greater than 30 μm , it is conceivable that a voxel near to the large vessel segments results in a significant amount of oxygen diffusion from a neighboring voxel (or arteriole). To correct the outlier problems, a nearest neighbor algorithm was implemented, which formed a new boundary condition and significantly improved the correlation of the outliers. The linear regression displayed in Figure 4.3.4.2(A) demonstrates the significant improvement in the results.

A sensitivity analysis was performed where a systematic change in each parameter was plotted while holding all other parameters constant, see figure 4.3.2.1. Blood perfusion, oxygen consumption, oxygen saturation (SaO₂), and hemoglobin concentration (CtHb) all influenced oxygen transport in a similar fashion and magnitude. Overall, the vessel diameter had the least influence, while the importance of SaO₂ and hemoglobin

concentration underlines the importance of photoacoustic spectroscopy (PCT-S) in predicting pO₂. New contrast-enhanced PCT-S imaging currently being developed in the Stantz lab will provide simultaneous acquisition of the vessel structure, physiology in addition to the oxygen saturation and hemoglobin concentration critical for MPO₂ determination of pO₂. This can reduce image acquisition time and bypass the uncertainty from image co-registration procedure. However, the importance of oxygen metabolism remains critical in determining local oxygen concentration. Cellular density in a tumor can be highly heterogeneous. Since MPO₂ considers the fraction of cells from DCE-CT (fraction of cell volume = 1 – fraction of vessel volume – fraction of interstitial volume), MPO₂ can provide a more accurate measure of pO₂ than Green's function algorithm. In these simulations, the cancer cell metabolic rate was assumed to be either at its maximum or dormant, which has yet to be validated, and can contribute to the uncertainty in the pO₂. In chapter 4, the potential error (precision and accuracy) in pO₂ due to measurement error in perfusion and fractional plasma volume was investigated. The average coefficient of variance (CV) of pO₂ due to blood perfusion and fraction of vessel volume error was close to 3.3% and 7.0% and considered relatively small, assuming a 20 percent uncertainty in these measured parameters (based on commercial high-resolution CT imaging scanners).

The simulations performed in this study demonstrate the feasibility of the MPO₂ method to quantify oxygen concentration and obtain hypoxic fractions in a tumor, but with some limitations. For example, the voxel size or spatial resolution should ideally be

200 μm or smaller. By including 20 percent noise into the parametric images, which is consistent with measured values, the linearity and variance remained less than 7 percent. Together with the result from sensitivity test, future oxygen profiling experiments should focus on PCT for both physiological measurements (DCE-PCT) and hemoglobin status, SaO₂ and CtHb (PCT-S). Replacing DCE-CT has two main advantages, better spatial resolution and mitigating unnecessary dose from ionizing radiation; however, quantification remains unproven in DCE-PCT and *in vivo* imaging remains limited due to signal loss at depth.

7.2 *In vivo* Validation of MPO₂ Using the OxyLite Oxygen Sensor

In specific aim 1, the MPO₂ model was investigated at various voxel sizes. For voxel sizes ranging from 500-200 μm , a correlation between the pO₂ based on the microscopic measurements and Green's function solution to oxygen transport and *in vivo* imaging and MPO₂ model. For specific aim 2, the voxel size implemented was set to 300 μm , which was based on the range or field-of-view of the OxyLite probe and the *in vivo* imaging modalities used in this study. As a first step, To calibrate the OxyLite probe, pO₂ and SaO₂ in blood was obtained using the OxyLite probe and co-oximeter, respectively, from which the dissociation curve associated with the red blood cells was plotted, with little scatter in the data. Both Hill's coefficient, n , and P50 (2.26 and 23.4 mmHg) are consistent with reported values [135], validating both the OxyLite probe and technique against a Gold Standard (co-oximeter). Within the tumor, reductions in P50 were

observed (17.2 and 20.7 mmHg) are consistent with microenvironmental factors influences the dissociation curve, such as acidosis (reduced pH). The acidosis of tumor was arguably responsible for low n and P50; however, additional experiments will be required to confirm this hypothesis.

Next, DCE-CT and PCT-S scans were acquired to determine the key vascular physiological arguments to MPO2 model. Ideally, both DCE-CT and PCT-S should be acquired within a short time to minimize cycling effects and improve the accuracy and precision of pO₂. IN this study, these measurements were 30-90 minutes apart. Although the measurements of DCE-CT and PCT-S were not quantified simultaneously, the overall trend ($P < 0.1$) of MPO2 to OxyLite pO₂ was observed. The high deviation of blood perfusion (figure 5.3.2.1.A) and hemoglobin concentration (figure 5.3.3.2.A) at the both ends (point 1 and 10) resulted in high discrepancy between MPO2 and OxyLite pO₂. Other factors affecting the accuracy and precision include the accuracy at which PCT-S, DCE-CT, and OxyLite probe can be spatially co-localized and the influence of a 300 mm range (or voxel size) on MPO2.

7.3 MPO2 Analysis on PRT and NRT Tumors Post DC101 Administration

Cao et. al. used DCE-CT to longitudinally monitor the vascular and tumor physiology in the mouse xenograft pancreatic tumors subject to mono AAT (DC101) or radiation therapy or both. They adapted a blood perfusion threshold to regroup the mice receiving the combined therapy (AAT plus RT) into the positive responding group (PRT)

and the negative responding group (NRT). The average blood perfusion of the positive responding tumor (PRT) was 50% higher than that of the negative responding tumor (NRT); the fraction of plasma of PRT showed statistically equal to that of NRT. Blood perfusion is a robust surrogate marker since it significantly correlates to the primary outcome in this study-- the relative tumor growth rate. The finding suggested that increased blood in PRT improves the oxygen concentration in tumors which enhances the following radiation sensitivity to kill tumor cells. This study also provided an opportunity to apply MPO2 to calculate tumor oxygen concentration. Although there were no SaO₂ and Hct measurements, we used SaO₂ = 0.5 and Hct = 0.25 in MPO2 simulation, which were close to the PCT-S observations of many tumors in our lab.

The theoretical assessment supported the Cao's findings that blood perfusion is a reliable surrogate marker to predict the combined therapeutic outcome of pancreatic xenograft tumors with DC101 as AAT agent, and proved the significant tumor hypoxia relief due to the increased blood flow. MPO2 model showed that the increased blood perfusion in PRT (50% more than NRT) significantly elevated the oxygen concentration (57% more than NRT) that the concern from 10% DCE-CT or PCT-S measurement uncertainty (perfusion, f-plasma, SaO₂, Hct) can even be ignored. The real oxygen level difference between NRT and PRT could be higher since the tortuosity difference between two groups is most likely greater than 20%. The montages in figure 6.3.8.1.A-D showed the high heterogeneity in tumor oxygen concentration. We speculate that more negative responding tumors might become the positive responders if intensive narrow

radiation beams are applied only to the highly hypoxic local regions shown on the oxygen map instead of the entire tumor.

7.4 Perspectives in Vessel Normalization

Vessel normalization hypothesis proposed by Dr. Jain provides a sounding explanation to the improved efficacy from the combined therapy (AAT plus RT or AAT plus chemotherapy) by easing off tumor hypoxia; many preclinical and clinical investigations demonstrate the evidences of the normalized vessels, e.g. the increased blood perfusion, decreased plasma volume, reduced interstitial pressure (IFP) in solid tumors, and more. However the detailed normalization mechanisms remain unanswered and required further investigations. For example is there only one mechanism responsible for all tumor vessel structural and functional normalization? Or are there separated driving forces controlling individual aspects of normalization? Does tumor vessel normalization occur heterogeneously? How would this normalization heterogeneity affect the patient survival rate and correlate with tumor hypoxia? Some solid tumors showed the clear structural normalization concomitant with functional normalization; some appeared to suggest that two normalizations were decoupled (e.g. our pancreatic tumor study); some solid tumors did not respond to AAT at all [199, 200]. What are the underlying factors responsible for various normalization outcomes? In this study we used MPO2 as a concept tool to investigate two structure normalization modes—the topological normalization mode to correct tortuosity and the geometrical normalization mode to correct vessel diameter. We found normalizing vessel network tortuosity was more

efficient than normalizing vessel segment diameter. If there was a separated pathway controlling vessel tortuosity normalization, perhaps targeting this mode would yield superior survival rate than targeting the vessel diameter normalization.

Blood perfusion in a vascular network is related to the pressure gradient between the arterial and venous end, the plasma viscosity, and structure resistance of the vessel network. Tortuous tumor vasculature has high structure resistance which contributes to the stagnant blood flow. Hence we would expect structure restored vasculature induced by AAT should lead to the increased blood flow. Ideal vessel normalization should restore most abnormal attributes of tumor microvasculature in a period of time (dilation, tortuosity, decreased blood flow, permeability, e.t.c). In pancreatic tumor the blood perfusion difference between NRT and PRT reached statistical significance, not the fraction of plasma volume. Our theoretical work in comparing the pO₂ improvement from the geometrical and topological normalization suggested that vessel normalization in NRT might correct more the vessel diameter than the vessel tortuosity. The topological normalization was more active than the geometrical normalization in PRT. In other word, more vessel tortuosity in PRT group possibly was normalized than in NRT group. Both NRT and PRT groups had similar vasculature volume reduction after DC101 administration, but less tortuous vessel network in PRT offers reasonable explanation to the increased blood perfusion and oxygen concentration. Idea of arteriole network normalization can provide another route to increase blood flow. Since the arteriole network of microcirculation controls the blood flow rate in the capillary network,

normalizing the abnormal arterioles including restoration of smooth muscle coverage and autoregulation feedback mechanism should improve the blood flow in microcirculation and the subsequent oxygen level in tissue.

Microcirculation composed of arteriole, capillary, and venule network is a complicated and interactive system. We found that restoration of tumor microvasculature seems to involve several modes to normalize various parts of the network and functions. Many investigations showed that the arteriole not only controls the blood flow to capillary network but involves direct oxygen delivery to tissue. The impact to local oxygen concentration from the arteriole network should be at least as dominant as the capillary network. Perhaps there is hierarchy in vessel normalization; ***normalization begins at arteriole network might yield preferred antiangiogenic outcome than normalization starts at capillary network***. Henceforth the capability to further quantify functions and structures for the arteriole network will benefit our understanding in the outcome of antiangiogenic therapy.

7.5 Future Perspectives

Hypoxia is a critical factor in the life of tumor and the cancer therapeutic outcome. Hypoxia is also critical to other disease progression, such as macular degeneration, diabetes retinopathy, chronic kidney and liver fibrosis formation. What is more, we began to realize the pathological significance of hypoxia etiology, distribution, and dynamics in the disease formation and complication to other molecular pathways in

progression. Therefore capability to quantify hypoxia in high fidelity and accuracy will assist to answer those questions and to develop new therapeutic interventions to prevent or to manage the diseases. In this study we proved the validity of our novel approach to quantify tissue pO₂ with *in vivo* functional imaging and mathematical modeling; we also showed the initial success that theoretical MPO₂ prediction agreed with the experimental findings of the antiangiogenic drug on pancreatic xenograft tumors. In this section we proposed four future directions to further improve or extend oxygen transport modeling in hypoxia research.

Animal model. We used Green's function algorithm to evaluate the tissue oxygen profile determined by the structure and function of microcirculation. The detailed vessel structure and function were acquired by inoculating tumor cells in window chamber model. Window chamber model is laborious and technical challenging. The success in the implementation is highly determined by the skill of the surgeon. What is more, the tumors can only grow in the chamber with very limited depth ($< 200\ \mu\text{m}$), which raises the concern how much the tumors in window chambers is relevant to the true subcutaneous tumors on host. Retina is a very transparent tissue in the back of eyes, tumor growing in retina has no limitation in depth and the tumor cell induced vasculature is easily to observe. Tumor cell inoculation in retina provides another animal model to study detailed structure and function of tumor-induced angiogenesis[201, 202].

Accuracy improvement in large voxel size. Simulation showed the excellent correlation existed only voxel size was in range of 50 to 200 μm and deteriorated as voxel size

increased. While this is expected, developing a verified correction formula for voxel size greater than 250 μm can extend this method to *in vivo* functional imaging modalities with lower spatial resolution to estimate hypoxia distribution in tumor.

Measurement of SaO₂ and CtHb. SaO₂, CtHb, and blood flow are highly related to the oxygen concentration in blood as shown in the sensitivity comparison in chapter 4. In pancreatic study, we had structural and hemodynamic parameters from DCE-CT with a reasonable average value of SaO₂ and CtHb in calculation. Tumor vessel is known for heterogeneity in both function and structure. Studies showed identical diameter tumor capillaries can carry diverse RBC flow, which suggested the corresponding SaO₂ and CtHb could fluctuate as well [146, 203, 204]. Hence the accurate measurement of SaO₂ and CtHb are needed in future xenograft tumor experiment to reach more accurate tumor pO₂ prediction.

Development of Dynamic contrast-enhanced 3D photoacoustic imaging. Photoacoustic imaging is an emerging hybrid *in vivo* imaging modality. Dynamic contrast-enhanced 3D photoacoustic imaging (DCE-PCT) will provide most of key vascular physiology in oxygen transport in one experiment. Some preliminary investigation has begun to address the capability and application of this new technology in tumor hypoxia [205-207]. Acute hypoxia has shown correlation to angiogenic treatment efficacy in some solid tumors. The fast scan capability of DCE-PCT will assist to identify short-period acute hypoxia dynamics and its consequence in tumor progression and metastasis.

LIST OF REFERENCES

LIST OF REFERENCES

1. Shannon, A.M., et al., *Tumour hypoxia, chemotherapeutic resistance and hypoxia-related therapies*. *Cancer Treat Rev*, 2003. **29**(4): p. 297-307.
2. Menon, C. and D.L. Fraker, *Tumor oxygenation status as a prognostic marker*. *Cancer Lett*, 2005. **221**(2): p. 225-35.
3. Harrison, L.B., et al., *Impact of tumor hypoxia and anemia on radiation therapy outcomes*. *Oncologist*, 2002. **7**(6): p. 492-508.
4. Brizel, D.M., et al., *Tumor hypoxia adversely affects the prognosis of carcinoma of the head and neck*. *Int J Radiat Oncol Biol Phys*, 1997. **38**(2): p. 285-9.
5. Brizel, D.M., et al., *Tumor oxygenation predicts for the likelihood of distant metastases in human soft tissue sarcoma*. *Cancer Res*, 1996. **56**(5): p. 941-3.
6. Wilson, W.R. and M.P. Hay, *Targeting hypoxia in cancer therapy*. *Nat Rev Cancer*, 2011. **11**(6): p. 393-410.
7. Chiche, J., J.E. Ricci, and J. Pouyssegur, *Tumor hypoxia and metabolism -- towards novel anticancer approaches*. *Ann Endocrinol (Paris)*, 2013. **74**(2): p. 111-4.
8. Coupland, L.A. and C.R. Parish, *Platelets, selectins, and the control of tumor metastasis*. *Semin Oncol*, 2014. **41**(3): p. 422-34.
9. Gilkes, D.M., G.L. Semenza, and D. Wirtz, *Hypoxia and the extracellular matrix: drivers of tumour metastasis*. *Nat Rev Cancer*, 2014. **14**(6): p. 430-9.
10. Vaupel, P. and A. Mayer, *Hypoxia in cancer: significance and impact on clinical outcome*. *Cancer Metastasis Rev*, 2007. **26**(2): p. 225-39.
11. Huang, Y., et al., *Vascular normalizing doses of antiangiogenic treatment reprogram the immunosuppressive tumor microenvironment and enhance immunotherapy*. *Proc Natl Acad Sci U S A*, 2012. **109**(43): p. 17561-6.
12. Vakoc, B.J., et al., *Three-dimensional microscopy of the tumor microenvironment in vivo using optical frequency domain imaging*. *Nat Med*, 2009. **15**(10): p. 1219-23.
13. Jain, R.K., J.D. Martin, and T. Stylianopoulos, *The role of mechanical forces in tumor growth and therapy*. *Annu Rev Biomed Eng*, 2014. **16**: p. 321-46.
14. Emblem, K.E., et al., *Vessel architectural imaging identifies cancer patient responders to anti-angiogenic therapy*. *Nat Med*, 2013. **19**(9): p. 1178-83.
15. Folkman, J., *Angiogenesis: an organizing principle for drug discovery?* *Nat Rev Drug Discov*, 2007. **6**(4): p. 273-86.
16. Folkman, J., *Angiogenesis*. *Annu Rev Med*, 2006. **57**: p. 1-18.
17. Semenza, G.L., *Targeting HIF-1 for cancer therapy*. *Nat Rev Cancer*, 2003. **3**(10): p. 721-32.
18. Semenza, G.L., *Hypoxia, clonal selection, and the role of HIF-1 in tumor progression*. *Crit Rev Biochem Mol Biol*, 2000. **35**(2): p. 71-103.
19. Willett, C.G., et al., *Direct evidence that the VEGF-specific antibody bevacizumab has antivasular effects in human rectal cancer*. *Nat Med*, 2004. **10**(2): p. 145-7.

20. Inai, T., et al., *Inhibition of vascular endothelial growth factor (VEGF) signaling in cancer causes loss of endothelial fenestrations, regression of tumor vessels, and appearance of basement membrane ghosts*. Am J Pathol, 2004. **165**(1): p. 35-52.
21. Graham, C.H., et al., *Hypoxia-mediated stimulation of carcinoma cell invasiveness via upregulation of urokinase receptor expression*. Int J Cancer, 1999. **80**(4): p. 617-23.
22. Giaccia, A.J., *Hypoxic Stress Proteins: Survival of the Fittest*. Semin Radiat Oncol, 1996. **6**(1): p. 46-58.
23. Mattern, J., et al., *Association of resistance-related protein expression with poor vascularization and low levels of oxygen in human rectal cancer*. Int J Cancer, 1996. **67**(1): p. 20-3.
24. Sanna, K. and E.K. Rofstad, *Hypoxia-induced resistance to doxorubicin and methotrexate in human melanoma cell lines in vitro*. Int J Cancer, 1994. **58**(2): p. 258-62.
25. Ausserer, W.A., et al., *Regulation of c-jun expression during hypoxic and low-glucose stress*. Mol Cell Biol, 1994. **14**(8): p. 5032-42.
26. Laderoute, K.R., et al., *Enhanced epidermal growth factor receptor synthesis in human squamous carcinoma cells exposed to low levels of oxygen*. Int J Cancer, 1992. **52**(3): p. 428-32.
27. Takagi, H., et al., *Hypoxia regulates vascular endothelial growth factor receptor KDR/Flk gene expression through adenosine A2 receptors in retinal capillary endothelial cells*. Invest Ophthalmol Vis Sci, 1996. **37**(7): p. 1311-21.
28. Liu, Y., et al., *Hypoxia regulates vascular endothelial growth factor gene expression in endothelial cells. Identification of a 5' enhancer*. Circ Res, 1995. **77**(3): p. 638-43.
29. Forsythe, J.A., et al., *Activation of vascular endothelial growth factor gene transcription by hypoxia-inducible factor 1*. Mol Cell Biol, 1996. **16**(9): p. 4604-13.
30. Sainson, R.C. and A.L. Harris, *Hypoxia-regulated differentiation: let's step it up a Notch*. Trends Mol Med, 2006. **12**(4): p. 141-3.
31. Shi, W. and A.L. Harris, *Notch signaling in breast cancer and tumor angiogenesis: cross-talk and therapeutic potentials*. J Mammary Gland Biol Neoplasia, 2006. **11**(1): p. 41-52.
32. Semenza, G.L. and G.L. Wang, *A nuclear factor induced by hypoxia via de novo protein synthesis binds to the human erythropoietin gene enhancer at a site required for transcriptional activation*. Mol Cell Biol, 1992. **12**(12): p. 5447-54.
33. Jones, N., et al., *Tie receptors: new modulators of angiogenic and lymphangiogenic responses*. Nat Rev Mol Cell Biol, 2001. **2**(4): p. 257-67.
34. Yamakawa, M., et al., *Hypoxia-inducible factor-1 mediates activation of cultured vascular endothelial cells by inducing multiple angiogenic factors*. Circ Res, 2003. **93**(7): p. 664-73.
35. Sanchez-Elsner, T., et al., *A cross-talk between hypoxia and TGF-beta orchestrates erythropoietin gene regulation through SP1 and Smads*. J Mol Biol, 2004. **336**(1): p. 9-24.

36. Schaffer, L., et al., *Oxygen-regulated expression of TGF-beta 3, a growth factor involved in trophoblast differentiation*. Placenta, 2003. **24**(10): p. 941-50.
37. Folkman, J., *Tumor angiogenesis: therapeutic implications*. N Engl J Med, 1971. **285**(21): p. 1182-6.
38. Folkman, J., et al., *Isolation of a tumor factor responsible for angiogenesis*. J Exp Med, 1971. **133**(2): p. 275-88.
39. Clarke, J.M. and H.I. Hurwitz, *Understanding and targeting resistance to anti-angiogenic therapies*. J Gastrointest Oncol, 2013. **4**(3): p. 253-63.
40. Yang, J.C., et al., *A randomized trial of bevacizumab, an anti-vascular endothelial growth factor antibody, for metastatic renal cancer*. N Engl J Med, 2003. **349**(5): p. 427-34.
41. Cobleigh, M.A., et al., *A phase I/II dose-escalation trial of bevacizumab in previously treated metastatic breast cancer*. Seminars in Oncology, 2003. **30**, **Supplement 16**(0): p. 117-124.
42. Mayer, R.J., *Two Steps Forward in the Treatment of Colorectal Cancer*. New England Journal of Medicine, 2004. **350**(23): p. 2406-2408.
43. Tong, R.T., et al., *Vascular normalization by vascular endothelial growth factor receptor 2 blockade induces a pressure gradient across the vasculature and improves drug penetration in tumors*. Cancer Res, 2004. **64**(11): p. 3731-6.
44. Jain, R.K., *Normalizing tumor vasculature with anti-angiogenic therapy: a new paradigm for combination therapy*. Nat Med, 2001. **7**(9): p. 987-9.
45. Senger, D.R., et al., *Tumor cells secrete a vascular permeability factor that promotes accumulation of ascites fluid*. Science, 1983. **219**(4587): p. 983-5.
46. Ferrara, N. and W.J. Henzel, *Pituitary follicular cells secrete a novel heparin-binding growth factor specific for vascular endothelial cells*. Biochem Biophys Res Commun, 1989. **161**(2): p. 851-8.
47. Shweiki, D., et al., *Vascular endothelial growth factor induced by hypoxia may mediate hypoxia-initiated angiogenesis*. Nature, 1992. **359**(6398): p. 843-5.
48. Plate, K.H., et al., *Vascular endothelial growth factor is a potential tumour angiogenesis factor in human gliomas in vivo*. Nature, 1992. **359**(6398): p. 845-8.
49. de Vries, C., et al., *The fms-like tyrosine kinase, a receptor for vascular endothelial growth factor*. Science, 1992. **255**(5047): p. 989-91.
50. Terman, B.I., et al., *Identification of the KDR tyrosine kinase as a receptor for vascular endothelial cell growth factor*. Biochem Biophys Res Commun, 1992. **187**(3): p. 1579-86.
51. Qi, W.X., et al., *Bevacizumab increases the risk of infections in cancer patients: A systematic review and pooled analysis of 41 randomized controlled trials*. Crit Rev Oncol Hematol, 2015.
52. Dedania, V.S. and S.J. Bakri, *Current perspectives on ranibizumab*. Clin Ophthalmol, 2015. **9**: p. 533-42.
53. Larsen, P.B., I. Kumler, and D.L. Nielsen, *A systematic review of trastuzumab and lapatinib in the treatment of women with brain metastases from HER2-positive breast cancer*. Cancer Treat Rev, 2013. **39**(7): p. 720-7.

54. Santoni, M., et al., *Treatment-related fatigue with sorafenib, sunitinib and pazopanib in patients with advanced solid tumors: an up-to-date review and meta-analysis of clinical trials*. Int J Cancer, 2015. **136**(1): p. 1-10.
55. Smolle, E., et al., *Targeted treatment of ovarian cancer--the multiple - kinase - inhibitor sorafenib as a potential option*. Anticancer Res, 2014. **34**(4): p. 1519-30.
56. Ichihara, E., K. Kiura, and M. Tanimoto, *Targeting angiogenesis in cancer therapy*. Acta Med Okayama, 2011. **65**(6): p. 353-62.
57. Sakurai, T. and M. Kudo, *Signaling pathways governing tumor angiogenesis*. Oncology, 2011. **81 Suppl 1**: p. 24-9.
58. Hurwitz, H., et al., *Bevacizumab plus Irinotecan, Fluorouracil, and Leucovorin for Metastatic Colorectal Cancer*. New England Journal of Medicine, 2004. **350**(23): p. 2335-2342.
59. Eskander, R.N. and L.M. Randall, *Bevacizumab in the treatment of ovarian cancer*. Biologics, 2011. **5**: p. 1-5.
60. Gorski, D.H., et al., *Potentiation of the Antitumor Effect of Ionizing Radiation by Brief Concomitant Exposures to Angiostatin*. Cancer Research, 1998. **58**(24): p. 5686-5689.
61. Mauceri, H.J., et al., *Combined effects of angiostatin and ionizing radiation in antitumour therapy*. Nature, 1998. **394**(6690): p. 287-291.
62. Thomlinson, R.H. and L.H. Gray, *The histological structure of some human lung cancers and the possible implications for radiotherapy*. Br J Cancer, 1955. **9**(4): p. 539-49.
63. Gray, L.H., et al., *The concentration of oxygen dissolved in tissues at the time of irradiation as a factor in radiotherapy*. Br J Radiol, 1953. **26**(312): p. 638-48.
64. Yuan, F., et al., *Time-dependent vascular regression and permeability changes in established human tumor xenografts induced by an anti-vascular endothelial growth factor/vascular permeability factor antibody*. Proc Natl Acad Sci U S A, 1996. **93**(25): p. 14765-70.
65. Hansen-Algenstaedt, N., et al., *Tumor Oxygenation in Hormone-Dependent Tumors During Vascular Endothelial Growth Factor Receptor-2 Blockade, Hormone Ablation, and Chemotherapy*. Cancer Research, 2000. **60**(16): p. 4556-4560.
66. Tong, R.T., et al., *Vascular Normalization by Vascular Endothelial Growth Factor Receptor 2 Blockade Induces a Pressure Gradient Across the Vasculature and Improves Drug Penetration in Tumors*. Cancer Research, 2004. **64**(11): p. 3731-3736.
67. Winkler, F., et al., *Kinetics of vascular normalization by VEGFR2 blockade governs brain tumor response to radiation: role of oxygenation, angiopoietin-1, and matrix metalloproteinases*. Cancer Cell, 2004. **6**(6): p. 553-63.
68. Vakoc, B.J., et al., *Three-dimensional microscopy of the tumor microenvironment in vivo using optical frequency domain imaging*. Nat Med, 2009. **15**(10): p. 1219-1223.

69. Willett, C.G., et al., *Surrogate Markers for Antiangiogenic Therapy and Dose-Limiting Toxicities for Bevacizumab With Radiation and Chemotherapy: Continued Experience of a Phase I Trial in Rectal Cancer Patients*. Journal of Clinical Oncology, 2005. **23**(31): p. 8136-8139.
70. Batchelor, T.T., et al., *AZD2171, a pan-VEGF receptor tyrosine kinase inhibitor, normalizes tumor vasculature and alleviates edema in glioblastoma patients*. Cancer Cell, 2007. **11**(1): p. 83-95.
71. Jain, R.K., *Normalization of tumor vasculature: an emerging concept in antiangiogenic therapy*. Science, 2005. **307**(5706): p. 58-62.
72. Izumi, Y., et al., *Tumour biology: herceptin acts as an anti-angiogenic cocktail*. Nature, 2002. **416**(6878): p. 279-80.
73. Qayum, N., et al., *Tumor vascular changes mediated by inhibition of oncogenic signaling*. Cancer Res, 2009. **69**(15): p. 6347-54.
74. Cao, N., et al., *Monitoring the effects of anti-angiogenesis on the radiation sensitivity of pancreatic cancer xenografts using dynamic contrast-enhanced computed tomography*. Int J Radiat Oncol Biol Phys, 2014. **88**(2): p. 412-8.
75. Batchelor, T.T., et al., *Phase II study of cediranib, an oral pan-vascular endothelial growth factor receptor tyrosine kinase inhibitor, in patients with recurrent glioblastoma*. J Clin Oncol, 2010. **28**(17): p. 2817-23.
76. Fischer, I., et al., *High-grade glioma before and after treatment with radiation and Avastin: initial observations*. Neuro Oncol, 2008. **10**(5): p. 700-8.
77. Benjamin, L.E., et al., *Selective ablation of immature blood vessels in established human tumors follows vascular endothelial growth factor withdrawal*. J Clin Invest, 1999. **103**(2): p. 159-65.
78. Bullitt, E., et al., *Blood vessel morphologic changes depicted with MR angiography during treatment of brain metastases: a feasibility study*. Radiology, 2007. **245**(3): p. 824-30.
79. Hockel, M., et al., *Oxygenation of carcinomas of the uterine cervix: evaluation by computerized O₂ tension measurements*. Cancer Res, 1991. **51**(22): p. 6098-102.
80. Vaupel, P., et al., *Oxygenation of human tumors: evaluation of tissue oxygen distribution in breast cancers by computerized O₂ tension measurements*. Cancer Res, 1991. **51**(12): p. 3316-22.
81. Chitneni, S.K., et al., *Molecular imaging of hypoxia*. J Nucl Med, 2011. **52**(2): p. 165-8.
82. Krohn, K.A., J.M. Link, and R.P. Mason, *Molecular imaging of hypoxia*. J Nucl Med, 2008. **49 Suppl 2**: p. 129S-48S.
83. Young, W.K., B. Vojnovic, and P. Wardman, *Measurement of oxygen tension in tumours by time-resolved fluorescence*. Br J Cancer Suppl, 1996. **27**: p. S256-9.
84. Collingridge, D.R., et al., *Measurement of tumor oxygenation: a comparison between polarographic needle electrodes and a time-resolved luminescence-based optical sensor*. Radiat Res, 1997. **147**(3): p. 329-34.

85. Braun, R.D., et al., *Comparison of tumor and normal tissue oxygen tension measurements using OxyLite or microelectrodes in rodents*. Am J Physiol Heart Circ Physiol, 2001. **280**(6): p. H2533-44.
86. Wen, B., et al., *Comparison of Helzel and OxyLite systems in the measurements of tumor partial oxygen pressure (pO₂)*. Radiat Res, 2008. **169**(1): p. 67-75.
87. Kaanders, J.H., et al., *Pimonidazole binding and tumor vascularity predict for treatment outcome in head and neck cancer*. Cancer Res, 2002. **62**(23): p. 7066-74.
88. Evans, S.M., et al., *Patterns and levels of hypoxia in head and neck squamous cell carcinomas and their relationship to patient outcome*. Int J Radiat Oncol Biol Phys, 2007. **69**(4): p. 1024-31.
89. Nordsmark, M., et al., *Measurements of hypoxia using pimonidazole and polarographic oxygen-sensitive electrodes in human cervix carcinomas*. Radiother Oncol, 2003. **67**(1): p. 35-44.
90. Evans, S.M., et al., *Comparative measurements of hypoxia in human brain tumors using needle electrodes and EF5 binding*. Cancer Res, 2004. **64**(5): p. 1886-92.
91. Sorensen, B.S., et al., *Hypoxia induced expression of endogenous markers in vitro is highly influenced by pH*. Radiother Oncol, 2007. **83**(3): p. 362-6.
92. Airley, R., et al., *Glucose transporter glut-1 expression correlates with tumor hypoxia and predicts metastasis-free survival in advanced carcinoma of the cervix*. Clin Cancer Res, 2001. **7**(4): p. 928-34.
93. Koh-ichi Sakata MD, M.S., Hisayasu Nagakura, Kensei Nakata, Atushi Oouchi, Masato Hareyama, Masaaki Satoh, *A Clinical Study of Hypoxia Using Endogenous Hypoxic Markers and Polarographic Oxygen Electrodes*. Strahlentherapie und Onkologie, 2006. **182**(9): p. 511-517.
94. Fontanella, A.N., et al., *Quantitative mapping of hemodynamics in the lung, brain, and dorsal window chamber-grown tumors using a novel, automated algorithm*. Microcirculation, 2013.
95. Dewhirst, M.W., et al., *Review of methods used to study oxygen transport at the microcirculatory level*. Int J Cancer, 2000. **90**(5): p. 237-55.
96. Raleigh, J.A., M.W. Dewhirst, and D.E. Thrall, *Measuring Tumor Hypoxia*. Semin Radiat Oncol, 1996. **6**(1): p. 37-45.
97. Lee, S.T. and A.M. Scott, *Hypoxia positron emission tomography imaging with 18f-fluoromisonidazole*. Semin Nucl Med, 2007. **37**(6): p. 451-61.
98. Grunbaum, Z., et al., *Synthesis and characterization of congeners of misonidazole for imaging hypoxia*. J Nucl Med, 1987. **28**(1): p. 68-75.
99. Martin, G.V., et al., *Noninvasive detection of hypoxic myocardium using fluorine-18-fluoromisonidazole and positron emission tomography*. J Nucl Med, 1992. **33**(12): p. 2202-8.
100. Bhujwala, Z.M., et al., *Reduction of vascular and permeable regions in solid tumors detected by macromolecular contrast magnetic resonance imaging after treatment with antiangiogenic agent TNP-470*. Clin Cancer Res, 2003. **9**(1): p. 355-62.

101. Bandettini, P.A., *The Spatial, Temporal, And Interpretive Limits OF Functional MRI*, in *Neuropsychopharmacology: The Firth Generation of Progress*, K.C.D.C.J.T.N.C. Davis, Editor. 2002, Lippincott Williams & Wilkins: Philadelphia, PA.
102. Thulborn, K.R., et al., *Oxygenation dependence of the transverse relaxation time of water protons in whole blood at high field*. *Biochim Biophys Acta*, 1982. **714**(2): p. 265-70.
103. Baudelet, C. and B. Gallez, *How does blood oxygen level-dependent (BOLD) contrast correlate with oxygen partial pressure (pO₂) inside tumors?* *Magnetic Resonance in Medicine*, 2002. **48**(6): p. 980-986.
104. Baudelet C., G.B., *Current Issues in the Utility of Blood Oxygen Level Dependent MRI for the Assessment of Modulations in Tumor Oxygenation*. *Current Medical Imaging Reviews*, 2005. **1**(3): p. 229-243.
105. Bandettini, P.A., *Functional MRI (Medical Radiology / Diagnostic Imaging)*, ed. P.A.B. C.T.W. Moonen. 2000: Springer. 587.
106. Mason, R.P., et al., *Non-invasive determination of tumor oxygen tension and local variation with growth*. *Int J Radiat Oncol Biol Phys*, 1994. **29**(1): p. 95-103.
107. Mason, R.P., et al., *Tumor oximetry: comparison of 19F MR EPI and electrodes*. *Adv Exp Med Biol*, 2003. **530**: p. 19-27.
108. Zhao, D., et al., *Tumor oxygen dynamics: correlation of in vivo MRI with histological findings*. *Neoplasia*, 2003. **5**(4): p. 308-18.
109. Delpuecha), J.-J., et al., *Fluorocarbons as oxygen carriers. I. An NMR study of oxygen solutions in hexafluorobenzene*. *The Journal of Chemical Physics*, 1979. **70**(6): p. 2680-2687.
110. Hamza, M.H.A., et al., *Solute-solvent interactions in perfluorocarbon solutions of oxygen. An NMR study*. *Journal of the American Chemical Society*, 1981. **103**(13): p. 3733-3738.
111. Yalowitz, J.A., et al., *Cytotoxicity and cellular differentiation activity of methylenebis(phosphonate) analogs of tiazofurin and mycophenolic acid adenine dinucleotide in human cancer cell lines*. *Cancer Lett*, 2002. **181**(1): p. 31-8.
112. Jayaram, H.N., et al., *Toxicity and efficacy of benzamide riboside in cancer chemotherapy models*. *Curr Med Chem*, 2002. **9**(7): p. 787-92.
113. Oku, T., et al., *Tumor growth modulation by sense and antisense vascular endothelial growth factor gene expression: effects on angiogenesis, vascular permeability, blood volume, blood flow, fluorodeoxyglucose uptake, and proliferation of human melanoma intracerebral xenografts*. *Cancer Res*, 1998. **58**(18): p. 4185-92.
114. Bowen, T.N., L.; Pifer, AE; Sembrosk, GH, *Some experimental results on the thermoacoustic imaging of soft tissue-equivalent phantoms*. *PROC IEEE Ultrason Symp.*, 1981. **2**: p. 823-827.
115. Bowen, T., *Radiation-induced thermoacoustic soft tissue imaging*. *PROC IEEE Ultrason Symp.*, 1981. **2**: p. 817-822.
116. Kruger, R.A., et al., *Thermoacoustic molecular imaging of small animals*. *Mol Imaging*, 2003. **2**(2): p. 113-23.

117. Cairns, R.A. and R.P. Hill, *Acute hypoxia enhances spontaneous lymph node metastasis in an orthotopic murine model of human cervical carcinoma*. Cancer Res, 2004. **64**(6): p. 2054-61.
118. Kimura, H., et al., *Fluctuations in red cell flux in tumor microvessels can lead to transient hypoxia and reoxygenation in tumor parenchyma*. Cancer Res, 1996. **56**(23): p. 5522-8.
119. Haakma, W., et al., *Belief elicitation to populate health economic models of medical diagnostic devices in development*. Appl Health Econ Health Policy, 2014. **12**(3): p. 327-34.
120. Menke, J., *Photoacoustic breast tomography prototypes with reported human applications*. Eur Radiol, 2015.
121. Axel, L., *Cerebral blood flow determination by rapid-sequence computed tomography: theoretical analysis*. Radiology, 1980. **137**(3): p. 679-86.
122. Sourbron, S., *Technical aspects of MR perfusion*. Eur J Radiol, 2010. **76**(3): p. 304-13.
123. Greis, C., *Quantitative evaluation of microvascular blood flow by contrast-enhanced ultrasound (CEUS)*. Clin Hemorheol Microcirc, 2011. **49**(1-4): p. 137-49.
124. Williams, R., et al., *Dynamic microbubble contrast-enhanced US to measure tumor response to targeted therapy: a proposed clinical protocol with results from renal cell carcinoma patients receiving antiangiogenic therapy*. Radiology, 2011. **260**(2): p. 581-90.
125. Ito, H., et al., *Database of normal human cerebral blood flow measured by SPECT: I. Comparison between I-123-IMP, Tc-99m-HMPAO, and Tc-99m-ECD as referred with O-15 labeled water PET and voxel-based morphometry*. Ann Nucl Med, 2006. **20**(2): p. 131-8.
126. Cao, M., *Quantification of Intra-tumor Physiological Heterogeneity and Therapeutic Response in Xenograft MCF-7 Breast Tumor Models by Dynamic Contrast Enhanced Computed Tomography*, in School of Health Sciences. 2007, Purdue University.
127. Cao, M., et al., *Developing DCE-CT to quantify intra-tumor heterogeneity in breast tumors with differing angiogenic phenotype*. IEEE Trans Med Imaging, 2009. **28**(6): p. 861-71.
128. Krishnamurthi, G., et al., *Functional imaging in small animals using X-ray computed tomography--study of physiologic measurement reproducibility*. IEEE Trans Med Imaging, 2005. **24**(7): p. 832-43.
129. Stantz, K.M., et al., *Monitoring the longitudinal intra-tumor physiological impulse response to VEGFR2 blockade in breast tumors using DCE-CT*. Mol Imaging Biol, 2011. **13**(6): p. 1183-95.
130. Levick, R., *An introduction to cardiovascular physiology*. 2009: CRC Press. 432.
131. Sherwood, L., *Human Physiology: From Cells to Systems*. 2012: Cengage Learning.
132. Krogh, A., *The rate of diffusion of gases through animal tissues, with some remarks on the coefficient of invasion*. J Physiol, 1919. **52**(6): p. 391-408.

133. Krogh, A., *The number and distribution of capillaries in muscles with calculations of the oxygen pressure head necessary for supplying the tissue*. J Physiol, 1919. **52**(6): p. 409-15.
134. Arthur C. Guyton, J.E.H., *Textbook of Medical Physiology*. 2006: Elsevier Saunders.
135. Fournier, R.L., *Basic Transport Phenomena in Biomedical Engineering*. 3rd ed. 2011: CRC Press.
136. Duling, B.R. and R.M. Berne, *Longitudinal gradients in periarteriolar oxygen tension. A possible mechanism for the participation of oxygen in local regulation of blood flow*. Circ Res, 1970. **27**(5): p. 669-78.
137. Duling, B.R., W. Kuschinsky, and M. Wahl, *Measurements of the perivascular PO₂ in the vicinity of the pial vessels of the cat*. Pflugers Arch, 1979. **383**(1): p. 29-34.
138. Ivanov, K.P., et al., *Direct measurements of oxygen tension at the surface of arterioles, capillaries and venules of the cerebral cortex*. Pflugers Arch, 1982. **393**(1): p. 118-20.
139. Pittman, R.N., *Oxygen gradients in the microcirculation*. Acta Physiol (Oxf), 2011. **202**(3): p. 311-22.
140. Golub, A.S., M.A. Tevald, and R.N. Pittman, *Phosphorescence quenching microrespirometry of skeletal muscle in situ*. Am J Physiol Heart Circ Physiol, 2011. **300**(1): p. H135-43.
141. Tsai, A.G., P. Cabrales, and M. Intaglietta, *The physics of oxygen delivery: facts and controversies*. Antioxid Redox Signal, 2010. **12**(6): p. 683-91.
142. Tsai, A.G., P.C. Johnson, and M. Intaglietta, *Is the distribution of tissue pO₂ homogeneous?* Antioxid Redox Signal, 2007. **9**(7): p. 979-84.
143. Algire, G.H., *An Adaptation of the Transparent-Chamber Technique to the Mouse*. Journal of the National Cancer Institute, 1943. **4**(1): p. 1-11.
144. Papenfuss, H.D., et al., *A transparent access chamber for the rat dorsal skin fold*. Microvasc Res, 1979. **18**(3): p. 311-8.
145. Asaishi, K., et al., *Quantitative analysis of microvascular structure and function in the amelanotic melanoma A-Mel-3*. Cancer Res, 1981. **41**(5): p. 1898-904.
146. Leunig, M., et al., *Angiogenesis, microvascular architecture, microhemodynamics, and interstitial fluid pressure during early growth of human adenocarcinoma LS174T in SCID mice*. Cancer Res, 1992. **52**(23): p. 6553-60.
147. Helmlinger, G., et al., *Interstitial pH and pO₂ gradients in solid tumors in vivo: high-resolution measurements reveal a lack of correlation*. Nat Med, 1997. **3**(2): p. 177-82.
148. Huang, Q., et al., *Noninvasive visualization of tumors in rodent dorsal skin window chambers*. Nat Biotechnol, 1999. **17**(10): p. 1033-5.
149. Dewhirst, M.W., et al., *Quantification of longitudinal tissue pO₂ gradients in window chamber tumours: impact on tumour hypoxia*. Br J Cancer, 1999. **79**(11-12): p. 1717-22.
150. Palmer, G.M., et al., *Optical imaging of tumor hypoxia dynamics*. J Biomed Opt, 2010. **15**(6): p. 066021.

151. Giuvarasteanu, I., *Scanning electron microscopy of vascular corrosion casts--standard method for studying microvessels*. Rom J Morphol Embryol, 2007. **48**(3): p. 257-61.
152. Konerding, M.A., A.J. Miodonski, and A. Lametschwandtner, *Microvascular corrosion casting in the study of tumor vascularity: a review*. Scanning Microsc, 1995. **9**(4): p. 1233-43; discussion 1243-4.
153. Secomb, T.W., et al., *Theoretical simulation of oxygen transport to tumors by three-dimensional networks of microvessels*. Adv Exp Med Biol, 1998. **454**: p. 629-34.
154. Fukumura, D., et al., *Tumor microvasculature and microenvironment: novel insights through intravital imaging in pre-clinical models*. Microcirculation, 2010. **17**(3): p. 206-25.
155. Potter, S.M., *Vital imaging: two photons are better than one*. Curr Biol, 1996. **6**(12): p. 1595-8.
156. Cox, P.G. and N. Jeffery, *Reviewing the morphology of the jaw-closing musculature in squirrels, rats, and guinea pigs with contrast-enhanced microCT*. Anat Rec (Hoboken), 2011. **294**(6): p. 915-28.
157. Kiessling, F., D. Razansky, and F. Alves, *Anatomical and microstructural imaging of angiogenesis*. Eur J Nucl Med Mol Imaging, 2010. **37 Suppl 1**: p. S4-19.
158. Wayland, H. and P.C. Johnson, *Erythrocyte velocity measurement in microvessels by a two-slit photometric method*. J Appl Physiol, 1967. **22**(2): p. 333-7.
159. Intaglietta, M., N.R. Silverman, and W.R. Tompkins, *Capillary flow velocity measurements in vivo and in situ by television methods*. Microvasc Res, 1975. **10**(2): p. 165-79.
160. Unthank, J.L., et al., *Evaluation of carbocyanine-labeled erythrocytes for microvascular measurements*. Microvasc Res, 1993. **45**(2): p. 193-210.
161. Brizel, D.M., et al., *A comparison of tumor and normal tissue microvascular hematocrits and red cell fluxes in a rat window chamber model*. Int J Radiat Oncol Biol Phys, 1993. **25**(2): p. 269-76.
162. Jain, R.K., *Determinants of tumor blood flow: a review*. Cancer Res, 1988. **48**(10): p. 2641-58.
163. Vanderkooi, J.M., et al., *An optical method for measurement of dioxygen concentration based upon quenching of phosphorescence*. J Biol Chem, 1987. **262**(12): p. 5476-82.
164. Wilson, D.F., et al., *Monitoring the dynamics of tissue oxygenation in vivo by phosphorescence quenching*. Adv Exp Med Biol, 2003. **540**: p. 1-5.
165. Vinogradov, S.A., et al., *Oxygen distributions in tissue measured by phosphorescence quenching*. Adv Exp Med Biol, 2003. **510**: p. 181-5.
166. Torres Filho, I.P., et al., *Noninvasive measurement of microvascular and interstitial oxygen profiles in a human tumor in SCID mice*. Proc Natl Acad Sci U S A, 1994. **91**(6): p. 2081-5.

167. Shibata, M., et al., *Microvascular and interstitial PO₂ measurements in rat skeletal muscle by phosphorescence quenching*. J Appl Physiol (1985), 2001. **91**(1): p. 321-7.
168. Buerk, D.G., *Measuring tissue PO₂ with microelectrodes*. Methods Enzymol, 2004. **381**: p. 665-90.
169. Whalen, W.J., J. Riley, and P. Nair, *A microelectrode for measuring intracellular PO₂*. J Appl Physiol, 1967. **23**(5): p. 798-801.
170. Whalen, W.J. and P. Nair, *Intracellular PO₂ and its regulation in resting skeletal muscle of the guinea pig*. Circ Res, 1967. **21**(3): p. 251-61.
171. Vinogradov, S.A., et al., *Noninvasive imaging of the distribution in oxygen in tissue in vivo using near-infrared phosphors*. Biophys J, 1996. **70**(4): p. 1609-17.
172. Dunphy, I., S.A. Vinogradov, and D.F. Wilson, *Oxyphor R2 and G2: phosphors for measuring oxygen by oxygen-dependent quenching of phosphorescence*. Anal Biochem, 2002. **310**(2): p. 191-8.
173. Pittman, R.N. and B.R. Duling, *Measurement of percent oxyhemoglobin in the microvasculature*. J Appl Physiol, 1975. **38**(2): p. 321-7.
174. Pittman, R.N. and B.R. Duling, *A new method for the measurement of percent oxyhemoglobin*. J Appl Physiol, 1975. **38**(2): p. 315-20.
175. Pittman, R.N., *In vivo photometric analysis of hemoglobin*. Ann Biomed Eng, 1986. **14**(2): p. 119-37.
176. Torres Filho, I.P., et al., *Measurement of hemoglobin oxygen saturation using Raman microspectroscopy and 532-nm excitation*. J Appl Physiol (1985), 2008. **104**(6): p. 1809-17.
177. Ward, K.R., et al., *Resonance Raman spectroscopy: a new technology for tissue oxygenation monitoring*. Crit Care Med, 2006. **34**(3): p. 792-9.
178. Lanzen, J., et al., *Direct demonstration of instabilities in oxygen concentrations within the extravascular compartment of an experimental tumor*. Cancer Res, 2006. **66**(4): p. 2219-23.
179. Hellums, J.D., *The resistance to oxygen transport in the capillaries relative to that in the surrounding tissue*. Microvasc Res, 1977. **13**(1): p. 131-6.
180. Kellogg, O.D., *Foundations of Potential Theory*. 2010.
181. Weiss, R., *Parameter-Free Iterative Linear Solvers*. 1996, Berlin: Akademie Verlag GmbH.
182. Vaupel, P., et al., *Blood flow, oxygen consumption, and tissue oxygenation of human breast cancer xenografts in nude rats*. Cancer Res, 1987. **47**(13): p. 3496-503.
183. Grote, J., R. Susskind, and P. Vaupel, *Oxygen diffusivity in tumor tissue (DS-carcinosarcoma) under temperature conditions within the range of 20--40 degrees C*. Pflugers Arch, 1977. **372**(1): p. 37-42.
184. Zander, R., *Cellular oxygen concentration*. Adv Exp Med Biol, 1975. **75**: p. 463-467.
185. Mouton, P.R., *Unbiased Stereology*. 2011: The Johns Hopkins University Press.
186. Secomb, T.W., *Microvascular Network Structure*. 2010: University of Arizona.

187. Lubbers, D.W., *Oxygen electrodes and optodes and their application in vivo*. Adv Exp Med Biol, 1996. **388**: p. 13-34.
188. Ragheb, J. and D.J. Buggy, *Editorial III: Tissue oxygen tension (PTO₂) in anaesthesia and perioperative medicine*. Br J Anaesth, 2004. **92**(4): p. 464-8.
189. Tian, W., et al., *Singlet oxygen phosphorescence lifetime imaging based on a fluorescence lifetime imaging microscope*. J Phys Chem A, 2015. **119**(14): p. 3393-9.
190. Griffiths, J.R. and S.P. Robinson, *The OxyLite: a fibre-optic oxygen sensor*. Br J Radiol, 1999. **72**(859): p. 627-30.
191. Shaw, A.D., et al., *Assessment of tissue oxygen tension: comparison of dynamic fluorescence quenching and polarographic electrode technique*. Crit Care, 2002. **6**(1): p. 76-80.
192. Stantz, K., et al., *Imaging the Progression of Intra-tumor Heterogeneity in Prostate and Ovarian Xenografts Using Dynamic Contrast-Enhanced CT*. Conf Proc IEEE Eng Med Biol Soc, 2005. **2**(1): p. 1883-1886.
193. Koido, S., et al., *Current immunotherapeutic approaches in pancreatic cancer*. Clin Dev Immunol, 2011. **2011**: p. 267539.
194. Nakahira, S., et al., *Involvement of ribonucleotide reductase M1 subunit overexpression in gemcitabine resistance of human pancreatic cancer*. Int J Cancer, 2007. **120**(6): p. 1355-63.
195. Rofstad, E.K., et al., *Tumors exposed to acute cyclic hypoxic stress show enhanced angiogenesis, perfusion and metastatic dissemination*. Int J Cancer, 2010. **127**(7): p. 1535-46.
196. Rofstad, E.K., et al., *Fluctuating and diffusion-limited hypoxia in hypoxia-induced metastasis*. Clin Cancer Res, 2007. **13**(7): p. 1971-8.
197. Rofstad, E.K. and K. Maseide, *Radiobiological and immunohistochemical assessment of hypoxia in human melanoma xenografts: acute and chronic hypoxia in individual tumours*. Int J Radiat Biol, 1999. **75**(11): p. 1377-93.
198. Dewhirst, M.W., et al., *Determination of local oxygen consumption rates in tumors*. Cancer Res, 1994. **54**(13): p. 3333-6.
199. Koukourakis, M.I., et al., *Endogenous markers of two separate hypoxia response pathways (hypoxia inducible factor 2 alpha and carbonic anhydrase 9) are associated with radiotherapy failure in head and neck cancer patients recruited in the CHART randomized trial*. J Clin Oncol, 2006. **24**(5): p. 727-35.
200. Yan, M., et al., *BRCA1 tumours correlate with a HIF-1alpha phenotype and have a poor prognosis through modulation of hydroxylase enzyme profile expression*. Br J Cancer, 2009. **101**(7): p. 1168-74.
201. Kent, D.L., *Age-related macular degeneration: beyond anti-angiogenesis*. Mol Vis, 2014. **20**: p. 46-55.
202. Siemerink, M.J., et al., *Endothelial tip cells in ocular angiogenesis: potential target for anti-angiogenesis therapy*. J Histochem Cytochem, 2013. **61**(2): p. 101-15.

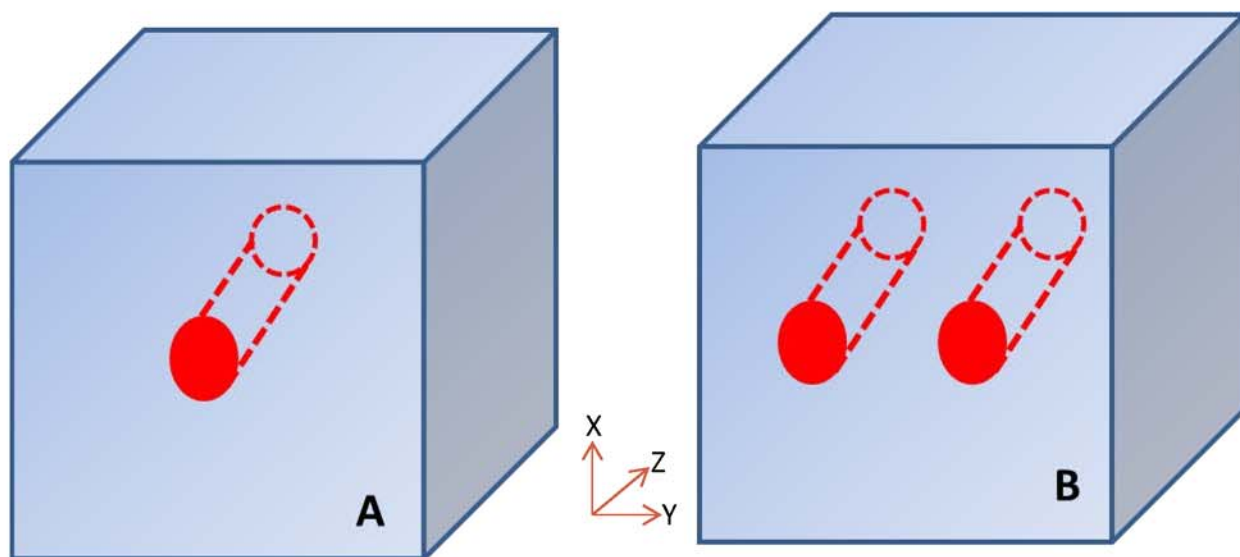
- 203. Less, J.R., et al., *Microvascular architecture in a mammary carcinoma: branching patterns and vessel dimensions*. Cancer Res, 1991. **51**(1): p. 265-73.
- 204. Kamoun, W.S., et al., *Simultaneous measurement of RBC velocity, flux, hematocrit and shear rate in vascular networks*. Nat Methods, 2010. **7**(8): p. 655-60.
- 205. Olafsson, R., et al., *Real-time, contrast enhanced photoacoustic imaging of cancer in a mouse window chamber*. Opt Express, 2010. **18**(18): p. 18625-32.
- 206. Stantz, K., *Imaging hypoxia using 3D photoacoustic spectroscopy*. Proc. of SPIE, 2010. **7564**.
- 207. Wang, P.K., I.; Carson, J.L, *Dynamic contrast-enhanced 3D photoacoustic imaging*. Proc. of SPIE, 2013. **8581**.

APPENDIX

APPENDIX

Multi-Vessels MPO2 Modeling

Multi-vessels MPO2 model is the modification of single vessel MPO2 model. The procedures of obtaining voxel vascular inputs (fraction of vessel volume, blood perfusion, hct, and SaO₂) are identical. Single vessel model evaluates the pO₂ in a voxel by placing the vessel at the center of the voxel; multi vessels are distributed symmetrically in the voxel (see figure A). In multi-vessels model, the total vessel volume and blood perfusion are equally divided into the multi-vessels. For instance, in a two-vessels model each vessel blood perfusion is half of the total voxel blood perfusion; each vessel volume is half of the total vascular volume. SaO₂ and concentration of hemoglobin of each vessel remain unchanged as the total voxel SaO₂ and hemoglobin concentration. The pO₂ at any point inside voxel is the superposition from each individual vessel.



VITA

VITA

Chung-Wein Lee

Division of Medical Physics

School of Health Sciences

Purdue University

West Lafayette, Indiana, 47907

Education

B.S., Physics, Soochow University, Taipei, Taiwan

M.S., BioPhysics, Indiana University, Bloomington, Indiana, USA

Ph.D candidate, Medical Physics, Purdue University, West Lafayette, Indiana, USA

Professional experience

2011 to current Scientist III, Boehringer Ingelheim Pharmaceuticals, Ridgefield CT

2008 to 2010 Research Associate, Covance, Greenfield IN

2004 to 2008 Computational Biologist, Eli Lilly and Company, Greenfield IN

Publications

Book chapter

Using gene-pair differential expression to access relative contributions of biological processes in defining disease phenotype, *A Practical Guide to Bioinformatics Analysis*, 2010

Journal

- **Multispectral IHC imaging application on chronic kidney disease drug discovery**, Chung-Wein Lee, Glenn Gibson, Sun Peng, Stephen M. Weldon, Glenn Reinhart, HuSheng Qian, ASPET 2015
- **Quantification of Renal Intersitial Fibrosis by Second Harmonic Imaging in Rat Kidney Tissue sections**, HuSheng Qian, Damian Matera, Chung-Wein Lee, Stephen M. Weldon, Agnes Fogo, Glenn Reinhart (submission), 2015
- **Circulating markers reflect both anti- and pro-atherogenic drug effects in ApoE-deficient mice**, Birong Liao, Eileen McCall, Karen Cox, Chung-Wein Lee, Shuguang Huang, Richard E Higgs, Frank Lawrence, Steven Zuckerman, Li-Chun Chio, Yuejun Zheng, John E Hale, Xiao-di Huang, Donetta Gifford-Moore, Kwan Hui, Kevin Duffin, Kenneth E Gould, Mark Reikhter, Biomarker Insights 2008:3 147-157
- **Identification of Phenotype-Defining Gene Signatures Using the Gene-Pair Matrix Based Clustering**, Chung-Wein Lee, Shuyu Li, Eric W. Su, Birong Liao, *Lecture Notes in Bioinformatics* 4316, 106-119.
- **Development of an imaging analysis method for counting micro vessels in angiogenesis research**, Chung-Wein Lee, Xiaoling Xia, Eric W Su, Birong Liao (in revising progress)
- **Imaging Markers Quantify Entire Tumour Microvasculature Normalization in Response to Sutent Treatment**, Chung-Wein Lee, Jian Wang, Kuldeep Neote, Michael Westmore (in revising progress)
- **Gene Expression Profiling in Germ Cell Tumors**, Chongxian Pan, Jackie Brames, Lacey Dobrolecki, Chung-Wein Lee, Robert Hickey, Lawrence Einhorn, *ASCO, 2003, 2004*
- **Effect of High-Impact Mechanical Loading On Synovial Cell Cultures**, Irene Sun, Yunlong Liu, Shigeo M. Tanaka, Chung-Wein Lee, Hui-Bin Sun, Hiroki Yokota; *Journal of Sports Science And Medicine*, March 2004

- **High Frequency Mechanical Stimuli to Osteoblasts In 3D Matrix**, Shigeo M. Tanaka, Hui Bin Sun, Chung-Wein Lee, David B. Burr, Charles H. Turner, and Hiroki Yokota (2003) Effect of Low Amplitude, ASME
- **Direct Imaging in the L_α State of 1,2-dipalmitoylphosphatidylcholine Bilayers**, C-W Lee, R.S. Decca, S.W. Wassall, J.J. Breen; *Physical Review E* 67 01914).
- **Single Molecular Tracking Scheme Using a Near-Field Scanning Optical Microscope**, Decca, RS, Lee CW, et al; *REV SCI INSTRUM* 73 (7):2675-2679 JUL 2002
- **Observation of Nanoscale Optical Activity and Diffusion on Lipid Membranes**, Lee, C.W., Lall S., Decca R.S., Wassall, S.R.; *Biophysical J.* 82:2672 (2002)
- **Molecular organization of cholesterol in polyunsaturated phospholipid membranes: a solid state NMR investigation**, Lee, C.W., Brzustowicz, M.R., Stillwell William, Wassall S.R.; *Biophysical J.* 80:2325.
- **Change in Osmotic Pressure due to Actin Polymerization and its Implications on Cellular Motility**, Lee, C.W., and Tang, J.X; *Biophysical J.* 78:1410 (2000)
- **Multifractal Measures of Earthquakes in West Taiwan**, Wang JH, Lee CW; *PURE APPL GEOPHYS* 146 (1): 131-145 FEB 1996
- **Fractal Characterization of an Earthquake Sequence**, Wang JH, Lee CW; *PHYSICA A* 221(1-3): 152-158 NOV 15 1995
- **Multifractal Measures of Time Series of Earthquakes**, Wang JH, Lee CW; *J PHYS EARTH* 45 (5): 331-345 1997
- **Characterization of Self-Organized Criticality by Mean-Field Theory and BTW Model**, Lee CW; *Master Thesis of Mathematical Physics*